UNIVERSITY OF OKLAHOMA

GRADUATE COLLEGE

METHANE POLLUTION IN THE SOUTHERN GREAT PLAINS: SOURCE QUANTIFICATION AND EXAMINATION OF IMPACTS OF LAND-ATMOSPHERE PROCESSES USING ROUTINE OBSERVATIONS, FIELD CAMPAIGN DATA, AND SIMULATIONS

A DISSERTATION

SUBMITTED TO THE GRADUATE FACULTY

in partial fulfillment of the requirements for the Degree of

DOCTOR OF PHILOSOPHY

By QINGYU WANG

Norman, Oklahoma

2024

METHANE POLLUTION IN THE SOUTHERN GREAT PLAINS: SOURCE QUANTIFICATION AND EXAMINATION OF IMPACTS OF LAND-ATMOSPHERE PROCESSES USING ROUTINE OBSERVATIONS, FIELD CAMPAIGN DATA, AND SIMULATIONS

A DISSERTATION APPROVED FOR THE

SCHOOL OF METEOROLOGY

BY THE COMMITTEE CONSISTING OF

Dr. Petra Klein, Chair

Dr. Xiao-Ming Hu

Dr. Sean Crowell

Dr. Ming Xue

Dr. Feng Xu

Dr. Xiangming Xiao

Acknowledgements

I would like to express my deepest gratitude to my advisors, Dr. Petra Klein, Dr. Xiao-Ming Hu, and Dr. Sean Crowell, for their support throughout this journey. Whether it was academic guidance or advice on life's challenges, you were always there when I needed a hand. I am also deeply grateful to my committee members, Dr. Feng Xu, Dr. Ming Xue, and Dr. Xiangming Xiao, for their invaluable insights and guidance throughout this journey. Whenever I faced confusion or uncertainty, their perspectives helped me navigate through complex challenges.

I am incredibly fortunate to have worked alongside such an inspiring group of lab mates in the GeoCarb team – Shuang Ma, Russell Doughty, Hélène Peiro, Jeff Niv, Steven Jester, Elizabeth Spicer, and Wesley Honeycutt. Your insights, collaboration, and friendship made the hard work more enjoyable.

To my family, your love and support have been my strength. Thank you to my mom, Hongjuan Ji, and my dad, Jianfei Wang, for always believing in me, and to my in-laws, Xiaomei Xuan and Lixin Zhao, for your kindness and support.

I would also like to extend my heartfelt thanks to the University of Oklahoma (OU), where I had the opportunity to learn and grow. Special thanks to my friends I met at OU – Holly Chik, Qiuye He, Jinmiao Chen, Zhimin Jiang, Lingling Ji, Sijie Pan, and Juan Zhao. Your friendship has been invaluable, and I cherish the memories we've shared. Additionally, my deepest thanks to my high school friends, Yuwei Shi and Yuan Yuan, for their enduring friendship and support over the years.

I must also acknowledge my beloved cats, Zhuangzhuang (Tammy) and Coupon, who have been my faithful companion through countless late nights of research and writing. Their presence has brought me comfort and joy during the most stressful times.

This journey has been filled with countless milestones, and I owe much of my strength to my husband, Yue Zhao. Despite an eight-year long-distance relationship, his love has been a constant in my life. Now that we are finally together, I look forward to the many adventures that lie ahead of us. Thank you, Yue, for being my partner in every sense of the word, and for making this journey possible.

I would also like to acknowledge the Southern Great Plains site team for their essential contributions to providing high-quality data. My work was also made possible thanks to the financial support from OCO-2 (NASA Grant Number 80NSSC18K0896), GeoCarb, and the DOE methane projects DE-FE00322292 and DE-FE0032285.

Finally, to everyone who has been a part of this journey – thank you from the bottom of my heart. I could not have done it without you.

Table of Contents

List of Tables

List of Figures

Abstract

Methane (CH_4) is a potent greenhouse gas, and accurately characterizing its emissions and distribution in the atmosphere is critical for advancing our understanding of its role in climate change. This dissertation consists of two key components of CH_4 dynamics: land-atmosphere interactions and emission quantification. By combining advanced modeling techniques with field observations, this work seeks to identify CH_4 emission sources and enhance our understanding of how land-atmosphere processes influence CH_4 concentrations. This is particularly important for improving inverse modeling approaches, where accurately linking CH_4 concentrations to emission sources relies on understanding how planetary boundary layer (PBL) dynamics and land surface processes affect CH_4 distribution in the atmosphere. These insights are crucial for refining CH_4 emission inventories and enhancing the effectiveness of mitigation strategies aimed at reducing CH_4 emissions.

The first focus of the dissertation is to examine land-atmosphere interactions specific to the Southern Great Plains (SGP) site in Oklahoma, as these dynamics play a crucial role in the transport and mixing of CH_4 within the PBL. We optimized seven key parameters of the Noah-Multiparameterization Land Surface Model (Noah-MP) to improve its representation of land-atmosphere interactions. Using Bayesian optimization (BO), we fine-tuned the model parameters using data from flux tower observations. This optimization not only enhanced the simulation of surface energy fluxes and meteorological state variables like temperature, but also provided insights into soil characteristics, suggesting that the top layer of soil at the SGP site may contain more sand than indicated by existing classifications. These improvements extended beyond the initial nine-day optimization period to the entire growing season in 2016, enhancing the accuracy of atmospheric state variables and top-layer soil conditions.

Building on the improved simulation of land-atmosphere processes, the second part of the research investigates CH_4 concentration enhancements at the SGP site from 2017 to 2020. Analysis of local meteorological data revealed that stable boundary layer conditions—characterized by strong temperature inversions and shallow PBLs—trap CH_4 near the surface, particularly during nighttime, leading to significant concentration spikes. Wind direction analysis identified a concentrated animal feeding operation (AFO) located 5.8 km northwest of the SGP site as a potential source of these CH_4 emissions. In a field campaign conducted in June 2024, we measured CH_4 concentrations exceeding 6000 ppb downwind of the AFO, corresponding to an emission rate of approximately 95 $kg \cdot hr^{-1}$, as calculated using the mass balance method. Additional nearby sources, including open-range cattle and a natural gas pipeline, were also identified as potential contributors to elevated CH_4 levels.

The final component of this dissertation integrates the field campaign data with high-resolution atmospheric modeling using the Weather Research and Forecasting model with Greenhouse Gas (WRF-GHG) model to assess whether the AFO could be responsible for the observed CH_4 enhancements at the SGP site. Using the WRF-GHG model, we simulated CH_4 dispersion from the AFO and validated these simulations against field data. The model successfully captured the spatial dispersion of CH_4 from the AFO and aligned well with field measurements, particularly around the AFO itself. However, the simulated CH_4 enhancement at the SGP site was lower than observed, even when assuming an AFO emission rate of 100 $kg \cdot hr^{-1}$. This discrepancy suggests that the actual emission rate from the AFO may be higher than previously estimated, underscoring the need for more accurate emission inventories. The field campaign also revealed that rainfall events significantly increase CH_4 emissions, particularly from manure ponds and open lots, where microbial activity is enhanced in wet conditions. These findings highlight the importance of improving CH_4 emission inventories and refining atmospheric models, particularly in agricultural regions where localized sources can have substantial impacts on regional CH_4 concentrations.

This dissertation bridges gaps in our understanding of CH_4 emissions by optimizing land-surface models, quantifying local CH_4 sources, and validating atmospheric simulations. By integrating empirical field data with advanced modeling approaches, this research enhances our understanding of CH_4 dynamics at local and regional scales, with important implications for global CH_4 inventories and climate policies aimed at mitigating CH_4 emissions.

Chapter 1 Introduction

1.1 Background and Objectives

The Planetary Boundary Layer (PBL) serve as a critical interface between the atmosphere and the Earth's surface, and it is also the layer where atmospheric processes directly interact with human activities. PBL processes are essential for regulating our climate, weather, and air quality by enabling the exchange of energy, moisture, and trace gases between the Earth's surface and the atmosphere (Betts 2009; Dickinson 1995; He et al. 2021; Santanello Jr et al. 2011a; Santanello Jr et al. 2011b). A better understanding of these dynamics and interactions is crucial for effectively predicting climate variability, extreme weather events, and their impacts on ecosystems and human societies. Broadly speaking, we can make distinctions between the type of interactions associated with the following two areas:

1. Physical Climate System

The physical interactions between the atmosphere and the Earth's surface, involving the exchanges of radiation, sensible heat, latent heat, and momentum, are fundamental to shaping our climate. These interactions affect various scales from daily weather events to long-term climate patterns, influencing atmospheric conditions such as atmospheric temperature, humidity, wind, and precipitation, as well as ground surface states like soil temperature and moisture (Andrews 2009; Bateni and Entekhabi 2012; Beringer and Tapper 2002; Boer 1993; Dickinson 1983; Siler et al. 2019). The study of these processes provides crucial insights into how energy and mass transfers within the PBL can trigger or mitigate various weather phenomena, including extreme events like thunderstorms and droughts.

2. Biogeochemical Cycles

Trace gases such as carbon dioxide (CO_2), methane (CH_4), and various nitrogenous compounds play a pivotal role not only in radiative transfer and broader climate system (Collins et al. 2006; Iacono et al. 2008; Myhre et al. 1998) but also in public health (Anenberg et al. 2012; Haines et al. 2009; West et al. 2006). CH_4 needs particular attention due to its higher radiative efficiency compared to CO_2 – The radiative forcing from CH_4 is approximately 26 times that of CO_2, on a per-ppb basis (Stocker et al. 2013). By intensifying efforts to understand and manage CH_4 emissions, we can implement more immediate and effective measures to mitigate global warming. This makes understanding and controlling CH_4 emissions a strategic and effective approach to slowing global warming (Fiore et al. 2002; Heilig 1994; Hogan and Hoffman 1991; Milich 1999; Yavitt 1992).

In my dissertation, I explore the intricate dynamics of surface energy balance, land-atmosphere interactions (LA-I), the PBL, and Greenhouse Gases (GHGs), utilizing the comprehensive observational capacities of the Atmospheric Radiation Measurement (ARM) Program's Southern Great Plains (SGP) site (Sisterson et al. 2016). The diverse atmospheric datasets collected at the SGP site are invaluable for understanding the complex interactions between the surface and the atmosphere, thereby providing critical insights into both regional and global climate dynamics. Through this research, I aim to contribute to a better understanding of these interactions, supporting broader efforts to improve climate predictions and strategies for mitigating climate change impacts.

Specifically, this dissertation aims to advance the understanding of how land surface characteristics and PBL dynamics interact with CH_4 emissions at the SGP site. The objectives of this research are to:

1. Improve the understanding of surface energy exchange, the state (temperature and moisture) of the surface and the lower atmosphere and how they impact the PBL development and evolution.
2. Explore the mechanisms influencing near-surface CH_4 concentrations, particularly through the dynamics of the PBL at the SGP site.
3. Utilize observational data and model simulations to identify CH_4 emission sources and quantify their emission rates effectively.

1.2 Proposed Research and Overall Approach

To address Objective 1, this study employs Bayesian Optimization (Frazier 2018) to refine key parameters within the Noah-Multiparameterization Land Surface Model (Noah-MP) (Niu et al. 2011; Yang et al. 2011), which is implemented in a single-column configuration of the Weather Research & Forecasting (WRF) Model (Skamarock et al. 2008). The goal is to identify physically realistic parameter values that better align with observations from eddy covariance towers and surface meteorological stations at the SGP site during the 2016 alfalfa growing season. By updating these parameters, the model aims to improve the simulation of surface energy fluxes, near-surface atmospheric conditions, soil characteristics, and PBL development. Additionally, when integrated with soil texture records, these updated parameters are expected to suggest a more accurate representation of soil texture.

Building on the improved understanding of land-atmosphere interactions and PBL dynamics at the SGP site, this research also seeks to explain the observed high near-surface CH_4 concentrations at SGP (Objective 2). This is achieved by analyzing data from balloon-borne radiosondes, Doppler lidar wind profiles, surface meteorological stations, and WRF simulations, which collectively help to elucidate the influence of PBL dynamics on CH_4 levels recorded by the PGS system at the SGP over the past decade.

However, PBL dynamics alone may not fully account for the elevated CH_4 levels at the SGP. To address this, a field campaign was conducted in June 2024 to investigate potential CH_4 sources that might be absent from current inventories, using a LI-COR LI-7810 $CH_4/CO_2/H_2O$ Trace Gas Analyzer (https://www.licor.com/env/products/trace-gas/LI-7810, LI-COR Biosciences, Lincoln, Nebraska, USA). The LI-7810 was mounted on a pickup truck, with the inlet pipe positioned at the driver's window, and driven at speeds under 5 miles per hour. Measurements were conducted upwind and downwind of potential CH_4 sources such as animal feeding facilities (AFO), oil wells, natural gas pipelines, and free-range cattle. Addressing Objective 3, emission rates were quantified using methods like mass balance (Karion et al. 2015; Lavoie et al. 2015; Pandey et al. 2019; Peischl et al. 2015), combined with wind data from the SGP site's meteorological station.

Building on our studies of PBL dynamics and CH_4 emissions at the SGP site, we aim to extend these methods to local and community scales, such as the city of Norman in Oklahoma. This approach lays the groundwork for accurately identifying and quantifying CH_4 emissions in various settings, contributing to the development of precise CH_4 inventories. Moreover, it provides a robust reference point for refining other GHG inventories, enhancing their accuracy and reliability for both scientific research and policymaking.

Chapter 2 Literature Review

2.1 Background of Land-Atmosphere Interactions (LA-I) and their connection to the Planetary Boundary Layer (PBL)

Land-Atmosphere Interactions (LA-I) are fundamental to understanding the exchange of energy, moisture, and greenhouse gases between the Earth's surface and the atmosphere. These interactions are key drivers of many fundamental atmospheric processes, such as the formation of weather patterns, the distribution of precipitation, and the regulation of surface temperatures (Betts et al. 1996; Bonan 2008; Brubaker and Entekhabi 1996; Dickinson 1995; Kollet and Maxwell 2008; Santanello Jr et al. 2011a; Seneviratne et al. 2010). The dynamic exchange between the land and the atmosphere also has significant implications for climate variability and change on both regional and global scales(Barros and Hwu 2002; Betts et al. 1996; Betts 2007; Chelton and Xie 2010; Findell et al. 2011; Raupach 1995; Santanello Jr et al. 2011a; Seneviratne et al. 2006). Therefore, understanding LA-I is vital for improving weather forecasts and climate models.

LA-I is primarily confined between the land surface and the Planetary Boundary Layer (PBL), the lowest part of the atmosphere (Helbig et al. 2021; Yi et al. 2004) which typically extends from a few meters up to 1-3 kilometers in height. These interactions are largely driven by turbulent transport and mixing processes near the Earth's surface (Stull 2015). Key processes include the transfer of sensible and latent heat, momentum, and moisture, which vary significantly over diurnal cycles due to solar radiation (Su 2006). To quantify these transfer processes, the surface energy balance (SEB) is examined, which includes net radiation (Rn), sensible heat flux (H, the conductive heat flux from the Earth's surface to the atmosphere), latent heat flux (LE, the heat flux from the Earth's surface to the atmosphere that is associated with evaporation or condensation of water vapor at the surface), and ground heat flux (G, the heat flux from the soil to the earth's surface). The SEB describes the balance of Rn, G, H, and LE in the soil-surface-atmosphere system when energy stored (or lost) at the land surface can be neglected as in Equation 2.1:

$$Rn = G + H + LE, \quad (2.1)$$

In general, during the day, incoming solar radiation is primarily balanced by outgoing sensible and latent heat fluxes, while at night, the loss of energy through longwave radiation is offset by reduced or reversed heat fluxes from the ground and atmosphere. Through these fluxes, particularly H and LE, the energy absorbed by the land surface can be transferred upward into the PBL.

The SEB is tightly related to the diurnal evolution of the PBL (Mahmood et al. 2011), with strong daytime upward fluxes of sensible and latent heat resulting in deep convective mixed layers, while at night, reduced turbulence and radiative cooling typically lead to a more stable and shallow PBL. The growth of the daytime PBL (daytime in Figure 2.1) is primarily driven by thermal eddies (Helbig et al. 2021). In terms of energy fluxes, the daytime PBL development depends on available energy ($H + LE$) at the land surface and the energy partitioning between H and LE (the Bowen ratio $\beta = \frac{H}{LE}$), as in Figure 2.2. When β is high, indicating that more energy is converted to H, the PBL tends to grow more rapidly. In contrast, a lower β, where LE dominates, results in a more restrained PBL growth. For instance, in arid environments, where the energy balance favors sensible heat flux, the PBL expands quickly, whereas in regions with heavy vegetation, much of the energy is consumed as latent heat through processes like evaporation and transpiration, which slows PBL development. Additionally, the rate at which the PBL evolves is modulated by several factors, including the presence and strength of a capping inversion, entrainment processes from the free atmosphere above (Driedonks and Tennekes 1984; Wyngaard and Brost 1984), and the effects of vertical gradients in temperature and moisture, as well as wind shear (Batchvarova and Gryning 1991).

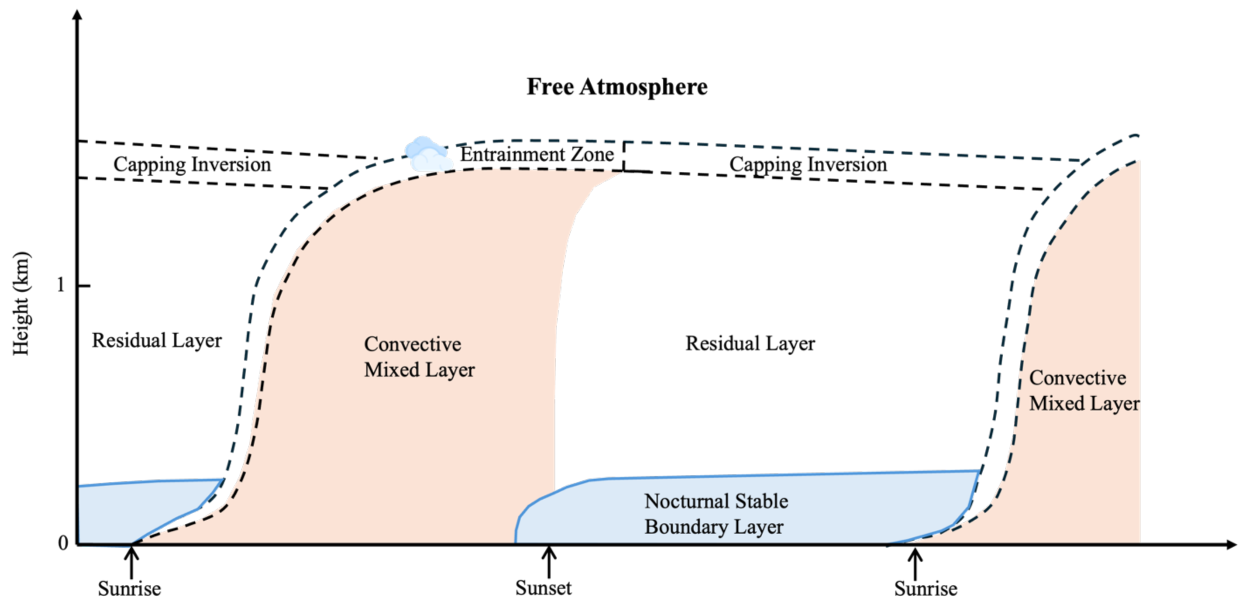

Figure 2.1 Ideal diurnal development of the planetary boundary layer (PBL) during the day, from sunrise to sunset, and transformation to the nocturnal stable boundary layer from sunset to sunrise (figure after Stull (1988)).

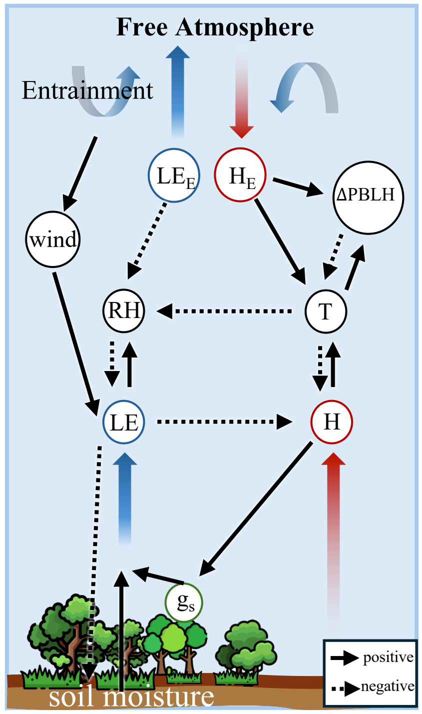

Figure 2.2 Key daytime interactions and feedback between surface sensible (H) and latent heat (LE) fluxes, entrainment fluxes (H_E, LE_E), atmospheric boundary layer growth rate (ΔPBLH), land surface (e.g., soil moisture) and vegetation conditions (e.g., stomatal conductance (g_s)), and relative humidity (RH), and mixed-layer temperature (T)). Horizontal advection is not shown. Figure is summarized and simplified from Santanello Jr et al. (2011b) and Helbig et al. (2021).

At sunset, as solar heating ceases, buoyancy-driven turbulent mixing quickly weakens, and a stable nocturnal boundary layer (NBL) begins to form near the surface, below an elevated a residual layer (Fig 2.1). Under strong atmospheric stability conditions, the residual layer can become decoupled from the shallow NBL due to the significant suppression of vertical mixing. The results from the CASES-99 project which was mainly conducted in southeastern Kansas suggest the NBL can be very stable under weak winds, clear sky, and strong surface radiative cooling conditions (Banta et al. 2007). Under these very stable NBL conditions, the strong stability of the radiational temperature inversion is effective in suppressing both turbulence and turbulent mixing, thereby producing a vertically thin, highly structured NBL – sometimes lower than 10m.

2.2 Methane (CH_4) Dynamics within Land-Atmosphere Interactions

Methane (CH_4) plays a pivotal role in global warming and is the second most significant greenhouse gas contributor to climate change in terms of radiative forcing, following carbon dioxide (Myhre et al. 2014; Stocker et al. 2013). Despite its critical importance, the complexity of CH_4 emissions and their atmospheric concentrations – particularly their interaction with meteorological variables, remains less understood. This lack of detailed understanding impedes the accuracy of predictive atmospheric models and challenges the effectiveness of strategies aimed at mitigating climate change impacts. Addressing this knowledge gap is crucial, necessitating in-depth studies to explore the meteorological interactions that influence CH_4 variability within the Earth's atmosphere.

The emission source of CH_4 can be both anthropogenic and natural. CH_4 is emitted during the production and transport of coal, natural gas, and oil (Chandra et al. 2021; Kirchgessner et al. 1993; Krings et al. 2013). CH_4 emissions also result from livestock (Dangal et al. 2017; Gerber et al. 2013; Omara et al. 2018) and other agricultural practices like rice cultivation (Cai et al. 2007; Wassmann et al. 2000; Zhang et al. 2016), land use (Ishizuka et al. 2002; McDaniel et al. 2019; Verchot et al. 2000), and by the decay of organic waste in municipal solid waste landfills (Boeckx et al. 1996; Bogner and Spokas 1993; Wang et al. 2017).

The major amount of CH_4 is removed by the photolytically produced hydroxyl radical (OH) in the troposphere (Rigby et al. 2017). However, the CH_4 removal from the chemical reaction with OH is small on a diurnal scale (Patra et al. 2009), unlike CO_2, whose diurnal cycle heavily relies on diurnal changes in photosynthetic uptake and PBLH variations (Hu et al. 2020; Law et al. 2008; Metya et al. 2021), the diurnal cycle of CH_4 near the surface may primarily relies on regional/local transport, PBL turbulent mixing, and emission rate (GaŽovic et al. 2010; Metya et al. 2021; Nishanth et al. 2014).

Since the primary sources of CH_4 emissions—such as wetlands, agricultural activities, and fossil fuel extraction—originate from the land surface, the way CH_4 is emitted and dispersed in the atmosphere is influenced by the same interactions that govern the exchange of energy, moisture, and momentum between the surface and the ABL. Thus, comprehending these processes is crucial for accurately quantifying and managing CH_4 emissions and concentrations.

To understand the role of CH_4 in climate change, it is crucial to accurately determine both the amount and distribution of CH_4 emissions, as well as how these emissions interact within the atmosphere. This includes understanding the processes that control the atmospheric lifetime of CH_4, such as its oxidation by OH (McNorton et al. 2016; Rigby et al. 2017). We also need to consider the impact of CH_4 on radiative forcing (Etminan et al. 2016; Forster et al. 2007; Myhre et al. 2011; Robertson et al. 2000), given its potency as a greenhouse gas, and how it contributes to feedback mechanisms that influence global temperatures, cloud formation, and precipitation patterns (Boucher et al. 2009; Kasting 2004; Reay et al. 2018). Understanding these processes also involves examining how CH_4 interacts with other atmospheric constituents, like ozone, and how these interactions affect air quality and climate (Dentener et al. 2005; Fiore et al. 2002).

However, as the first step in this complex cycle, CH_4 emissions themselves remain poorly constrained and difficult to quantify accurately. Natural sources, such as wetlands, are influenced by variable factors like temperature, moisture, and microbial activity (Bridgham et al. 2013; Christensen et al. 2003; Singh et al. 2000; Zhang et al. 2017), while anthropogenic sources, such as agriculture and fossil fuel extraction, are challenging to monitor due to the diffuse nature of emissions, inconsistent reporting standards, and uncertainty in assumed emission factors

(Balcombe et al. 2017; Caulton et al. 2014; Gao et al. 2022). This uncertainty is compounded by the spatial and temporal variability of emissions and the limited availability of high-resolution observational data. Consequently, there is a critical need for improved measurement techniques, enhanced modeling approaches, and more comprehensive data integration to better quantify CH_4 emissions and understand their role in climate dynamics.

CH_4 emission sources are derived from two main approaches: the "bottom-up" approach, which utilizes inventories and process models to estimate emissions, and the "top-down" approach, which relies on atmospheric observations integrated into chemical transport models to infer fluxes. The bottom-up approach faces challenges such as uncertainties in the underlying activity data, emission factors, and the extrapolation of limited observational data to broader regions, which can introduce significant biases. Moreover, this approach lacks constraints on the total global emissions of CH_4. On the other hand, the top-down approach is hindered by gaps and inaccuracies in observational data, as well as by our limited understanding of atmospheric transport processes and the chemical removal of CH_4. Together, these limitations contribute to a substantial discrepancy between the two methods of estimating CH_4 emissions.

CH_4 emissions are typically estimated in two approaches: 1. “bottom-up,” in which inventories or process models are used to predict fluxes, or 2. “top-down,” in which fluxes are inferred at a regional scale like an oil wells (Vaughn et al. 2018). Bottom-up methods suffer from uncertainties and potential biases in the available activity data or emissions factors or the extrapolation to large scales of a relatively small number of observations (Balcombe et al. 2017). Top-down methods are constrained at smaller scale compared to bottom-up method inferred fluxes, and are limited by incomplete or imperfect observations and our understanding of atmospheric transport and chemical sinks. For CH_4, these difficulties result in a significant mismatch between the two methods – the flux inferred from top-down methods is usually 1.5 times larger than bottom-up inferred ones (Vaughn et al. 2018).

2.3 Current observations and methods

2.3.1 Energy flux measurements

Flux measurements are widely used to estimate heat, water, and CO_2 exchange, as well as CH_4 and other trace gases. Eddy Covariance systems, which were first introduced in the 1940s (Montgomery 1948; Obukhov 1951; Swinbank 1951) is one of the most direct and defensible ways to measure such fluxes (Verma 1990).

In very simple terms, when we have turbulent flow, the vertical flux (F) is equal to a mean product of air density (ρ_a), vertical wind speed (w) and the mixing ratio of the gas of interest (s):

$$F = \overline{\rho_a w s}, \text{(2.2)}$$

We can use Reynold decomposition to express each variable on the right-hand side of Eqn (2) as the sum of its mean and fluctuating components, for instance, $\rho_a = \overline{\rho_a} + \rho_a{}'$. By making two key assumptions – (i) air density fluctuations are negligible; and (ii) mean vertical flow is negligible for horizontally homogeneous terrain – Equation 2.2 can be simplified to:

$$F = \overline{\rho_a w s} = \overline{(\overline{\rho_a} + \rho_a{}')(\overline{w} + w')(\overline{s} + s')} \approx \overline{\rho_a}\, \overline{w' s'}, \text{(2.3)}$$

The above is the general equation to estimate fluxes: the turbulent flux is approximately equal to mean air density multiplied by the mean covariance between deviations in instantaneous vertical wind speed w and mixing ratio s.

By analogy, sensible heat flux is equal to the mean air density multiplied by the covariance between deviations in instantaneous vertical wind speed and temperature; conversion to energy units is accomplished by including the specific heat C_p. Latent heat flux is computed in a similar manner using water vapor. CH_4 flux is presented as the mean covariance between deviations in instantaneous vertical wind speed and density of CH_4 in the air.

CH_4 flux: $F_{ch_4} = \overline{w'\rho_{ch_4}{}'}$, (2.4)

Sensible heat flux: $H = \rho_a C_p \overline{w'T'}$, (2.5)

Latent heat flux: $LE = \rho_a L_e \overline{w'q'}$, (2.6)

where C_p is the heat capacity of air (J kg^{-1} K^{-1}), L_e is the latent heat of vaporization of water (J kg^{-1}), and w', T', q′, $\rho_{ch_4}{}'$ are the fluctuation values of the vertical wind speed (m s^{-1}), sonic temperature (°C), specific humidity (g kg^{-1}), and the dry CH_4 mixing ratio (ppb or nmol mol^{-1}), respectively.

There are other methods like the Bowen ratio-energy balance (BREB) methods used to estimate fluxes. The BREB method estimates LE from a surface using measurements of air temperature and humidity gradients, net radiation, and soil heat flux (Fritschen and Simpson 1989). It is an indirect method, compared to methods such as eddy covariance, which directly measures turbulent fluxes, or weighing lysimeters, which measure the mass change of an isolated soil volume and the plants growing in it. The principles, pros, and cons comparison are listed in the following Table 2.1.

Since the eddy covariance method is a direct measurement, the eddy covariance method is the most used micrometeorological method to obtain accurate measurements of turbulent energy fluxes. This method is particularly valuable for understanding carbon, water, and energy exchanges between ecosystems and the atmosphere, providing essential data for assessing ecosystem function, carbon budgets, and climate change impacts.

Table 2.1 The principles, pros, and cons of surface-energy balance measurement methods.

Method	Principle	Strengths	Limitations	References
Lysimeters	Estimate evapotranspiration by measuring changes in soil water weight over time	Provides a direct measurement of evapotranspiration; highly accurate for site-specific studies; good for validating other methods.	Expensive and non-portable	Gebler et al. (2015); Goss and Ehlers (2009); López-Urrea et al. (2006)
Bowen Ratio –Energy Balance method	Latent heat flux based on the temperature and humidity gradient between two levels	Relatively simple setup; suitable for homogeneous and flat terrain; less costly than some other methods.	Requires extensive fetch; sensitive to instrument biases in temperature and humidity measurements	Prueger et al. (1997); Spittlehouse and Black (1980); Todd et al. (2000)
Scintillometer	Measuring the intensity fluctuations of electromagnetic radiation as it passes through the atmosphere	Can measure fluxes over larger areas than point-based methods; useful in heterogeneous landscapes.	High-cost method; disrupted by optical interception from rain, insects, frost, and air temperature variations	Chehbouni et al. (2000); Hemakumara et al. (2003); Meijninger et al. (2002)
Eddy Covariance (EC) system	Direct measurement of turbulent fluxes of heat, moisture, and trace gases using high-frequency sensors	Direct, high-frequency measurements of fluxes; highly accurate and widely applicable across different ecosystems; suitable for long-term monitoring.	Very expensive; measurements can be compromised by low wind speeds, mounting, or sensor head distortions	(Baldocchi et al. 2001; Delwiche et al. 2021); Fisher et al. (2008); Mauder et al. (2013)
Surface Renewal Method	Estimates fluxes by analyzing high-frequency temperature fluctuations near the surface	Lower cost compared to eddy covariance; useful in situations where eddy covariance is impractical; provides continuous measurements.	Less commonly used; accuracy depends on proper calibration; sensitive to environmental noise and surface conditions	Morán et al. (2020); Qiu et al. (1995); Snyder et al. (1996); Spano et al. (2000)

Building on the advantages of eddy covariance method, global networks such as FLUXNET (Baldocchi et al. 2001) and AmeriFlux (Novick et al. 2018) have been established to coordinate and standardize eddy covariance measurements across diverse ecosystems worldwide. FLUXNET is a global network that integrates data from over 1,000 flux towers across various biomes and climates, providing comprehensive datasets that support a wide range of scientific research, from local ecosystem studies to global climate modeling efforts. These flux towers continuously monitor exchanges of CO_2, CH_4 water vapor, and energy, contributing valuable insights into the carbon cycle, ecosystem productivity, and how different ecosystems respond to environmental changes.

AmeriFlux is a regional subset of FLUXNET, which focuses on ecosystems in the Americas, including North, Central, and South America. It provides critical data for studying LA-I in a wide range of environments, from tropical rainforests to arid deserts. AmeriFlux sites adhere to rigorous measurement standards, ensuring data quality and comparability across sites and over time. This consistency allows researchers to examine spatial and temporal trends in carbon, water, and energy fluxes, improving our understanding of ecosystem processes and their response to climatic variability and human activities.

2.3.2 CH_4 emission estimations

Direct CH_4 flux measurements provide high-precision data for quantifying methane emissions from specific sources and validating CH_4 emission inverse modeling. These methods are critical for understanding methane dynamics at the local scale and serve as a foundation for validating larger-scale emissions models. Key methods are in Table 2.2:

Table 2.2 Approaches to measure CH_4 fluxes directly

Method	Description	Strengths	Limitations	References
Chamber	This method involves placing a chamber over a small area of the ground (or water surface in the case of wetlands) to capture the emitted methane. Gas samples are collected from the chamber over time, and the methane flux is calculated based on the rate of change in methane concentration within the chamber.	Simple to implement, highly accurate for small-scale emissions.	Only measures small, localized areas, and may not capture variability at larger scales.	Chan and Parkin (2001); Keller and Stallard (1994); Ueyama et al. (2015)
Eddy Covariance Method	A flux measurement technique that directly measures the vertical turbulent transport of gases using high-frequency wind and concentration data.	High accuracy and real-time flux data over small areas.	Limited to flat terrains, small footprints, and turbulence.	McDermitt et al. (2011); McNicol et al. (2023); Morin (2019)
Relaxed Eddy Accumulation Method	Based on conditional sampling, where the vertical wind direction (updrafts and downdrafts) is used to determine when to sample air. Unlike Eddy Covariance, Relaxed Eddy Accumulation Method does not continuously measure gas concentrations; instead, it samples air during specific periods of vertical wind motion and accumulates these samples for analysis.	Requires lower-frequency sampling compared to EC	The accuracy of Relaxed Eddy Accumulation Method depends on the empirical determination of the "b" factor; Coarse in time resolution – about 30 minutes	Sakabe et al. (2012); Ueyama et al. (2013)

2.4 Modeling

The Weather Research and Forecasting (WRF, Skamarock et al. (2019)) model incorporates a comprehensive suite of parameterizations that simulate the atmospheric, land surface, and chemical processes critical for accurate weather prediction and climate analysis . These parameterizations, which include the PBL, land surface, and chemistry modules, are integral to the model's ability to capture complex interactions within the Earth system.

The PBL parameterization is essential for accurately depicting vertical mixing and turbulence, which are influenced by thermal and moisture gradients between the land surface and the atmosphere (Hu et al. 2010; Tyagi et al. 2018). The land surface models within WRF handle the biophysical and hydrological interactions at the surface, such as soil moisture, vegetation cover, and energy exchanges (Jin et al. 2010; Lee et al. 2016). These exchanges are critical for realistic simulations of surface temperature, evaporation, and sensible heat flux.

Parameterizations of atmospheric chemistry, which address the transformation and movement of greenhouse gases like CH_4, are closely linked to processes in the PBL and at the land surface. For instance, the breakdown of CH_4 in the atmosphere is highly dependent on temperature and humidity conditions shaped by surface and PBL dynamics. Conversely, elevated CH_4 concentrations can influence local radiative balance, thereby affecting surface temperatures and the development of the PBL.

The effectiveness of WRF in simulating weather and environmental conditions hinges on the seamless integration of these parameterizations. By accurately capturing the dynamics of the PBL, the physical processes at the land surface, and the chemical composition of the atmosphere, WRF provides a robust framework for understanding and predicting atmospheric phenomena.

2.4.1 Land Surface Model – Noah-MP

The Noah-Multiparameterization (Noah-MP) Land Surface Model represents an advanced evolution of the Noah model, enhancing its capabilities through multiple parameterization options that extend its applicability across different climatic and environmental conditions (Niu et al. 2011; Yang et al. 2011). Designed to interface seamlessly with atmospheric models like the WRF system, Noah-MP incorporates a diverse range of physical processes including vegetation, soil moisture, and hydrological dynamics. This modular extension enables more detailed simulations of land-atmosphere exchanges, crucial for accurate weather forecasting and climate research (Ju et al. 2022; Li et al. 2022). By integrating more complex biophysical interactions and feedback mechanisms, such as dynamic vegetation, urban canopy models, and varied soil moisture transfer functions, Noah-MP offers a sophisticated tool for researchers aiming to better understand and predict the interactions between the land surface and the atmosphere.

The Noah-MP land surface model is distinguished by its flexibility in simulating a wide range of physical processes through customizable options that enhance model adaptability and precision. In Table 2.3, we detail the configurable physical process options available within the Noah-MP land surface model.

In Noah-MP, there are 71 standard parameters which are included in four tables: MPTable.tbl, VegParm.tbl, SoilParm.tbl, GenParm.tbl, which are tables in Noah-MP describing carbon storage, physiology, radiation, runoff, snow energy, snow water, soil energy, soil-physiology interactions, soil water, transfer factor, vegetation structure, and volatile organic carbon parameters.

Table 2.3 Noah-MP parameterization options and options chose in this study.

Physical Process	Available Options	Options Chosen
Vegetation (dveg)	1. Prescribed LAI and shade fraction 2. LAI and shade fraction calculated from dynamic simulation of carbon uptake and partitioning 3. Shade fraction calculated from prescribed LAI	1. Prescribed LAI and shade fraction
Stomatal resistance (opt_crs)	1. Ball-Berry (Ball et al. 1987) 2. Javis (Chen et al. 1996)	1. Ball-Berry
Soil moisture factor for stomatal resistance (opt_btr)	1. Noah type (Chen et al. 1996) 2. CLM type (Oleson et al. 2010) 3. SSiB type (Xue et al. 1991)	1. Noah type
Runoff and groundwater (opt_run)	1. TOPMODEL with groundwater (Niu et al. 2007) 2. TOPMODEL with equilibrium water table (Niu et al. 2005) 3. Original surface and subsurface runoff (free drainage) (Schaake et al. 1996) 4. BATS surface and subsurface runoff (free drainage) (Yang and Dickinson 1996)	1. original surface and subsurface runoff (free drainage)
Surface layer drag coefficient (opt_sfc)	1. Monin-Obukhov (Brutsaert 1982) 2. Original Noah (Niu and Yang 2006)	1. Monin-Obukhov
Supercooled Liquid Water option (opt_frz)	1. No iteration (Niu and Yang 2006) 2. Koren's iteration (Koren et al. 1999)	1. No iteration
Soil Permeability option (opt_inf)	1. Linear effects (Niu and Yang 2006) 2. Non-linear effects (Koren et al. 1999)	1. Linear effects
Radiative Transfer (opt_rad)	1. Modified two-stream (Niu and Yang 2004; Yang and Friedl 2003) 2. Two-stream applied to grid-cell 3. Two-stream applied to vegetated fraction	3. Two-stream applied to vegetated fraction
Ground Surface Albedo (opt_alb)	1. BATS (Yang et al. 1997) 2. CLASS (Verseghy 1991)	2. CLASS
Precipitation Partitioning between snow and rain (opt_snf)	1. Jordan (Jordan 1991) 2. BATS: Snow when T_air < T_frz + 2.2K, where T_frz is a constant 3. Snow when T_air < T_frz 4. Use WRF precipitation partitioning	1. Jordan

The numerous physical options provided by Noah-MP can lead to hundreds of possible combinations, each potentially activating or deactivating different sets of parameters. Based on the selected options shown in Table 2.3, the details of the active parameters and their corresponding physical explanations are summarized in Table 2.4.

Table 2.4 Noah-MP standard vegetation parameters with description, units, category, range, and involved physics.

Parameter	Description	Units	Category [a]	Range	Processes involved
Z0MVT	Momentum roughness length	m	VegS	0.06 – 1.10	VEGE_FLUX(vegetation fluxes)
HVT	Height of top of canopy	m	VegS	max([1.0,0.5*alpha]) – min([20.0 – 2.0*alpha]) alpha=2 for crops	VEGE_FLUX(vegetation fluxes)
					PHENOLOGY
HVB	Height of bottom of canopy	m	VegS	0.1*HVT – 0.9*HVT	RADIATION (when radiation option is 1: Modified two-stream)
					PHENOLOGY
RC	Tree crown radius	–	VegS	0.08 – 3.60	RADIATION (when radiation option is 1: Modified two-stream)
LAI	Leaf area index multiplier	m^2 m^{-2}	VegS	0 – 5	SURRAD(surface radiation)
					CANWATER(canopy hydrology)
					Emissivity
SAI	Stem area index multiplier	m^2 m^{-2}	VegS	0 – 5	Same with LAI
RSMAX	Maximal stomatal resistance	s m^{-1}	VegS	2000 – 5000	VEGE_FLUX(when stomatal resistance option is 2:Jarvis)

Table 2.5 Noah-MP standard radiation parameters with description, units, category, range, and involved physics.

Parameter	Description	Units	Category[a]	Range	Processes involved
RHOL-vis	Leaf reflectance in visible spectrum	–	Rad	0 – 0.11	RADIATION (two stream)
RHOL-nir	Leaf reflectance in NIR	–	Rad	0 – 0.58	Same with RHOL-vis
RHOS-vis	Stem reflectance in visible spectrum	–	Rad	0 – 0.36	Same with RHOL-vis
RHOS-nir	Stem reflectance in NIR	–	Rad	0 – 0.58	Same with RHOL-vis
TAUL-vis	Leaf transmittance in visible spectrum	–	Rad	0 – 0.07	Same with RHOL-vis
TAUL-nir	Leaf transmittance in NIR	–	Rad	0 – 0.25	Same with RHOL-vis
TAUS-vis	Stem transmittance in visible spectrum	–	Rad	0 – 0.22	Same with RHOL-vis
TAUS-nir	Stem transmittance in NIR	–	Rad	0 – 0.38	Same with RHOL-vis
RGL	Parameter used in radiation stress function	–	Rad	30 – 1000	VEGE_FLUX(when stomatal resistance option is 2:Jarvis)

Table 2.6 Noah-MP standard soil parameters with description, units, category, range, and involved physics.

Parameter	Description	Units	Category[a]	Range	Processes involved
BEXP	Pore size distribution index	–	SoilW	4.26 – 11.55	SOILWATER(when Runoff and Groundwater option is 2: TOPMODEL with equilibrium water table)
					SOILWATER(when Soil Permeability option 1: Linear effects)

					VEGE_FLUX(when Soil Moisture Factor for Stomatal Resistance option is 2:CLM and 3:SSiB)
					PHASECHANGE
					Soil water evaporation (when surface evaporation resistance option is 1: Sakaguchi and Zeng, 2009)
DKSAT	Saturated soil hydraulic conductivity	$m\ s^{-1}$	SoilW	1e-6 – 1.4e-5	SOILWATER(when Soil Permeability option 1: Linear effects)
DWSAT	Saturated soil hydraulic diffusivity	$m^2\ s^{-1}$	SoilW	5e-6 – 1.4e-5	SOILWATER(when Soil Permeability option 1: Linear effects)
PSISAT	Saturated soil matric potential	$m\ m^{-1}$	SoilW	0.036 – 0.468	VEGE_FLUX(when Soil Moisture Factor for Stomatal Resistance option is 2:CLM and 3:SSiB):
					SOILWATER(when Runoff and Groundwater option is 2: TOPMODEL with equilibrium water table)
					PHASECHANGE(melting/freezing of snow water and soil water)
SMCMAX	Porosity	$m^3\ m^{-3}$	SoilW	0.4 – 0.7	VEGE_FLUX(when Soil Moisture Factor for Stomatal Resistance option is 2:CLM and 3:SSiB):
					Soil water evaporation (all options)
					THERMOPROP(soil thermal property)
					PHASECHANGE

					SOILWATER(when Runoff and Groundwater option is 2: TOPMODEL with equilibrium water table)
SMCREF	Field capacity	m^3 m^{-3}	SoilW	1/3*SMCMAX – SMCMAX	VEGE_FLUX(when Soil Moisture Factor for Stomatal Resistance option is 1: Noah)
SMCWLT	Wilting point soil moisture	m^3 m^{-3}	SoilW	SMCDRY – SMCREF	VEGE_FLUX(when Soil Moisture Factor for Stomatal Resistance option is 1: Noah)
					SOILWATER(when Runoff and Groundwater option is 2: TOPMODEL with equilibrium water table)
					Soil water evaporation (when surface evaporation resistance option is 1
CSOIL	Volumetric soil heat capacity	J m^{-3} K^{-1}	SoilE	$2e^6$ – $3e^6$	THERMOPROP(soil thermal property)
QUARTZ	Soil quartz content	m^3 m^{-3}	SoilE	0.25 – 0.82	THERMOPROP(soil thermal property)

Abbreviations in the categories: C:Carbon; Input: Input; Phys: Physiology; Rad: Radiation; Run: Runoff; SnowE: Snow energy; SnowW: Snow water; SoilE:Soil energy; SoilP: Soil-Physiology interactions; SoilW: Soil water; Trans: Transfer; VegS: Vegetation structure; VOC: Volatile organic carbon.

The explanation column illustrates how changes in parameter values affect land surface processes in Noah-MP. The => arrow indicates a positive effect (i.e., A increase results B increase, or A decrease results B decrease), while –> arrow indicates a negative effect.

2.4.2 CH_4 Emission Inverse Modeling

Current efforts to measure CH_4 involve a combination of bottom-up and top-down methods (Delwiche et al. 2021; Frankenberg et al. 2005; Jacob et al. 2016; Karion et al. 2015; Parker et al. 2011; Röckmann et al. 2016; Shaw et al. 2021; Toon et al. 2009; Tsuboi et al. 2013), each providing essential insights into different spatial and temporal scales. Despite advances in measurement technologies and methodologies, there remains a pressing need for higher resolution data, improved spatial coverage, and better integration between observation systems to reduce uncertainties in emission estimates(Erland et al. 2022; Lyon et al. 2015; Sawyer et al. 2022). Addressing these gaps is critical for developing more accurate inventories, refining climate models, and implementing effective mitigation strategies.

In the bottom-up emission inventory method, emissions from sources like valves, pumps, or wellheads (commonly found in the oil and gas industry) are either sampled or modeled based on their leak rates, which are determined using specific instrumentation. Once a representative leak rate is established, it is multiplied by the number of components (e.g., valves, wellheads) to estimate total emissions, often calculated at the facility or basin level for the oil and gas sector. A typical example of this is the EPA Greenhouse Gas Inventory (GHGI), which uses asset-based emission factors. While this approach can estimate emissions across a broad scope, it does not identify individual emitters, making it less useful for precise emissions reporting or for achieving targeted reductions, such as in net-zero initiatives.

On the other hand, the top-down emission inventory method estimates methane emissions by measuring atmospheric concentrations of CH_4 using airborne or satellite sensors. The data collected over a given area is then disaggregated to estimate the emission rates from specific components or facilities. However, both bottom-up and top-down method in estimating CH_4 have big uncertainties, which will be further introduced in Section 2.4.3. The key challenge in top-down methods is converting measured CH_4 concentrations into accurate emission rates, which is critical for developing an emissions inventory that can meaningfully guide emissions reduction strategies. Current methods are in Table 2.7.

Table 2.7 CH_4 flux inverse modeling approaches

Principle Category	Method	Description	Strengths	Limitations	References
Mass Conservation Based	Local Mass Balance	Estimates CH_4 emissions by integrating the concentration across a defined plane downwind of the source.	Simple to implement; useful for local or regional flux estimation	Highly dependent on accurate wind speed and direction; Often need aircraft campaign to collect vertical CH_4 profile	Cambaliza et al. (2014); Johnson and Johnson (1995); Spokas et al. (2006)
	Gauss's Theorem Method	The outward flux summed along a contour surrounding the point source	Closed circle, good for single or contained sources	Highly dependent on accurate wind speed and direction; also need CH_4 concentration observations	Conley et al. (2017); Ryoo et al. (2019)
	Integrated Mass Enhancement	Based on satellite observations: The total mass enhancement in the plume is related to the magnitude of emission with a parameterization dependent on wind speed.	Useful for large-scale emissions detection and satellite data utilization	Relies on assumptions about atmospheric mixing and wind patterns; cannot resolve small-scale or intermittent emissions	Bhardwaj et al. (2022)
	Angular Width	Based on satellite observations: Infer source rates without independent wind information	Provides an alternative to wind-measurement-dependent models; useful when meteorologi	Assumes uniform plume dispersion; sensitive to plume geometry and wind patterns	Jongaramrungruang et al. (2019)

		by using the plume angular width as a measure of wind speed.	cal data is limited		
	Tracer Correlation Method	Releasing known quantities of tracer gas(es), e.g., N_2O close to a suspected source, the unknown methane flow was deduced based on the known tracer flow and the measured concentration enhancements	Doesn't require detailed atmospheric dispersion modeling; can be deployed in varied environments	Requires separate tracer gas release, which can be logistically difficult	Galle et al. (2001); Sisterson et al. (2016)
Gaussian Dispersion Based	Gaussian Plume Model	Assumes the CH_4 concentration emitted from a point source follows a Gaussian distribution in space.	Well-suited for point-source emissions; simple and easy to use	Highly dependent on accurate wind speed and direction; also need CH_4 concentration observations	Grauer et al. (2018); Matacchiera et al. (2019); Varon et al. (2018)
Lagrangian Particle Dispersion Based	Lagrangian Stochastic Particle Dispersion Model	Simulates the transport and dispersion of CH_4 using particle trajectories in the atmosphere.	More accurate than Gaussian models in complex environments; accounts for surface roughness and non-uniform meteorological conditions	Highly dependent on accurate meteorological inputs	Gao et al. (2008); Gao et al. (2009); Laubach and Kelliher (2005)

Bayesian Theory Based	Ensemble Kalman Filter (EnKF)	Assimilates CH_4 observational data to iteratively update model states, using an ensemble forecast.	Dynamically accounts for uncertainties in model states and measurements; handles time-dependent variations	Computationally demanding; requires a high-quality ensemble of meteorological inputs	Bisht et al. (2023); Platonova and Klimova (2021)
	Variational Method (4DVar)	the model's posterior over time is adjusted to minimize the discrepancies between the model output and observations of methane emissions over a time window.	Allows for dynamic error evolution, providing detailed spatiotemporal corrections of methane fluxes.	Computationally expensive and requires an adjoint model, which can be difficult to develop.	Bannister and Wilson (2024); Wilson et al. (2014)
	Markov Chain Monte Carlo	It samples from the posterior distribution of model parameters or state variables, providing a probabilistic estimate by generating a large number of samples.	Provides a thorough exploration of parameter space; useful for uncertainty quantification in methane emissions estimation	Can be slow to converge; computationally demanding	Western et al. (2021)
	Other Bayesian inference Based Methods	Bayesian inference techniques estimate CH_4 emissions by iteratively updating a prior emission	Uses probabilistic framework; effectively incorporates uncertainties in the model and data,	Computationally expensive; sensitive to prior assumptions, and convergence can be slow	Cusworth et al. (2021b); Thompson et al. (2017)

		estimate using observational data and optimizing the posterior distribution of the emission.	handles non-linear dynamics well	depending on the complexity of the model	
Machine Learning Based	Convolutional Neural Network	Machine learning-based approach that learns from observed methane concentrations to estimate emission sources by identifying spatial patterns.	Highly adaptable to large datasets; can discover complex, non-linear relationships between emissions and observed concentrations	Requires large amounts of data to train; susceptible to overfitting, and can be difficult to interpret	Jahan et al. (2024)
	Random Forests	Machine learning approach that aggregates decision trees to predict methane emissions based on various input variables, such as meteorological conditions and observed concentrations.	Handles complex interactions between variables well; robust against overfitting with appropriate tuning	Requires careful feature selection; may not generalize well beyond training data	Irvin et al. (2021); Räsänen et al. (2021)

2.4.3 Current CH_4 inventories

CH_4 inventories are essential inputs for atmospheric models, as they provide a comprehensive understanding of CH_4 emissions from various sources across different regions and sectors (Sicard et al. 2021; Zhang et al. 2012). These inventories help quantify the amount and distribution of CH_4 released into the atmosphere, allowing models like WRF-Chem to simulate CH_4 transport, transformation, and its overall impact on climate (Beck et al. 2013; Callewaert et al. 2022).

Accurately estimating CH_4 emissions from livestock remains a significant challenge due to various uncertainties inherent in both bottom-up and top-down inventory approaches. These uncertainties arise from the reliance on input data, methodological assumptions, and the limitations of current observational and modeling frameworks.

Bottom-up inventories estimate CH_4 emissions by combining activity data, such as livestock population counts, with emission factors that quantify CH_4 released per animal under specific conditions. While this approach provides detailed sectoral insights, several sources of uncertainty compromise its accuracy.

The primary sources for activity data in U.S. livestock CH_4 inventories are FAOSTAT (Tubiello et al. 2013) and USDA Boryan et al. (2011), which compile information on livestock population counts and associated agricultural practices. However, uncertainties arise due to variations in reporting methods, time lags, and generalizations about livestock management practices, such as diet and housing conditions. For the manure management, the distribution of manure in different manure management systems is also a source of uncertainty (Hristov et al. 2017; Solazzo et al. 2021). Additionally, the coarse spatial resolution activity data often fails to capture regional or localized differences in livestock density, particularly in areas with concentrated animal feeding operations. Temporal changes, such as shifts in livestock numbers or management practices driven by economic or environmental factors, further contribute to uncertainties in activity data.

Emission factors (EFs), which quantify CH_4 emissions per animal, also introduce significant uncertainties. These factors depend on processes like enteric fermentation and manure management and are derived from empirical studies generalized for global or national applications. Variability in livestock type, diet, digestion efficiency, and metabolic rates leads to substantial differences in enteric fermentation emissions. Similarly, manure management emission factors are influenced by environmental conditions such as temperature, moisture, and storage practices. Studies (Solazzo et al. 2021) suggest that EF uncertainties in global inventories like EDGAR can reach ±50%. Furthermore, emission factors are often derived from limited field studies, lacking region-specific data to reflect local agricultural practices accurately.

Another critical source of uncertainty is the interdependence of bottom-up inventories. Many inventories are not entirely independent, as they frequently rely on shared activity data sources. For example, both EDGAR and USEPA inventories use livestock activity data from FAOSTAT and USDA, propagating shared uncertainties. Additionally, other livestock-specific inventories like the Community Emissions Data System (CEDS, Hoesly et al. (2018)) often reference EDGAR or USEPA data, further amplifying shared errors and assumptions.

Top-down inventories estimate CH_4 emissions by combining atmospheric CH_4 concentration measurements with inverse modeling techniques. These approaches can improve the spatial representation of emissions, but they are not free from significant uncertainties.

One major limitation of top-down inventories like Basu et al. (2022); Nesser et al. (2024); Worden et al. (2022) is their dependence on bottom-up inventories as prior inputs to guide the optimization process. As a result, uncertainties in activity data and emission factors from bottom-up methods propagate into top-down estimates. Furthermore, observational data from satellite instruments like TROPOMI and GOSAT introduces its own uncertainties. Retrieval algorithms are affected by factors such as cloud cover, surface reflectance, and instrument calibration, while spatial and temporal resolution limitations may miss small-scale or episodic emissions(Worden et al. 2022).

To address the limitations of coarse-resolution bottom-up and top-down approaches, local-scale inventories have emerged as a promising solution. These inventories focus on specific, small-scale emission sources and leverage high-resolution measurement techniques to complement larger-scale inventories.

One such approach is the mass balance method, a top-down technique that estimates CH_4 emissions from atmospheric CH_4 concentrations by integrating wind speed and direction to calculate fluxes. This method has proven effective for capturing emissions from localized sources, such as CAFOs and feedlots. However, its accuracy depends on the availability of high-quality meteorological data and precise CH_4 measurements, which are not always accessible in all regions.

Local-scale inventories provide critical insights into emission hotspots often underestimated or missed in national or global inventories. By incorporating high-resolution observations and focusing on specific sources, these inventories help refine broader CH_4 estimates and improve the accuracy of emission inventories.

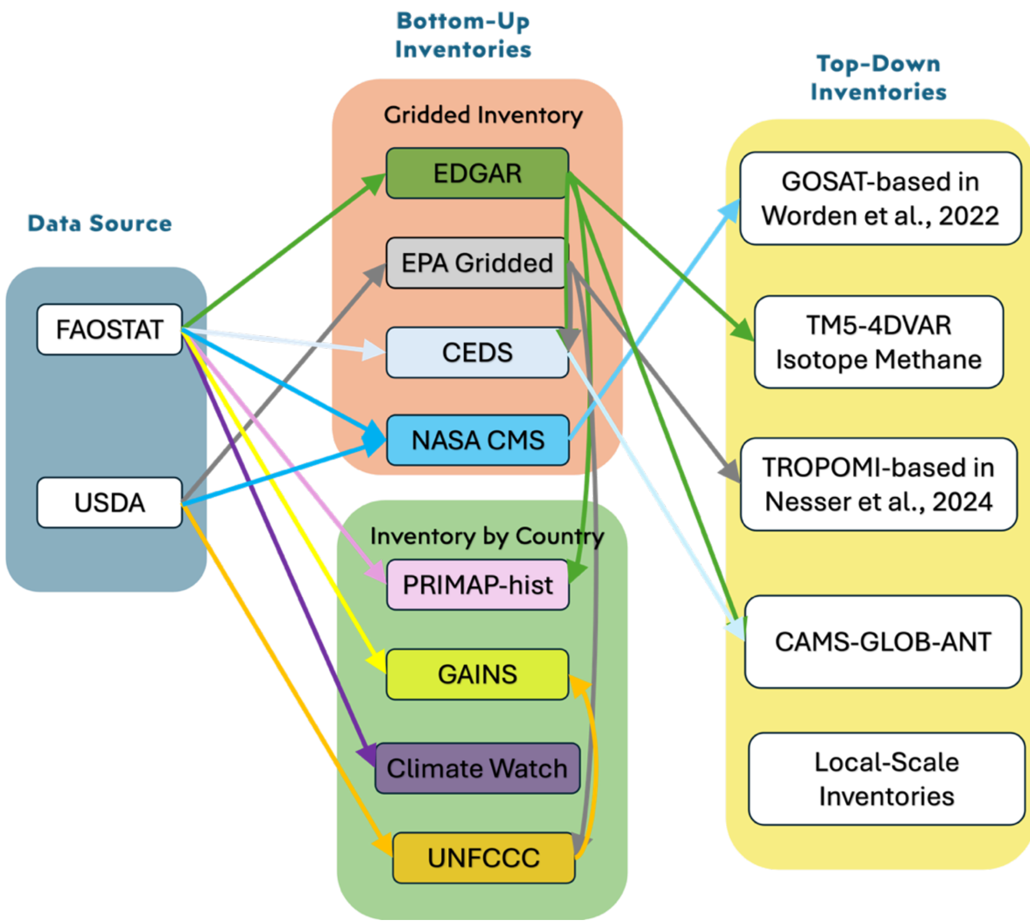

Figure 2.3 Overview of current bottom-up and top-down CH_4 inventories with their data sources, dependencies, and interconnections.

Chapter 3 Noah-MP Parameter Optimization at Southern Great Plains Using Bayesian Optimization

3.1 Introduction

Land-surface processes are of utmost importance in understanding energy, mass, and momentum exchanges and re-distributions between land and the atmosphere. Characterization of the critical mechanisms that underpin land-surface processes is fundamental in quantifying and distinguishing the interactions and feedback between the planetary boundary layer (PBL), the land surface, and the subsurface layer under different soil-vegetation system conditions (Kollet and Maxwell 2008). Most published studies indicate a tight correlation between surface energy fluxes, especially sensible heat fluxes (HFX) and latent heat fluxes (LH), and the structure and evolution of the PBL (Betts et al. 1996; Helbig et al. 2021; Jaeger et al. 2009; Sellers et al. 1997a; Wang and Dickinson 2012).

Over the past few decades, land surface models (LSMs) have undergone significant development, evolving from simple bucket models (Fisher and Koven 2020; Pitman 2003) to more complex models that incorporate the various interactions and feedbacks between physical, chemical, and biological processes. Despite these advancements, the accuracy of these LSMs such as the community Noah LSM with multiparameterization options (Noah-MP) is often compromised by inherent biases. These biases in current land surface models such as Noah-MP primarily originate from three primary errors (Clark et al. 2011; Duan et al. 2006; Wang et al. 2009): (1) an imperfect model structure; (2) inappropriate model parameter values (PVs); and (3) incorrect model inputs, including meteorological forcing data and initial surface conditions.

Numerous research efforts have concentrated on addressing the imperfections inherent in model structures (Collatz et al. 1991; Deardorff 1978; Dickinson 1984; Dickinson et al. 1998;

Jarvis 1976; Manabe 1969; Milly and Shmakin 2002a, 2002b; Niu et al. 2011; Sellers et al. 1997b; Yang et al. 2011). However, the imperfections of model structure can be difficult to address because they are often rooted in the fundamental assumptions and approximations used in model development. Making changes to the model structure can require a significant amount of time and resources and may also require a deep understanding of the underlying physical processes being simulated. On the other hand, significant strides have been made in improving the accuracy of model inputs, particularly meteorological forcing data. These improvements have been driven by advances in observational technologies, such as satellite remote sensing and weather radar, as well as by the development of more sophisticated data assimilation techniques (Dee et al. 2011; Gelaro et al. 2017; He et al. 2020; Kobayashi et al. 2015). Another effective strategy for reducing the biases in LSMs is by modifying the model parameters. LSMs often rely on empirical equations with adjustable parameters that can be fine-tuned to enhance model performance, accounting for varying soil types, vegetation cover, and meteorological conditions (Cuntz et al. 2016). The applicability of these parameters can vary depending on the model's scale and resolution. For instance, a global-scale model can necessitate different parameters compared to a regional or local model, reflecting the diversity in land characteristics at different scales (Clark et al. 2015; Fang et al. 2016).

Sensitivity analyses have revealed LSM's responsiveness to variations in soil and vegetation parameters, impacting not only hydrological cycles but also energy and carbon fluxes (Arsenault et al. 2018; Lu et al. 2013; Prihodko et al. 2008; Rosolem et al. 2012). Given that such sensitivity is highly site-specific, a subtle calibration of these parameters is essential. Taking the SGP site as an example, where the soil classification in the county (Grant County, Oklahoma) varies from sandy to clayey soils (Williams et al. 1985). In LSMs, variations in soil composition are reflected through distinct soil parameter values. These soil parameters in LSMs are of vital importance as they directly affect the simulation of multiple processes, including the energy and water balance at the Earth's surface (Garrigues et al. 2018; He et al. 2023; Montaldo et al. 2003). These processes, in turn, have significant impacts on the atmosphere, weather, and climate. Accurate soil parameter selections in LSMs are crucial for enhancing the modeling of land-atmosphere interactions. Soil parameters not only describe the physical properties of the soil, but also influence the simulated vegetation characteristics, such as stomatal resistance. Thus, the careful selection and adjustment of soil parameters is crucial for the tailored application and accuracy of models like Noah-MP, ensuring that they reflect the dynamic and variable nature of land-surface processes.

An offline LSM refers to an independent simulation, without real-time integration or data exchange with other models like WRF. While offline LSMs are valuable for direct surface energy budget assessments, they fall short in capturing the dynamic interactions with the atmosphere (Laguë et al. 2019). Coupled land-atmosphere models, like WRF/Noah-MP, address the interactions by coupling terrestrial and atmospheric processes, which enables the representation of complex feedback mechanisms (Blyth et al. 2021). For instance, high HFX accompanied by PBL growth might increase PBL turbulence, and in turn alter HFX and LH (Misra 2020). One primary motivation for using coupled models like WRF/Noah-MP is to understand the complex interactions between the land surface and the atmosphere. Furthermore, coupled models enable researchers to study the potential impacts of land-use changes on local and regional climate, assess the feedback mechanisms arising from various terrestrial and atmospheric interventions, and provide more holistic predictions in the face of evolving climate change scenarios.

Addressing the computational challenges inherent in parameter optimization in WRF/Noah-MP, our study leverages Bayesian Optimization (BO), a technique selected for its efficiency and speed. Traditional parameter optimization methods, such as Markov Chain Monte Carlo (MCMC), require an impractical number of iterations (10^4–10^6 iterations) to achieve convergence (Hassan et al. 2009; Lu et al. 2017; Ma et al. 2022; Tan et al. 2022) — potentially taking years for completion even with our idealized single-column WRF/Noah-MP. BO offers a tractable alternative that accelerates the discovery of optimal solutions, thereby facilitating global optimization within a feasible time frame. This is particularly critical when model time steps are less than one minute, where computational demands escalate dramatically.

This study builds on this foundation, delving into the sensitivity of WRF/Noah-MP to vegetation, soil, and general parameters. As detailed in section 3.3.1, we identified seven critical parameters through sensitivity analysis. These parameters include the pore size distribution index (BEXP), saturated soil hydraulic conductivity (DKSAT), saturated soil hydraulic diffusivity (DWSAT), porosity (SMCMAX), volumetric soil water content at field capacity (SMCREF), wilting point soil moisture (SMCWLT), and soil quartz content (QUARTZ), all optimized using BO to ascertain their effect on atmospheric state and flux variables. The selection of a nine-day period from 2-10 April and the April and May 2016 alfalfa growing season at the Southern Great Plains (SGP) site was strategic, aiming to reflect the unique soil and vegetative characteristics of the location.

Through the calibration of optimized parameters against the primary soil constituents—sand, silt, and clay, our goal is to deepen our understanding in land-atmosphere exchanges and adjust the Noah-MP model to represent energy fluxes and near-surface meteorological state variables more accurately that are relevant to specific site characteristics.

Ultimately, this manuscript presents a comprehensive optimization study that contributes to the fine-tuning of LSMs for improved simulation accuracy, with broader implications for meteorological forecasting and climate science and the potential for such methodologies to be extended to regional scales.

3.2 Data

3.2.1 AmeriFlux observations

Thermodynamic and kinetic observations of the atmosphere and soil along with eddy-covariance tower flux measurements from the AmeriFlux dataset located at the ARM SGP site (US-ARM, Biraud et al. (2023)) in Lamont, Oklahoma (Latitude: 36.6058°, Longitude: -97.4888°) are used for the parameter optimization: HFX, LH, and wind speed (WS) observations at 4.65m, air temperature and specific humidity observations at 3.94m, and top-layer soil moisture (SMOIS), top-layer soil temperature (TSLB) centered at 0.1 m under soil surface are used in the cost function (discussed later in Section 3.3.2) to determine the optimal set of parameter values for this site. The soil observations at 0.1m, 0.3m, 0.5m, and 1.0m below the ground surface are used to initialize the soil conditions in WRF/Noah-MP, The initial soil conditions in the model are based on measurements of soil moisture and temperature taken at depths of 0.1m, 0.3m, 0.5m, and 1.0m below the ground surface at SGP site. The Balloon-Borne Sounding System (SONDEWNPN, Keeler et al. (2019)) soundings at SGP site are also used in WRF/Noah-MP to initialize the atmospheric profile, including the u-component and v-component wind speeds, potential temperature, and atmospheric specific humidity taken at 25 different levels, starting from near the surface (about 1m above the ground) and extending up to approximately 16 km.

SGP site is characterized by an annual crop rotation system including winter wheat, corn, soybean, and alfalfa on a silt-clay-loam soil. Management records indicate that in April and May 2016, alfalfa was planted at SGP site. The management practices implemented at the SGP site during the period from May through September 2016 included multiple plantings, hay baling, herbicide applications, and fertilization. These practices are known to have diverse impacts on vegetation canopy, phenology, and carbon dynamics, as indicated by previous studies (Campioli et al. 2015; Wilson et al. 2013; Zhou et al. 2017). The selection of observations from April and May 2016 was motivated by the persistently high values of net ecosystem exchange (NEE) during this period according to AmeriFlux NEE observations, indicating vigorous plant growth and substantial carbon sequestration within plant tissues. The impacts from management activities can be complicated, for example, previous studies suggested that the conventional tillage typically reduces soil compaction within the tilled layer, leading to an increase in total porosity when compared to no-tillage practices. However, the impact on the distribution of different sized pores varies with soil type (Lipiec et al. 2006; Schjønning and Rasmussen 2000). Until May 25th, 2016, no management activities were documented, ensuring minimal external disturbances during this time frame. More details about the SGP site and the measurements are introduced in Sisterson et al. (2016).

3.2.2 Model configuration

The single-column WRF model (V3.9) is forced by the European Centre for Medium-Range Weather Forecasts (ECMWF) ERA5 (Hersbach et al. 2018) and ERA5-land reanalysis (Muñoz Sabater 2019) 6-hourly on 25 pressure levels. To investigate the effects of different forcing datasets, we also tested the Modern-Era Retrospective analysis for Research and Applications, Version 2 (MERRA-2, (Global 2015)) reanalysis data to drive our WRF/Noah-MP simulations. The resultant simulations driven by the two reanalysis exhibited negligible differences. The single-column simulation is conducted with 4 km × 4 km grid spacing centered at the SGP site – Crop type at SGP was all alfalfa in the grid in the study period. The model output domain has 47 vertical layers extending from the surface to 50 hPa. Noah-MP is implemented in WRF and provides 10 parameterization options representing 10 distinct land surface states and processes. The parameterization options in Noah-MP we chose are listed in Table 3.1, which are commonly used as default options (provided from the user's guide in Niu (2011)). Table 3.2 lists the WRF model configuration, which includes the Dudhia shortwave radiation scheme (Dudhia 1989), the rapid radiative transfer model (RRTM, Mlawer et al. (1997)) for longwave radiation, the Noah-MP land surface model (Niu et al. 2011; Yang et al. 2011), and the Yonsei University PBL scheme (Hong et al. 2006). The single-column WRF/Noah-MP offers a simplified approach. Unlike a 3D model, it lacks interactions and connections with surrounding columns. Precipitation prediction within a model can be intricate, leading to potential inaccuracies the single-column WRF/Noah-MP simulating precipitation. Notably, from 2-10 April, the weather was fair. To prevent imprecise simulations of precipitation and cumulus and avoid time periods with precipitation in the optimization, we disabled the microphysics and cumulus options. The Noah-MP model calculates the temperature and phase changes for the canopy, snowpack, and soil by taking into account the energy balance of the canopy and ground. Therefore, it does not include the simulation of energy balance residuals (threshold 0.01 $W \bullet m^{-2}$), which are commonly observed in eddy covariance measurements (Foken 2008).

In Noah-MP, Leaf Area Index (LAI) directly influences radiation (reflection, transmission, and absorption by vegetation), latent heat flux (canopy evaporation, transpiration), and CO_2 flux, with indirect effects like cooling from latent heat flux changes. In this study, prescribed LAI option is chosen in Noah-MP — LAI is calculated based on a linear interpolation between the specified LAI values for each day of the simulation and the LAI value from the previous month or the next month, which assumes that the LAI values change smoothly over time within each month. If the date falls before the 15th of the month, the daily LAI is based on both the previous month's and the current month's monthly LAI. Conversely, if the date falls on or after the 15th, the LAI is based on both the current month's and the following month's monthly LAI.

Table 3.1 Options chosen in Noah-MP in this study.

Physical process	Option used
Dynamic Vegetation	Prescribed LAI and shade fraction
Stomatal Resistance	Ball-Berry (Ball et al. 1987)
Soil moisture factor for stomatal resistance	Noah type (Chen et al. 1996)
Runoff and groundwater	SIMGM: based on TOPMODEL (Niu et al. 2007)
Surface layer drag coefficient	Monin-Obukhov
Supercooled liquid water	Standard freezing point depression (Niu and Yang 2006)
Frozen soil permeability	Uses total soil moisture to compute hydraulic properties (Niu and Yang 2006)
Radiation transfer	Two-stream with canopy gap equal to one
Snow albedo	CLASS (only considers overall snow age) (Verseghy 1991)
Frozen/liquid partitioning	Based on Jordan (1991)
Soil temperature lower boundary condition	Zero heat flux

Table 3.2 Summary of the configuration for the single-column WRF.

Physical process	Option used
Short wave radiation	Dudhia
Long wave radiation	Rapid radiative transfer model (RRTM)
Boundary layer	YSU
Microphysics	WRF single moment microphysics 5-class
Cumulus	Betts-Miller-Janjic
Land surface model	Noah-MP
Vertical levels	47
Horizontal resolution	4 km × 4 km
Time step	24 s
Meteorological initial conditions	OUN radiosonde soundings
Boundary conditions	Open boundary conditions
Meteorological forcing data	ERA5
Soil initial conditions	AmerifFlux measurements at SGP site

The default monthly LAI values in Noah-MP may not accurately represent the actual vegetation cover, hence we utilize the NOAA Climate Data Record (CDR) of AVHRR LAI as a more precise alternative (Vermote 2019), which is at a resolution of $0.05° \times 0.05°$. In the case of alfalfa growth at ARM in 2016, crop management recordings suggest that the alfalfa was laid down on May 25th to be prepared for baling, which may result in a decrease in LAI. Consequently, our simulations do not exhibit any abrupt decline in LAI or transpiration attributable to the harvesting event. Thus a linear regression was performed on the daily CDR LAI data, and manual LAI values of 1.344 $m^2 \bullet m^{-2}$, 1.450 $m^2 \bullet m^{-2}$, 1.561 $m^2 \bullet m^{-2}$, and 1.669 $m^2 \bullet m^{-2}$ were assigned for March, April, May, and June, respectively. These LAI values were used as inputs in Noah-MP to simulate the land surface processes during the growing season of alfalfa.

3.3 Methods

3.3.1 Sensitivity analysis

We applied a finite difference method, as introduced in Lenhart et al. (2002), to conduct a sensitivity analysis of the WRF/Noah-MP simulated model fields. This method estimates the partial derivative of the model's output in relation to each standard input parameter in the neighborhood of a chosen parameter value while holding all other parameters constant, which in this case includes vegetation, soil, and general parameters. By doing so, we aimed to identify the most sensitive parameters within the selected Noah-MP options, not to compute their exact values, but to identify which parameters the model output is most responsive to. Thus, we were able to assess the model's sensitivity to changes in active vegetation, soil, and general parameters in the vicinity of the default value. The sensitivity index is calculated by the finite difference centered on the default parameter value, which is an estimation of the sensitivity of the model output y to changes in the parameter x ($\frac{\partial y}{\partial x}$):

$$\frac{dy}{dx} = \frac{y_2 - y_1}{2\Delta x}, (3.1)$$

where Δx is the 25% of the default parameter value x_0, y_2 (y_1) is the nine-day model output (i.e., 2-meter air temperature (T2), 2-meter specific humidity (Q2), HFX, LH, 10-meter wind speed (WS), SMOIS, and TSLB) simulated with $x_0 + \Delta x$ ($x_0 - \Delta x$), and all other parameters remain unchanged to be default silty-clay-loam values. Our methodology only involves daytime simulations (i.e., y_1 and y_2 are data obtained during the period of 8 AM to 8 PM local time from 2-10 April). We then determine the hourly difference between y_1 and y_2 and compute the mean of these differences. It is important to note that this method is most effective when applied to monotonic functions, however, it can still provide a general understanding of the sensitivity of the WRF/Noah-MP model to each parameter when used in a simple sensitivity analysis. Moreover, the sensitivity of the model's output relative to the parameters is subject to the length of the simulation employed for the sensitivity analysis.

3.3.2 Bayesian Optimization and Experiment design

BO is an efficient method to optimize objective functions which are expensive to evaluate. BO is designed to solve the problem of finding a global minimizer (or maximizer):

$$x^* = \underset{x \in A}{\operatorname{argmin}} f(x),\ (3.2)$$

where x is the vector of tunable parameters in the space of interest A, and argmin represents the parameter set that yields the smallest possible values with given constraints. The method aims to find the x^* that achieves the minimum of the objective function $f(x)$ that depends on a "black-box" simulation model. In this study, the $f(x)$ is calculated as:

$$f(x) = \sum_{i=1}^{7} \frac{1}{2\sigma_i^2} \sum_{t} |obs_i(x,t) - sim_i(x,t)|^2, (3.3)$$

where $obs_i(x,t)$ and $sim_i(x,t)$ are the hourly observations and simulations of the variable i from April 2^{nd} 12UTC to 10^{th} 12 UTC in 2016 at the SGP site; σ_i^2 is the variance of all $obs(t)$ in these 10 days of i. The seven variables *i* are HFX, LH, T2, Q2, WS, SMOIS, and TSLB. We utilized the scikit-optimize (Head et al. 2021) library to perform BO calculations efficiently. BO relies on Bayesian inference and uses a probabilistic model to predict the objective function's behavior based on the observations made so far. BO's use of probabilistic modeling and Bayesian inference provides an efficient and effective framework for optimizing complex objective functions with a limited number of evaluations, making it a popular choice for hyperparameter tuning in machine learning and other optimization problems (Shahriari et al. 2015; Wu et al. 2019).

BO consists of two primary components: Gaussian process regression, which constructs a probabilistic model for the objective function, and an acquisition function, which directs the subsequent sampling point for evaluation.

First, a prior probability distribution over the function f is established through a set of initial samples. The sampling method and the number of the initial samples can determine how evenly the samples are distributed in the parameter space and how fast the convergence can be achieved. We used the Hammersley sampling method (Diwekar and Kalagnanam 1997). This approach provides an evenly distributed foundation for subsequent iterations, as evidenced by the uniformity shown in Figures 3d and 4d of Diwekar and Kalagnanam (1997).

Having a sufficient number of initial samples is advantageous for obtaining a more accurate initial estimate of the prior distribution of f. In Diessner et al. (2022), five initial samples per input dimension were used for BO. While augmenting the number of initial samples can enhance the

BO performance, it also increases computational time (Munoz-González 2017). Consequently, we opted for 70 initial samples, equal to 10 samples per input dimension, to balance efficiency and computational demand.

Following the allocation of 70 initial samples using the Hammersley sampling method, our BO algorithm progresses iteratively to refine the model. Each iteration begins with updating the Gaussian process' posterior probability distribution for the objective function f. The next sampling point x_n is selected by maximizing the acquisition function against this updated distribution, a step that navigates the trade-off between exploring new potential areas and exploiting known regions to optimize f. After evaluating f at x_n, we increment the iteration count and continue this cycle until the minimum of f value does not change in recent 50 iterations, which is considered converged. In our BO method, we employ the model from the final iteration as a surrogate to guide subsequent exploration. Specifically, we perform 10^6 iterations within a seven-dimensional parameter space, corresponding to the parameters outlined in Table 3.3, each of which spans a specific range also in Table 3.3. This iterative process, leveraging the surrogate model, allows us to efficiently explore the multi-dimensional parameter space and identify optimal or near-optimal values. Unlike the optimization component, this step can be done in parallel for each parameter set.

The acquisition function we chose is the expected improvement (EI), which is a common choice for acquisition function (Ma et al. 2020). One of the advantages of EI is that it automatically balances between exploration and exploitation based on the learned model. The parameter values tested in the iteration $n + 1$ is determined by the EI in the iteration n (EI_n):

$$x_{n+1} = argmax\ EI_n(x), (3.4)$$

where $argmax$ denotes the parameters that give the largest possible values with given constraints.

Table 3.3 The description and units of the parameters we optimized and physical processes they involved. The original values for sand, silt, clay, and silty clay loam of each parameter and the optimized values are also given.

Parameter	**BEXP**	**DKSAT**	**DWSAT**	**SMCMAX**	**SMCREF**	**SMCWLT**	**QUARTZ**
Description	Pore size distribution index	Saturated soil hydraulic conductivity	Saturated soil hydraulic diffusivity	Porosity	Volumetric soil water content at field capacity	Wilting point soil moisture	Soil quartz content
Sand	2.79	46.6×10^{-6}	2.65×10^{-5}	0.339	0.236	0.01	0.92
Silt	3.86	2.18×10^{-6}	1.66×10^{-5}	0.484	0.383	0.061	0.1
Clay	11.55	0.974×10^{-6}	1.22×10^{-5}	0.468	0.412	0.138	0.25
Optimization Range	2.79 – 11.55	0.974×10^{-6} – 46.6×10^{-6}	0.608×10^{-6} – 2.65×10^{-5}	0.339 – 0.484	0.236 – 0.412	0.01 – 0.138	0.0 – 1.0
Default Silty Clay Loam Value	8.72	2.08×10^{-6}	2.35×10^{-5}	0.464	0.387	0.12	0.1
Optimized Value (Percent change)	3.94 (-54.8%)	8.79×10^{-6} (+322.6%)	1.56×10^{-5} (-33.6%)	0.471 (+1.5%)	0.314 (-18.9%)	0.128 (+6.7%)	0.5 (+400%)
Units	–	$m\ s^{-1}$	$m^2\ s^{-1}$	$m^3\ m^{-3}$	$m^3\ m^{-3}$	$m^3\ m^{-3}$	$m^3\ m^{-3}$
Involved Physical Processes	Soil hydraulic conductivity; Plant photosynthesis; Soil water evaporation	Soil hydraulic conductivity	Soil water diffusivity	Soil water evaporation; Soil thermal diffusivity and conductivity	Plant photosynthesis related to soil moisture	Plant photosynthesis related to soil moisture; Soil water evaporation	Soil thermal diffusivity and conductivity

As in Figure 3.1, we performed 300 iterations after the initial 70 iterations to assure convergence. In fact, the optimization process tends to converge at about 100 iterations after initial 70 iterations. However, to ensure convergence, additional iterations up to 300 were added to the optimization process.

The optimizations are based on nine fair-weather-day observations from April 2^{nd} through 10^{th} in 2016 at the SGP site. We then use the optimized parameters to run WRF/Noah-MP for a two-month period from April to May 2016 to determine if the optimization technique improves simulations throughout the alfalfa growing season in that year. One limitation of the idealized single-column WRF is the difficulty in accurately simulating precipitation since the model is only able to represent a single vertical column of the atmosphere and is not able to take into account the complex interactions and processes that lead to precipitation. In simulating the two-month period from April to May 2016, to overcome this limitation of inaccuracy in simulating precipitation, we restart the simulation at the time of precipitation event when there is an abrupt increase in soil moisture. Our single-column WRF/Noah-MP restarts with the observed soil moisture and SONDEWNPN soundings at SGP site on 11 April at 18 UTC, 17 April at 18 UTC, 20 April at 00 UTC, 27 April at 06 UTC, and 17 May at 12 UTC. This approach helps to avoid significant biases in the simulation of land surface moisture characteristics, allowing for more accurate results.

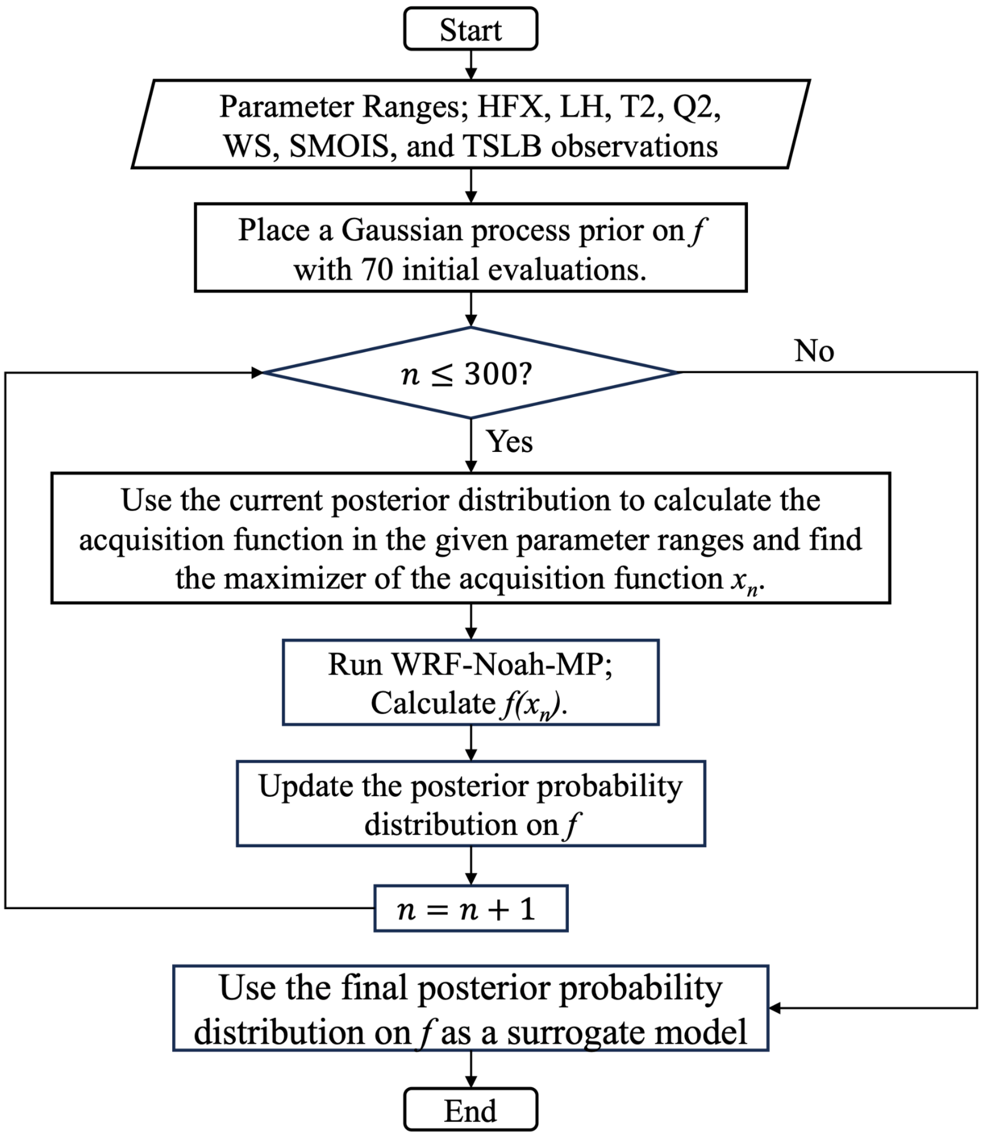

Figure 3.1 Schematic of the single column WRF/Noah-MP parameter optimization with BO.

3.4 Results

3.4.1 Sensitivity Test results

In our sensitivity analysis (described in Section 3.3.1), we examined the impact of 33 active parameters from MPTABLE.TBL, SOILPARM.TBL, and GENPARM.TBL on the WRF/Noah-

MP's simulations. These parameters, as selected in Table 3.1, were evaluated for their influence on HFX, LH, T2, Q2, WS, SMOIS, and TSLB by calculating sensitivity indices. Our analysis highlighted that parameters like BEXP, DKSAT, DWSAT, SMCMAX, SMCREF, SMCWLT, and QUARTZ, which influence soil characteristics, had a significant impact on these variables, thus warranting their optimization. While certain vegetation and radiation parameters, such as leaf reflectance and transmittance in the near-infrared spectral band (RHOL-nir: leaf reflectance in the near-infrared spectral band, TAUL-nir: leaf transmittance in the near-infrared spectral band) and physiology parameters like VCMX25 (the maximum carboxylation rate at 25℃) and MP (the slope of Ball-Woodrow-Berry stomatal conductance formulation) showed sensitivity, their influence was less pronounced on TSLB and SMOIS. Moreover, the Planetary Boundary Layer Height (PBLH) was found to be particularly sensitive to soil parameters, which aligns with the YSU PBL scheme used in our simulations. This scheme balances surface heating (HFX) against the entrainment of more stable air above the PBL, indicating that stronger surface HFX lead to a deeper PBL and vice versa (Garratt 1994; Stull 1988). Table 3.3 provides a detailed overview of these seven soil parameters, including their default and optimized values. These parameters are crucial for simulating soil thermal conductivity and diffusivity, hydraulic conductivity, water evaporation, and plant photosynthesis related to soil water in Noah-MP.

3.4.2 Optimization results

3.4.2.1 Overview of optimization results

The optimization outcomes detailed in Table 3.3 reveal that the values for DKSAT SMCMAX, and QUARTZ are optimized to exceed their default values, while BEXP, DWSAT, SMCREF, and SMCWLT are reduced. This divergence from default parameters indicates a discrepancy between the model's assumptions and the actual soil properties at our study site, emphasizing the need for site-specific calibrations. Such discrepancies have important implications on soil water movement and heat conduction, plant water availability and evapotranspiration, which affect surface energy fluxes.

Figures 3.2 and 3.3 provide empirical support for these parameter optimizations. Figure 3.2 illustrates the cost function's sensitivity to individual parameter changes while holding others constant at their optimized values, offering a detailed examination of the influence each parameter exerts on the model's performance. The 95% confidence intervals depicted in the figure 3.2 underscore the certainty of these relationships across the parameter's range.

Figure 3.3 illustrates the selection of 1000 samples out of the 10^6 generated using the Latin hypercube sampling method. These 1000 samples represent the instances where the cost function values are the smallest. This analysis adopts the BO approach's last iteration as the best representation of the cost function distribution across the seven-dimensional parameter space. By executing an additional 10^6 iterations based on this final iteration, we obtain a histogram that highlights the most probable regions for the optimal parameter values. The peaks of this histogram represent the confluence of reduced cost function values, indicating where the model's simulations align most closely with observational data. It's important to note that the optimization of parameter values is not confined to a single fixed value by providing such a histogram. Instead, parameter values occurring with higher frequency exhibit a greater likelihood of enhancing the performance of Noah-MP simulations.

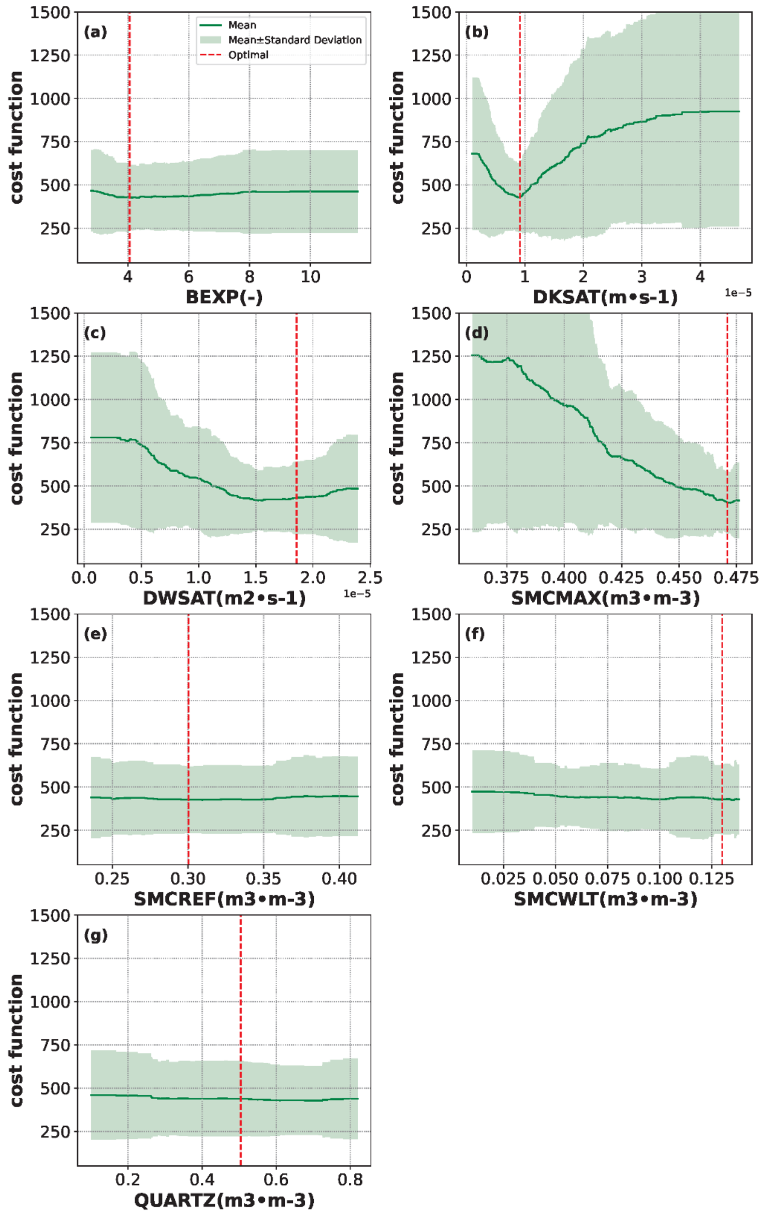

Figure 3.2 Visualization of BO results for selected soil parameters: (a) BEXP, (b) DKSAT, (c) DWSAT, (d) SMCMAX, (e) SMCREF, (f) SMCWLT, and (g) QUARTZ. Each subplot includes the predicted cost function trajectory (green solid line) across varying parameter values, with green shaded regions representing 1.96 standard deviations, indicating prediction uncertainties. Red dashed lines pinpoint the optimal parameter values.

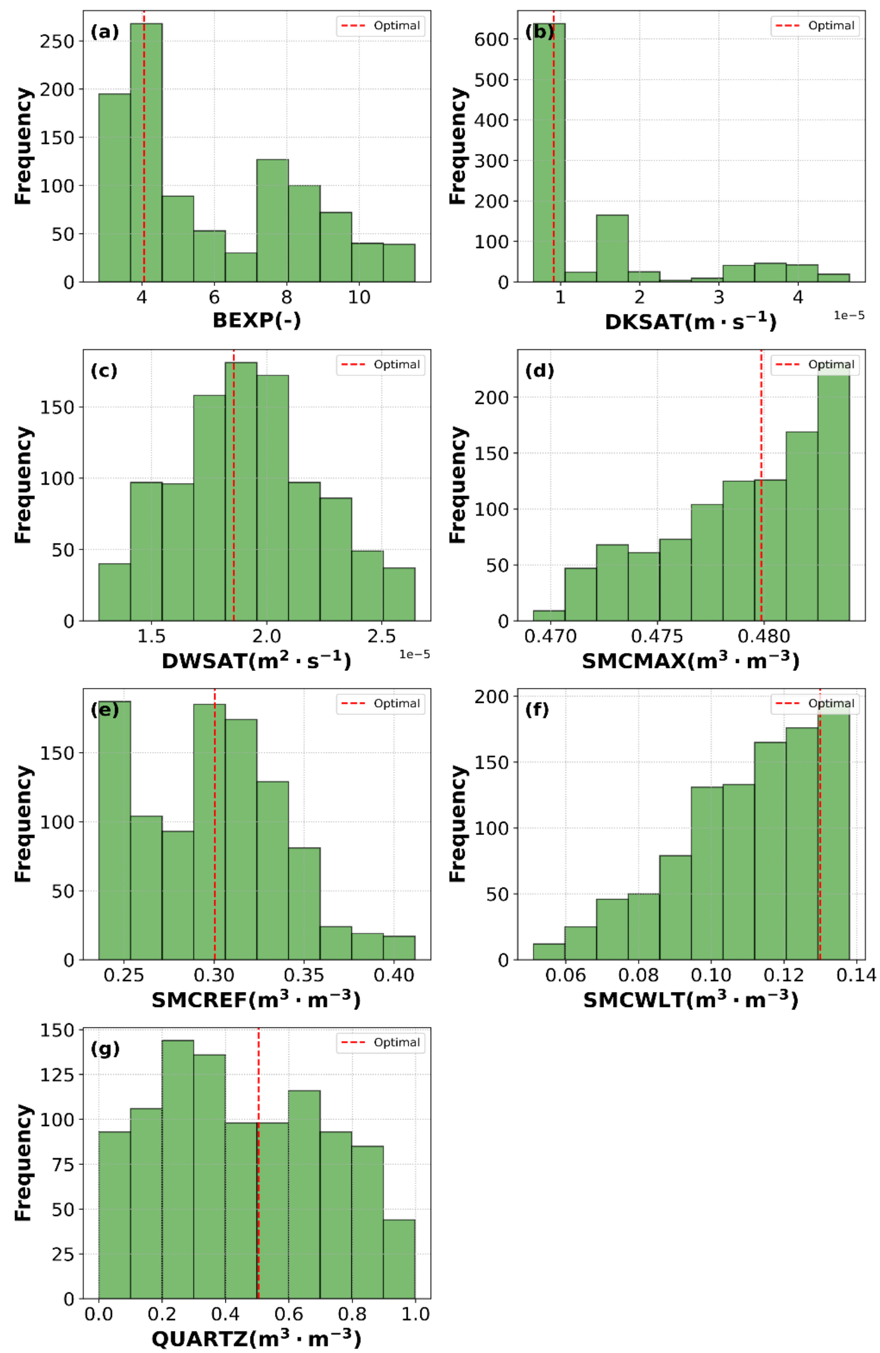

Figure 3.3 The histogram of 1000 samples represent the instances where the cost function values are minimized with respect to (a). BEXP, (b). DKSAT, (c). DWSAT, (d). SMCMAX, (e). SMCREF (f). SMCWLT, and (g) QUARTZ. The vertical red dashed lines represent the optimized value corresponding to each parameter.

3.4.2.2 Effects of soil parameter variations on land surface characteristics

The overall outcome of the optimization process is an enhancement in soil water percolation, which subsequently leads to a reduction of simulated water content in the surface soil layer, despite starting with the same initial soil moisture levels. This drier condition of the soil is associated with an increase in HFX and a decrease in LH at the soil surface as shown in Fig 3.4 (a) and (b), with a more pronounced effect during the last 5 days from 6 April. The observed daily mean soil moisture between April 3rd and 9th reveals a decreasing trend of -0.0040 $m^3 \bullet m^{-3}$per day. The simulated results with optimized parameters yield a similar trend of -0.0059 $m^3 \bullet m^{-3}$per day, while the simulation with the default soil parameter values predict a slower decrease – more than -0.001 $m^3 \bullet m^{-3}$ (less negative) per day. During the nine-day period without precipitation (2-10 April), simulations using default parameters overestimated LH, suggesting an over-prediction of evapotranspiration. This discrepancy is partly attributable to the original DKSAT values, which likely underestimated the actual soil percolation rates at the site. The optimization adjustments increased DKSAT values, aligning simulations more closely with observed percolation trends and offering a better representation of matric potential changes. This improvement is critical as the single-column WRF/Noah-MP model does not simulate horizontal soil water flow, necessitating accurate vertical percolation rates for realistic soil moisture and energy flux predictions.

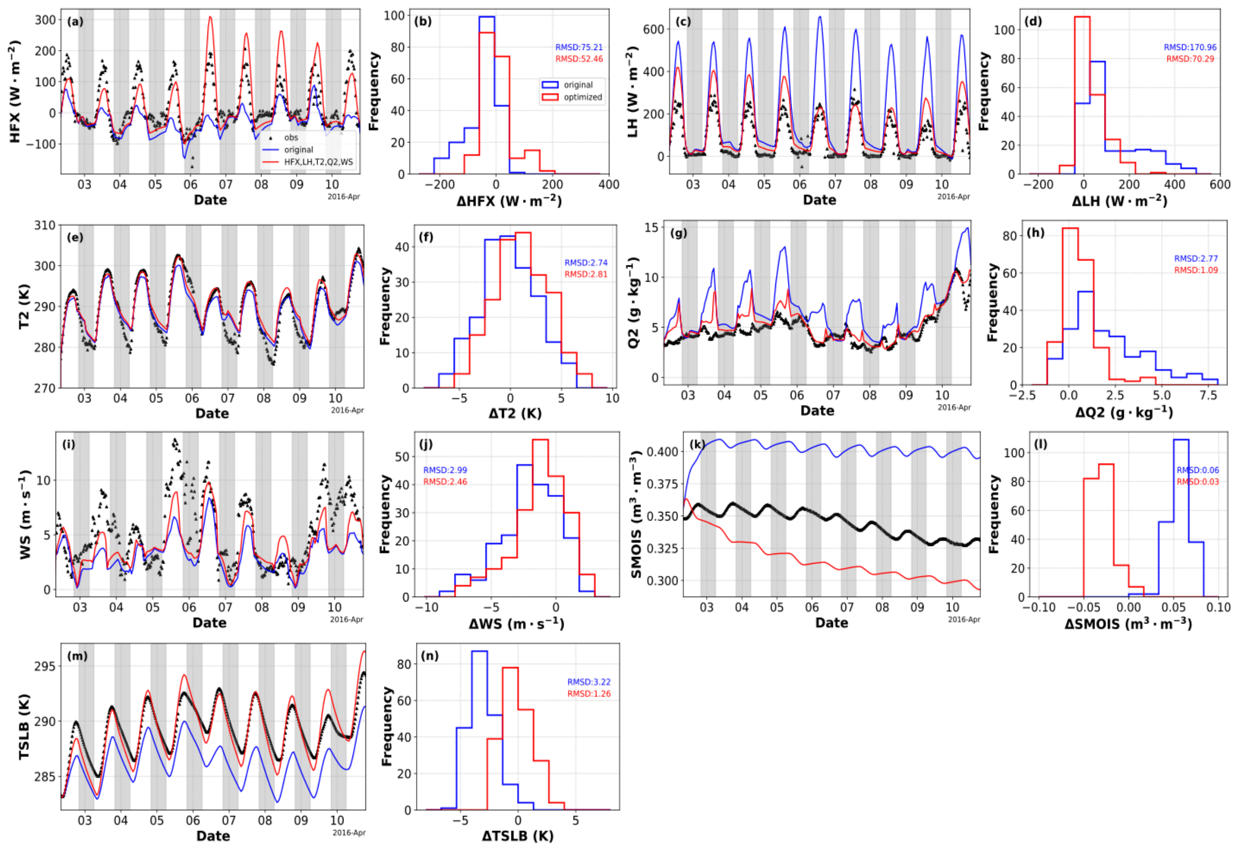

Figure 3.4 (a) HFX simulated by WRF/Noah-MP with default values of the seven parameters (blue line) and the optimized parameters (red line) compared to the observations at the SGP site (black triangle) from April 2nd to 10th. The gray shades represent nighttime (8 PM – 8 AM). Similar for (c), (e), (g), (i), (k), and (m) but for LH, T2, Q2, WS, SMOIS, and TSLB. (b) The blue histogram is for the simulated HFX with original values of the seven parameters minus the observation at the SGP site, red histogram is for the simulated HFX with the optimized parameters minus the observation at the SGP site. Similar for (d), (f), (h), (j), (l), and (n) but for LH, T2, Q2, WS, SMOIS, and TSLB correspondingly.

In Noah-MP, DWSAT is positively correlated with soil water diffusivity, indicating that soils with higher DWSAT values promote more efficient water movement and facilitate enhanced redistribution within the soil profile. Soil water diffusivity influences the distribution of moisture content at various depths by affecting the rate of water movement within the soil matrix. Generally, increased soil water diffusivity accelerates water movement through the soil, leading to a more extensive dispersion of soil moisture simulations across different depths. This, in turn, results in a more uniform vertical distribution of soil moisture as water rapidly infiltrates from the surface to deeper layers if the surface is dryer than the deeper soil, replenishing moisture in the lower soil strata, and conversely, moving upwards when deeper layers are drier than the surface. Consequently, this leads to a uniform availability of water for plant root systems throughout the entire soil profile simulations. In this study, the initial soil conditions from the AmeriFlux soil moisture profile indicate that deeper soil layers (1.5m under soil surface) are moister than the surface layer (0.1m under soil surface).

When DWSAT is reduced, soil moisture simulations indicate less dispersion between the surface and deeper soil layers compared to the default simulation, leading to a relatively drier surface layer and a moister deeper layer. The decrease in DWSAT has a similar effect to that of decreasing DKSAT, namely a greater HFX and lower LH simulation during daytime.

BEXP is a fitting parameter in determining the soil water characteristic curve and is intrinsically linked to the soil texture, as evidenced by previous research (Sakaguchi and Zeng 2009). The equation for BEXP in Noah-MP follows the soil wetness functions in Sakaguchi and Zeng (2009). This parameter governs the exponent value in the exponential decay of saturated soil water diffusivity and conductivity. Like the behavior exhibited by DKSAT and DWSAT, a decrease in BEXP results in a drier soil surface and an increase in soil surface resistance for ground evaporation in the model. If we neglect the dependence between the seven parameters and keep other six parameters except BEXP at the default value, the changes in BEXP itself listed in Table 3.3 results in an approximate increase of 12.1 $W \bullet m^{-2}$ (+10.4%) in transpiration at noon from 2 April to 10 April. Moreover, the augmentation of BEXP leading to a subsequent decrease in the simulated canopy temperature has been found to provoke a decrease in the under-canopy evaporation as simulated in Noah-MP, estimated at approximately -69.0 $W \bullet m^{-2}$ (-12.9%) around noon. Similar to DKSAT and DWSAT, the decrease in BEXP leads to a drier soil surface.

SMCMAX in Noah-MP, which represents soil porosity, was found to be informative and was identified as a critical parameter for most fluxes, especially HFX. In Noah-MP, SMCMAX plays an important role in ground water evaporation, soil thermal conductivity and diffusivity. SMCMAX commonly appears as the denominator in the degree of saturation (S) as in Equation 3.5, which refers to the actual amount of soil water compared to the maximum amount of water that the soil can hold:

$$S = \frac{V_w}{V \cdot SMCMAX} \cdot 100\%, (3.5)$$

where V_w is the volume of water in the soil and V is the total volume of the soil. And the product of SMCMAX and V is the volume of voids (V_v). Generally, if V and V_w remain constant, a larger SMCMAX (larger V_v) corresponds to a a smaller S, which leads to a decrease in LH as a larger SMCMAX indicates a finer soil particles, which may lead to less evaporation at the same soil water content (Hillel 2013).

SMCMAX, SMCREF, and SMCWLT are primarily associated with soil moisture evaporation and vegetation transpiration. The optimized values of SMCMAX and SMCWLT show minimal change (+0.015 $m^3 \bullet m^{-3}$ (+1.51%) and +0.009 $m^3 \bullet m^{-3}$(+6.67%), respectively), while SMCREF decreases by 0.087 m3m-3. The modification of SMCREF impacts transpiration by increasing the β factor in the Noah-type soil moisture factor as in Equation 3.6, which controls stomatal resistance and, consequently, photosynthesis strength:

$$\beta = \sum_{i=1}^{N_{root}} \frac{\Delta z_i}{z_{root}} min\left(1.0, \frac{smois_i - SMCWLT}{SMCREF - SMCWLT}\right), (3.6)$$

where N_{root} and z_{root} are total number of soil layers containing roots and total depth of root zone, Δz_i and $smois_i$ is the thickness and the water content of the ith soil layer. If keeping other 6 parameters except SMCREF at the default value, the reduction in SMCREF results in an average increase of 7.4 $W \bullet m^{-2}$ (+6.5%) in transpiration simulation at noon. This effect becomes more pronounced as soil moisture approaches SMCREF, with around noon transpiration simulations increasing up to 25 $W \bullet m^{-2}$ (+13.8%) on the 9th and 10th of April, the last two days of the study period. It is noteworthy to mention that this reduction in ground evaporation does not necessarily signify weaker transpiration, as the alfalfa plant's root system length may still be able to facilitate sufficient water uptake to meet its water demands. In the model, transpiration rates can be stimulated by higher soil temperatures, with a 2.64K (+0.91%) increase in the top three soil levels (which aligns with the root length of the crop in Noah-MP) resulting in about 36.1% increase in transpiration.

One of the limitations of our optimization process is that it does not consider the dependence between two parameters. In our case, SMCMAX, SMCREF, and SMCWLT are known to be related to each other for a specific soil type, but were assumed to be independent in the prior covariance matrix. SMCMAX, SMCREF, and SMCWLT are largely influenced by soil texture: Clay-dominated soils typically exhibit elevated porosity, field capacity, and wilting point as a consequence of their fine-textured, small pore structure. Conversely, sandy soils possess lower values for these parameters, attributable to their coarser texture and larger pore spaces. Soils with a silt composition demonstrate intermediate characteristics, displaying moderate levels of porosity, field capacity, and wilting point. Our optimization results indicate that the top layer soil exhibits characteristics more closely resembling the loam or sandy loam class rather than the silty clay loam class in Noah-MP - it contains a higher proportion of quartz, resulting in stronger thermal and hydraulic conductivity. On the other hand, the deeper soil may possess more attributes typical of clay soils. The soil parameter values in Noah-MP are based on empirical data, assigning fixed numbers to each soil type. However, in practice, soil parameter values can vary within a range. For instance, SMCWLT specified in the Noah-MP vegetation table (MPTABLE.TBL) for silty clay loam is 0.12 $m^3 \bullet m^{-3}$. However, empirical data indicates that SMCWLT for silty clay loam can be approximately 0.2 $m^3 \bullet m^{-3}$, as observed by Hunt et al. (2009) at the Mead site in eastern Oklahoma. Ghanbarian-Alavijeh and Millán (2009) suggested the range of SMCWLT of silty clay loam is 0.116 – 0.224 $m^3 \bullet m^{-3}$ with the databases from Fooladmand (2007) and 0.154 – 0.329 $m^3 \bullet m^{-3}$ with the databases from Puckett et al. (1985).

3.4.2.3 Model simulation improvements with optimized parameters

3.4.2.3.1 Improved agreement in 2-10 April, 2016

The global optimization of the seven soil parameters leads to a more accurate simulation of HFX, LH, T2, Q2, WS, SMOIS, and TSLB. As shown in Fig 3.4, the simulations from WRF/Noah-MP were improved using the optimized parameters: the daytime HFX was greatly underestimated by more than 100 $W \bullet m^{-2}$ with original parameter values, but the optimal parameters drive simulations that agree better with flux tower observations (Fig 3.4(a)). The histogram from Fig 3.4(b) shows that the mean of the HFX simulation mismatches is approximately 0 W/m^2, and the reduction in the standard deviation with the optimized parameters suggests a more accurate simulation of HFX across both daytime and nighttime periods. The LH is mostly improved from overestimation and the Q2 is also attributed to smaller diurnal variations corresponding to the change in LH. The better agreement of T2 and WS simulations with data is not as evident as the other 3 variables, but the improvement can still be seen, especially every day around noon. However, the simulated top layer soil moisture with the optimized parameters appears drier compared to the observed data. This difference can be attributed to the assumption of uniform soil moisture across the 20 cm soil layer, which is used in calculating surface energy fluxes. The observed soil moisture at a nearby site, located 192 m away, indicates that soil moisture at 5 cm below the ground surface is approximately 0.08 $m^3 \bullet m^{-3}$ drier than at 10 cm. Consequently, it is plausible to infer that the surface layer soil moisture at the SGP site should also be drier than at 10 cm depth. The increase in HFX and the decrease in LH, observed with the optimized parameters, align with the drier top layer soil moisture conditions in the Noah-MP model. TSLB exhibits less mismatched, likely due to the use of surface skin temperature, instead of the top layer soil temperature, in calculating HFX and LH. This involves the computation of saturated vapor pressure and the temperature difference between the ground surface and the air above.

3.4.2.3.2 Improved agreement in the entire 2016 alfalfa growing season at SGP site

The optimization results also improved simulations of HFX, LH, T2, Q2, WS, and TSLB over a longer time period during the 2016 alfalfa growing season at SGP site – specifically in April and May. By utilizing the seven optimized parameters, improvements are observed in the simulations of LH, T2, Q2, and WS, as presented in Fig 3.5(c)-(j), whereas HFX is generally overestimated, as shown in Fig 3.5(a) and (b).

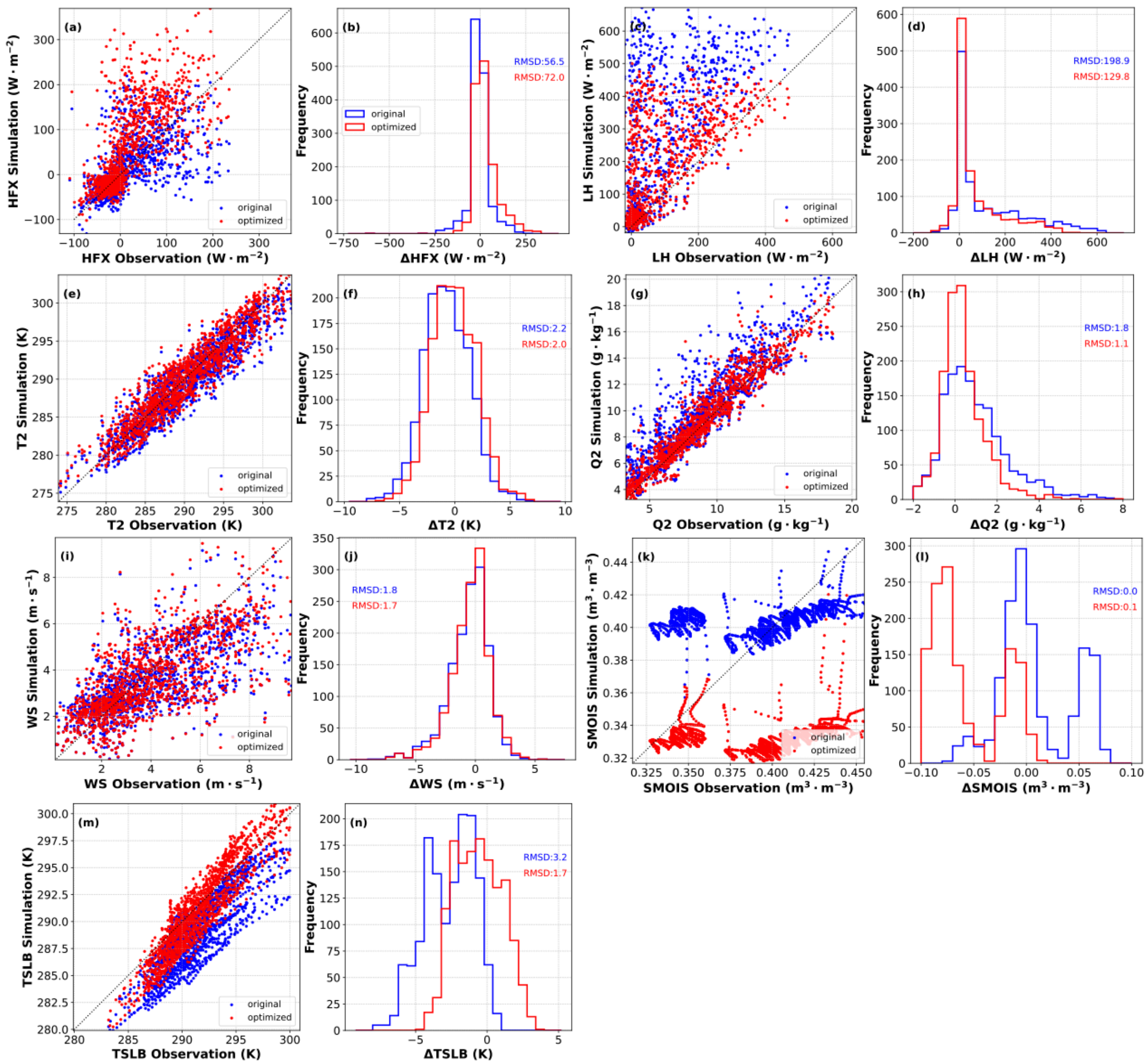

Figure 3.5 (a) HFX simulated by WRF/Noah-MP with original values of the six parameters (blue line) and the optimized parameters (red line) compared to the observations at the SGP site (black triangle) from April 1st to May 30th. The gray shades represent nighttime (8 PM – 8 AM). Similar for (c), (e), (g), (i), (k), and (m) but for LH, T2, Q2, WS, SMOIS, and TSLB. (b) The blue histogram is for the simulated HFX with original values of the six parameters minus the observation at the SGP site, red histogram is for the simulated HFX with the optimized parameters minus the observation at the SGP site. Similar for (d), (f), (h), (j), (l), and (n) but for LH, T2, Q2, WS, SMOIS, ad TSLB correspondingly.

The optimization of the seven parameters also has notably enhanced the simulation of TSLB, which is a crucial variable in numerous agricultural and hydrological applications. The optimized parameters have effectively improved the representation of the heat exchange between the soil and the atmosphere, which is vital for the accurate simulation of the energy balance at the land surface. However, SMOIS tends to be consistently underestimated. This could potentially be attributed to the sharp gradient present in the top 20cm of the soil stratum. These findings authenticate the efficacy of the optimization process in enhancing the overall performance of the Noah-MP model, rendering it a more dependable tool for investigating land-atmosphere interactions and their environmental consequences.

The changes in surface energy flux attributable to global optimization are predominantly associated with surface layer soil moisture for both the nine-day and the long-term simulations. The correlation coefficient, calculated between the daily minimum of the reduction in LH (determined by subtracting LH with the original parameters from LH with the optimized parameter), and the daily mean of optimized top-level soil moisture, is found to be 0.85. Furthermore, there exists a negative correlation of -0.83 between the daily maximum increase in HFX (calculated by subtracting HFX with the original parameters from HFX with the optimized parameter) and the daily mean of optimized SMOIS. These relationships highlight the intricate interactions between soil moisture and energy fluxes in the context of global optimization processes.

Decreased soil moisture is typically associated with increased HFX, which subsequently promotes the development of the Convective Boundary Layer (CBL) within the coupled land-atmosphere system (Pal and Haeffelin 2015; Xu et al. 2021). PBLH was computed from 6-hourly radiosonde air temperature profiles and WRF/Noah-MP simulations with both original and optimized parameters, utilizing the Bulk Richardson Number method (threshold 0.25). In accordance with previous studies, the diminished surface-level soil moisture and augmented daytime HFX associated with optimized parameters are correlated with an elevated CBL as shown in Fig 3.6(a). As depicted in Fig 3.6(b) and (c), the Bulk Richardson Numbers derived from the radiosonde are generally larger than those from the WRF simulation. However, parameter optimization increases the simulated Bulk Richardson Numbers, thereby bringing the simulation closer to the observations. The soil parameter optimization results in a reduction of the RMSD between the radiosonde and WRF-simulated vertical air temperature inferred PBLH during daytime (8 AM to 8 PM) from 576.2m to 475.3m, which indicates a more accurate representation of PBLH in the simulation with optimized parameters, thereby demonstrating the effectiveness of the soil parameter optimization in improving the simulation of land-atmosphere interactions.

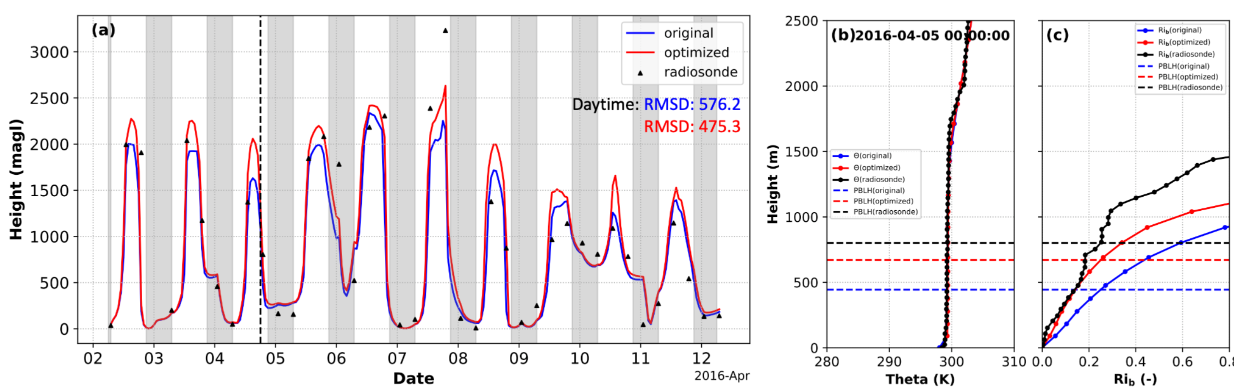

Figure 3.6 (a) The calculated PBLH using the Bulk Richardson Number method with a threshold of 0.25, based on measurements from radiosonde (black triangle scatters), simulations with original parameters from WRF/Noah-MP (blue solid line), and simulations with optimized parameters from WRF/Noah-MP (red solid line). The black dashed line indicates the time in (b) and (c). Panel (b) shows the vertical profile of potential temperature ($\boldsymbol{\theta}$), with the same color pattern as (a). The horizontal dashed lines in (b) represent the PBLH calculated using the Bulk Richardson Number method with a threshold of 0.25. Panel (c) is similar to (b) but displays the vertical profile of Bulk Richardson Number ($\boldsymbol{Ri_b}$).

3.5 Discussion

Changes in soil parameters have profound implications for soil hydrology, which in turn modulates both soil temperature and moisture profiles. For instance, changes in parameters such as SMCMAX or DKSAT can influence the soil's water-holding capacity and the rate at which water moves through the soil profile, respectively. An enhanced SMCMAX, for example, can augment the simulated soil's retention of water, leading to prolonged soil moisture persistence. This increased moisture content has the dual effect of modulating the soil's thermal properties — damp soils generally have a higher thermal capacity than dry. Consequently, with enhanced moisture retention, soils exhibit a slower thermal response to diurnal temperature fluctuations. In the context of the surface energy balance, these modifications in soil temperature and moisture can significantly impact the partitioning between HFX and LH. A more moisture-laden soil, resultant from altered hydrological parameters, tends to favor higher rates of evapotranspiration, subsequently amplifying the LH at the expense of the HFX. This shift not only affects near-surface atmospheric conditions but also plays a significant role in underpinning local and regional weather and climate patterns.

Based on the soil parameter table in Noah-MP with USGS soil classification, the optimized parameter values are more in line with soil composed of a greater proportion of sand relative to the typical silty clay loam. For example, DKSAT is found to be $9.10\times 10^{-6}\ m\ s^{-1}$ compared to the default DKSAT of silty clay loam ($2.08 \times 10^{-6}\ m\ s^{-1}$). The soil parameter table in Noah-MP (SOILPARM.TBL) reveals that DKSAT for sand significantly exceeds that of silt and clay. Specifically, the DKSAT may vary over several orders of magnitude between catchments – value for sand is measured at $46.6 \times 10^{-6}\ m\ s^{-1}$, while silt measures at $3.38 \times 10^{-6}\ m\ s^{-1}$ and clay at $0.974 \times 10^{-6}\ m\ s^{-1}$. This underpins a fundamental physical principle: the diffusion of water in soil is intrinsically governed by its class, with substantial sensitivity to the proportion of constituent soil components.

Uncertainty in soil classification translates to variability in these properties, subsequently influencing the partitioning between HFX and LH. For instance, misclassification that overlooks a soil's true water retention capability might lead to inaccurate estimations of surface evaporation rates. Similarly, an imprecise understanding of the soil's thermal inertia can yield discrepancies in diurnal temperature amplitudes and phase lags. Such uncertainties not only modulate the local radiative balance but also have far-reaching consequences on boundary layer dynamics.

In both the Noah-MP model and observational data from the SGP site, the soil is classified as silty clay loam, exhibiting uniformity in composition throughout the soil profile depth. However, from the data at nearby Mesonet (Afchar et al. 2018) sites, the soil classification can vary with depth. For example, the soil characteristics at a Mesonet site in Blackwell (BLAC), which is to the northeast of SGP site and about 27 km away, suggest that the soil texture at 5 cm under the ground is loam (27.8% sand, 49.2% silt, and 23% clay). However, the soil at 25 cm depth is recognized as silty clay loam (17.5% sand, 44.8% silt, and 37.8% clay) and clay loam at 60 cm depth (20% sand, 40.3% silt, and 39.7% clay. Based on soil texture records from nearby sites and the limited drainage observed in the deeper soil layers, we infer that the soil texture beneath the top layer closely resembles clay. It is common for soil characteristics to vary with depth, as different layers of soil may have different physical and chemical properties due to factors such as the type of parent material, the amount of organic matter, and the amount of weathering. The varying proportions of sand, silt, and clay in a soil can lead to differing infiltration rates, which can affect the way energy is partitioned at the surface.

Cropland soil management practices considerably impact soil properties, including soil structure, organic matter content, and overall soil health. These alterations subsequently affect the soil's water retention capacity and plant-available water. For instance, conservation tillage aids in preserving the soil's natural structure and minimizes soil compaction, which consequently maintains or enhances soil porosity. Furthermore, conservation tillage contributes to improved soil structure, augmented organic matter content, and enhanced water-holding capacity. These factors can indirectly influence the wilting point by fostering better soil structure and promoting increased organic matter content. As plants develop, their root systems infiltrate the soil, forming channels and cavities while traversing the soil matrix. These root-induced channels contribute to soil porosity by augmenting the quantity and dimensions of pore spaces. Moreover, the decomposition of expired roots results in residual channels that can further bolster soil porosity.

BO is an effective method for optimizing functions where the analytical form is unknown or complex, often resulting in reduced computational costs. In our application of BO to soil properties, we operate under the assumption that parameters such as SMCMAX (soil porosity) and SMCWLT (wilting point) are independent. This is a simplification, as these parameters typically exhibit physical interdependence; for example, soils with a higher porosity generally also have a higher wilting point due to their capacity to retain more water. While BO can handle multiple dimensions, it performs best with fewer than 20 dimensions, with less than 10 being ideal. To manage the independence assumption and dimensional constraints, we gave a reasonable range for each parameter based on original Noah-MP soil parameter table and proceed with the optimization, note that this approach may not capture the full complexity of soil parameter interactions.

In considering longer-term simulations, computational expenses become a paramount concern. Our current approach, employing BO, has demonstrated efficiency for a single-site, short-term, nine-day simulations, with 370 iterations necessitating approximately 13 hours of computational time. Extrapolating this to higher dimensions implies that the computational cost would grow prohibitively high. Given the nonlinear increase in complexity as parameter amount increases, BO may not be the optimal method for parameter optimization in high-dimension studies. Building on this study, future research should investigate optimization strategies that can accommodate the expanded parameter dimensions efficiently. Discovering a method that minimizes computational requirements is crucial for the practicality of optimizing models over more extended periods.

3.6 Conclusions

The default parameter set in WRF/Noah-MP leads to residual biases in simulating surface energy fluxes and near-surface atmospheric state variables that requires further research to understand and address. To better simulate the surface energy fluxes and atmospheric state variables in WRF/Noah-MP, we find the most sensitive seven parameters (BEXP, DKSAT, DWSAT, SMCMAX, SMCREF, SMCWLT, QUARTZ) in the chosen parameterization options in Noah-MP with a finite difference sensitivity analysis and use a surrogate BO method to optimize these seven parameters based on nine-day observations from 2-10 April, 2016 at SGP site. The optimization results tend to suggest the soil texture at SGP site contains more sand than the silty-clay-loam in the Noah-MP soil classification, resulting in the properties involved in these seven parameters contain more characteristics from sand. The general changes in these seven parameters enhance the downward soil water infiltration and reduce the amount of available energy. The parameters optimization helps reduce the mismatches between WRF/Noah-MP and the eddy covariance tower observations at SGP site in simulating HFX, LH, T2, Q2, WS, SMOIS, and TSLB from 2-10 April. With the optimized parameters, the simulations of HFX, LH, T2, Q2, WS, SMOIS, and TSLB in the SGP site alfalfa spring growing season also get improved. By optimizing the parameters of the WRF/Noah-MP using BO, we not only enhance the simulation of key variables such as HFX and LH but also improve the representation of atmospheric state variables like specific humidity. These findings demonstrate the potential of parameter optimization techniques to bridge the gap between observational and model dimensions, ultimately advancing our understanding and prediction of land-atmosphere interactions. Such improvements have broader implications for weather forecasting, climate modeling, and land management strategies.

Chapter 4 Characterizing Methane (CH_4) Enhancements at the SGP ARM Site: Meteorological Influences and Source Attribution

4.1 Introduction

Methane (CH_4) plays a pivotal role in global warming and is the second most significant greenhouse gas contributor to climate change in terms of radiative forcing (Myhre et al. 2014; Stocker et al. 2013). Despite its critical importance, the complexity of the linkage between specific CH_4 emission sources and their atmospheric concentration variations remains less understood (Turner et al. 2019). Understanding CH_4 emissions at local and regional scales is crucial because they provide the foundation for improving our knowledge of the role of CH_4 in global climate systems, which are essential for predicting the global climate impact from CH_4 (Bridgham et al. 2013; Stavert et al. 2022). Furthermore, examining how CH_4 emissions interact with meteorological conditions can improve our ability to simulate regional and global CH_4 transport and distribution, leading to more accurate assessments of its role in climate dynamics and supporting more effective climate policies.

Local and regional CH_4 concentrations are influenced by a combination of emissions and meteorological conditions (Patra et al., 2009). For instance, meteorology alone can alter near-surface CH_4 concentrations—shallow PBL associated with increased atmospheric stability often lead to elevated CH_4 concentrations (Esau and Zilitinkevich 2010). Emissions also play a crucial role in regional CH_4 variability, as numerous studies have demonstrated that CH_4 plumes from emission sources significantly contribute to regional CH_4 increases (Cusworth et al. 2021a; Duren et al. 2019; Kort et al. 2014; Yuan et al. 2015). Moreover, the interplay between meteorological conditions and emissions is critical in altering the distribution and variability of CH_4. For example, natural CH_4 sources, such as wetlands, are particularly sensitive to environmental changes in temperature, radiation, and precipitation (Bousquet et al. 2011; Dlugokencky et al. 2009; Pison et al. 2013). Despite these advances, significant uncertainties remain in accurately attributing CH_4 concentration variations to specific emission sources and meteorological conditions due to the complex interplay between these factors (Balashov et al. 2020; Bloom et al. 2017).

Previous studies have consistently found elevated CH_4 concentrations at the Southern Great Plains (SGP) Atmospheric Radiation Measurement (ARM) site (Miller et al. 2013; Saito et al. 2013; Turner et al. 2016) (refer to the SGP site simply as SGP hereafter), but the exact mechanisms driving these high concentrations remain unclear. For example, Saito et al. (2013) used chemistry transport models incorporating both natural and anthropogenic CH_4 inventories but found that the emissions in these inventories were too low to explain the observed CH_4 levels, particularly within the lower 1.5 km of the atmosphere. Meanwhile, recent studies highlight that grasslands act as significant CH_4 sinks due to methanotrophic activity in soils (Koyama et al. 2024). Given this established role of grasslands as CH_4 sinks, the persistently high CH_4 concentrations at the SGP site present a paradox, suggesting that the observed CH_4 levels may not be fully explained by known sources or mechanisms. This calls into question whether unaccounted-for local emissions, underestimated anthropogenic contributions, or other regional factors are driving the elevated CH_4 concentrations, underscoring the need for further investigation.

One of the key uncertainties is the role of meteorological conditions in driving these high local CH_4 concentrations. The frequent occurrence of a stable nocturnal PBL in the U.S. Great plains (Banta et al. 2007) is likely a significant factor contributing to elevated CH_4. A stable PBL, especially at night, can trap CH_4 near the surface, resulting in elevated concentrations (Patra et al. 2009). The shallowest, stably-stratified PBLs are of particular concern, as these conditions are highly sensitive to perturbations in the Earth's surface energy balance and GHG emission rates (Esau and Zilitinkevich 2010). However, these strongly stratified PBLs have been underexplored (Holtslag et al. 2013). Correct representation of the stable boundary layer is difficult owing to the weak behavior of turbulence (Mauritsen and Svensson 2007), which highlights the difficulty in our understanding of how these conditions affect GHG accumulation.

In addition to the stable PBL, low-level jets (LLJs) represent another meteorological condition that can significantly influence CH_4 dynamics in the U.S. Great Plains. LLJs in this region frequently develop at night due to a combination of factors, like inertial oscillation caused by the decoupling of nocturnal winds from surface friction following the formation of a near-surface temperature inversion (Blackadar 1957; Song et al. 2005), as well as topographical influences from the Rocky Mountains (Bleeker and Andre 1951; Bonner and Paegle 1970; Pan et al. 2004; Uccellini 1980). With LLJs occurring in the U.S. Great Plains more than 20% of the time and often accompanied by strong temperature inversions and pronounced stratification below the jet core (Luiz and Fiedler 2024), LLJs can be a critical factor in the horizontal and vertical dispersion of gases. Previous studies have shown that LLJs play a significant role in the transport of gases like ozone (Hu et al. 2013; Klein et al. 2014), but their specific effects on CH_4 dispersion and accumulation remain unexplored.

In addition to the meteorological uncertainties, emission attribution challenges further complicate the understanding of CH_4 dynamics at SGP. Oklahoma is known for substantial anthropogenic CH_4 emissions from oil and gas production and agriculture, particularly livestock farming (Katzenstein et al. 2003; Omara et al. 2018). However, existing emission inventories like U.S. Environmental Protection Agency (EPA) CH_4 inventory are found to underestimate CH_4

emissions especially in the south central U.S. (Miller et al. 2013; Saito et al. 2013; Turner et al. 2015). Turner et al. (2015) suggested that this underestimation could be attributed to oil/gas and livestock emissions, but a clear quantitative separation between the two sources is difficult due to their spatial overlap. This overlap complicates source attribution and hinders the ability to accurately identify and quantify individual contributions to regional CH_4 concentrations. As a result, high-resolution information, such as field measurements and investigations, is crucial to refine our understanding of these emissions.

To address the uncertainties in both meteorological and emission attribution to the high CH_4 at SGP, this study aims to explore three critical research questions that will provide a more comprehensive understanding of local CH_4 dynamics at SGP:

1. **Temporal Analysis of CH_4 Peaks:** What are the specific times of day and seasons when CH_4 concentration reach their peak at SGP?
2. **Meteorological Correlations:** What meteorological conditions correlate with these peaks in CH_4 concentration?
3. **Unaccounted Emission Sources:** Are there significant sources of CH_4 emissions near SGP that are not currently included in standard emission inventories?

This research employs a robust integrative approach, combining in-situ CH_4 concentration measurements with comprehensive meteorological data analysis and a field campaign to identify and quantify the potential CH_4 emission sources. By doing so, we aim to refine our understanding of the complex interactions that drive CH_4 variability at SGP. The outcomes of this study are expected to contribute to the enhancement of regional CH_4 emission inventories and to provide insights that could guide effective climate mitigation strategies in CH_4-intensive regions.

4.2 Study Sites and Data

4.2.1 Study Sites

All measurements were taken at or near the U.S. Department of Energy (DOE) ARM SGP Central Facility (Mather and Voyles 2013; Sisterson et al. 2016) near Lamont, Oklahoma shown in Fig 4.1, which is located at 36.605° N, 97.488° W, and the terrain elevation is 314 m above mean sea level. The landscape is relatively flat with a local terrain slope less than three degrees.

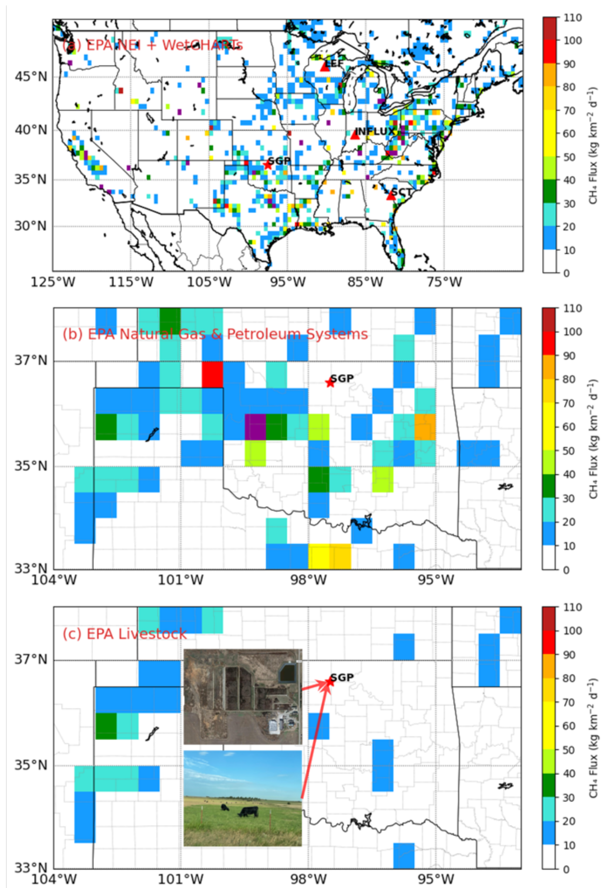

Figure 4.1(a) CH_4 emissions across the U.S. in 2018, combining the Environmental Protection Agency (EPA) Greenhouse Gas Inventory (GHGI) at a 0.1° × 0.1° resolution and Wetland emissions from WetCHARTs at a 0.5° × 0.5° resolution. To merge these datasets, the GHGI data was upscaled to match the 0.5° × 0.5° resolution of WetCHARTs before summing GHGI and WetCHARTs. (b) CH_4 emissions from natural gas and petroleum systems based on EPA GHGI, including specific classifications in GHGI: abandoned, surface, and underground coal, petroleum systems exploration, production, and transport, abandoned oil gas, natural gas distribution

exploration, processing, production, and transmission storage. (c) CH_4 emissions from livestock sources as classified by the EPA GHGI, including enteric fermentation and manure management.

SGP contains an extensive suite of instrumentations for monitoring the atmosphere and surface properties. Most of these instruments operate continuously, and the data are available from the ARM website (https://adc.arm.gov/discover, McCord and Voyles (2016)). SGP contains several heavily instrumented subsites or "facilities" that are geographically dispersed over Oklahoma and Kansas (Mather and Voyles 2013). For this study, we use observations from the central facility (C1), which also contains the largest number and most diverse suite of instruments.

A field campaign was conducted to investigate and quantify the potential CH_4 emissions near SGP by measuring CH_4 concentrations in the near-surface atmosphere. The field campaign route is around the SGP site (N3100 Road, E0280 Road, N3090 Road, and County Line Road) to investigate the activity of open-range cattle. We also investigated an AFO, about 5.8 km to the northwest of SGP at 36.64° N, 97.535° W, driving on N3070 Road, E0240 Road, N3060 Road, E0250 Road, and E0260 Road.

Other sites in this study for comparison with SGP includes the Wisconsin forest site (LEF) in Park Falls, WI, the South Carolina Tower (SCT) site near Beech Island, SC, and the Indianapolis Flux Experiment (INFLUX) site. CH_4 datasets at LEF, SCT, and INFLUX is provided from Kenneth N. Schuldt (2023). The locations and other general information of these sites is given in Table 4.1.

Table 4.1 Sites general information.

Site Code	Location	Latitude, Longitude	Elevation (masl)	Measurement Height (m)	Potential main CH_4 emission	Reference
SGP	Lamont, OK	36.6070, - 97.489	314	2,4,25*,60	Oil and natural gas system, agriculture	Sisterson et al. (2016)
LEF	Park Falls, WI	45.9451, -90.2732	472.0	30*,122,396	Wetlands	Andrews et al. (2024)
SCT	Beech Island, SC	33.4057, -81.8334	115.2	31*,61,306	Wetlands	Andrews et al. (2024)
INFLUX (Site 1)	Indianapolis, IN	39.5805, -86.4207	182	10*, 40,121	Landfills	Miles et al. (2017)

*CH_4 concentrations at the specific height are used to compare across the sites in Table 4.1

4.2.2 Data

4.2.2.1 CH_4 Data

CH_4 concentration data used in this study were obtained from the Precision Gas System (PGS), which provides high-accuracy and high-precision measurements of CH_4 at various heights (2m, 4m, 25m, and 60m) above the ground. The system samples air every 20 minutes, with measurements averaged over 30 seconds at each level. For the purpose of our analysis, we computed hourly averages of these CH_4 concentration measurements. Additional details regarding the PGS can be found in Torn (2005).

To compare CH_4 concentrations at the SGP site with other tower sites across the U.S., we focused on data collected from January 1, 2017, to December 31, 2020, when measurements were consistently available across all four sites. We used CH_4 measurements at 25 meters from SGP and compared them to the lowest measurement heights at the other sites: 30 meters at LEF, 31 meters at SCT, and 10 meters at INFLUX, as detailed in Table 4.1. CH_4 data for LEF, SCT, and INFLUX were sourced from the Observation Package (ObsPack) insitu CH_4 products (Masarie et al. 2014) and filtered using quality flags. While the 25-meter CH_4 data at SGP were provided by PGS, as ObsPack did not include this 25m measurement for SGP. To ensure consistency, both hourly mean values and quality flags were applied across all datasets. Furthermore, we applied a linear detrending process to remove the long-term increasing trend in CH_4 by subtracting the linear trend of daily CH_4 concentrations from the hourly-averaged CH_4 values. This process allowed us to focus solely on short-term variations and anomalies in CH_4 concentrations across the different sites during the study period.

In addition to the continuous CH_4 measurements obtained from the Precision Gas System (PGS) and ObsPack, we conducted a field measurement campaign in June 2024 using a LI-COR LI-7810 CH_4/CO_2/H_2O Trace Gas Analyzer (https://www.licor.com/env/products/trace-gas/LI-7810, LI-COR Biosciences, Lincoln, Nebraska, USA). LI-7810 provides high-frequency (1 second) CH_4 concentration data in the area surrounding the ARM site and the AFO. These measurements complement the PGS data by providing a more detailed spatial and temporal analysis of CH_4 concentrations near potential emission sources. The detailed design of the field campaign will be described later in 3.3.

To ensure measurement consistency, we positioned the LI-7810 at the foot of the 60-meter PGS tower from 9 AM to 11 AM on June 26th, comparing its CH_4 readings with those measured at 2 meters by the PGS (Figure 4.2). PGS provides CH_4 concentrations every 20 minutes, thus we have six comparative samples over the two-hour period. The maximum observed difference (LI-7810 CH_4 minus PGS 2m CH_4) was +5.06 ppb, while the average difference for the remaining five samples was +0.39 ppb (with a standard deviation of 0.53 ppb). These results confirm that the CH_4 concentration measured by the LI-7810 are consistent with those from the PGS.

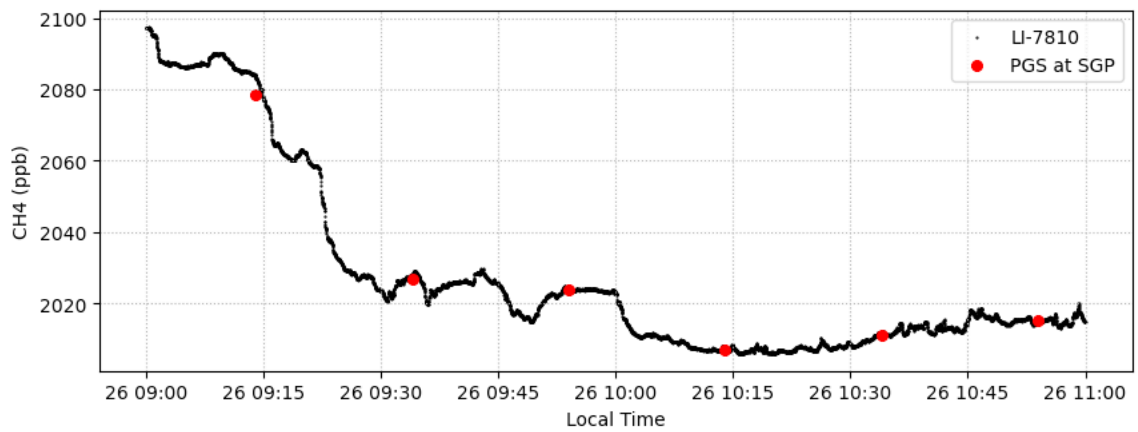

Figure 4.2 CH_4 concentration from LI-7810 (black) and the PGS at SGP (red) from 9 to 11AM, June 26

4.2.2.2 Meteorological Data and Model Simulations

To investigate the relationship between surface meteorological conditions and CH_4 concentrations, we utilized multiple meteorological data sources: 1. surface wind speed and direction from the Surface Meteorological System (MET) at the SGP C1 station (Kyrouac and Tuftedal 2024); 2. vertical meteorological states profile from balloon-borne radiosonde soundings (Keeler et al. 2019); 3. continuous wind speed and direction data above the surface from Doppler lidar (Newsom et al. 2015).

Wind speed and direction at 10 meters were collected every minute from the MET system to represent surface wind conditions at SGP and during the field campaign near the AFO. These wind measurements were also averaged hourly to align with the time resolution of the CH_4 data.

To explore meteorological conditions above surface, we used balloon-borne radiosonde soundings and Doppler lidar measurements. Radiosonde measurements are typically conducted every 6 hours at SGP. They provides vertical profiles of temperature, humidity, wind speed, and wind direction at a high temporal resolution of 2 seconds, offering detailed insights into the atmospheric structure necessary for analyzing the relationship between CH_4 concentrations and meteorological conditions within the nocturnal PBL.

To overcome this temporal gap and capture more continuous atmospheric dynamics, we supplemented the soundings with Doppler lidar measurements, offering real-time data on vertical wind velocity and horizontal wind speed/direction. The Doppler lidar provides height- and time-resolved measurements of horizontal wind speed and direction (facility 2010a) and vertical velocity (facility 2010b) on a 30m vertical spatial resolution and 15min temporal resolution. We also applied a higher SNR threshold (0.01) than was used (0.008) in the original processing. The minimum height of the lidar-derived vertical velocity statistics is approximately 100 m. More details about the instrument are provided by Newsom and Krishnamurthy (2022). Details about the vertical velocity statistics value-added product (VAP) are provided by Newsom et al. (2019), and details about the Doppler lidar wind VAP are given by (Newsom et al. 2015).

4.3 Methods

4.3.1 Identifying CH_4 Spikes using PGS Data

In our study, we define CH_4 anomalies by first calculating the hourly mean CH_4 concentration for each measurement height (2, 4, 25, and 60 meters) and then minus the climatology baseline. The climatology for each hourly interval is established by averaging the CH_4 concentration over the same hourly period for the entire month in the same year at the same measurement height – the CH_4 anomaly at a given hour is determined by subtracting this monthly mean from the observed hourly mean CH_4 concentration. For example, the CH_4 anomaly at 25m at 8 AM on January 1st, 2020, is calculated by taking the hourly mean CH_4 concentration at 25m from 8:00 to 8:59 AM on that date and subtracting the average CH_4 concentration at 25m of all corresponding 8:00 to 8:59 AM intervals in January 2020. This approach allows us to effectively isolate specific anomalies by removing the background seasonal variability and the long-term trend and identifying significant deviations from the expected CH_4 levels.

4.3.2 Quantifying PBL Stability and Determining PBL Height Using Radiosonde Data

To further explore these CH_4 anomalies and their relationship with the PBL stability, we employed radiosonde data to calculate the Richardson number (Ri) and determine PBLH.

The Gradient Richardson Number (Ri) is a key metric used to quantify turbulence in the PBL. It is defined as the ratio of mechanical turbulence production to thermal production or destruction of turbulent kinetic energy (Equation 4.1):

$$Ri = \frac{\frac{g}{T_v}\frac{\partial \theta_v}{\partial z}}{\left(\frac{\partial U}{\partial z}\right)^2 + \left(\frac{\partial V}{\partial z}\right)^2}, (4.1)$$

where g is the gravitational acceleration, T_v is the virtual temperature, θ_v is the virtual potential temperature, z is the height above ground level, and U, V are the wind components toward the east and north. A Ri exceeds a critical threshold (i.e., critical Richardson number Ri_c, typically between 0.25 and 1 (Galperin et al. 2007) characterizes the change of turbulent energy to laminar flow.

To prevent overestimating atmospheric stability, we set a minimum threshold in calculating Richardson number to avoid excessively high Ri values in cases of minimal wind shear. Doppler lidar precision limitations often result in wind speed errors on the order of 0.01 m/s in the VAP, while radiosonde wind speed measurements are accurate to the order of 0.1 m/s. These instrument errors can lead to subtle changes in wind speed and direction that do not accurately reflect true variations, potentially causing near-zero wind shear values in stability calculations, thus leading to an unrealistically high Ri. To remedy this, we've introduced a minimum threshold in the calculation of the denominator: $\left(\frac{\partial U}{\partial z}\right)^2 + \left(\frac{\partial V}{\partial z}\right)^2 \geq 10^{-2}$. The choice of 10^{-2} helps prevent overestimation of atmospheric stability by avoiding excessively high Ri values. We calculate Ri using its discrete approximation from balloon sounding data, providing a metric that compares the buoyant production to the shear production of turbulence and quantify the PBL stratification.

Ri is also often used to determine the PBLH, which method is called the critical Richardson number method. However, in this study, we determine the PBLH using the nose of LLJ instead of the critical Because it is less effective in highly stable conditions: in a very stable PBL, turbulence becomes intermittent, non-Kolmogorov, and non-stationary, driven by small-scale processes that do not conform to the traditional assumptions of similarity theory (Grachev et al. 2013), making Ri less reliable. In such cases, the LLJ nose is a better indicator of PBLH. The LLJ, a fast-moving wind layer often present at night, generates shear-induced turbulence even in stable conditions, providing a more accurate representation of the turbulent processes within the PBL. We define the PBLH as the height of the nose of the LLJ from the radiosonde wind profile, limiting our search to heights below 1000 meters. If multiple noses are present, we select the lowest one to define the PBLH. Furthermore, we define the wind speed at the nose of the LLJ as the LLJ strength. This approach ensures that the most relevant turbulence features are captured, even in highly stable nocturnal boundary layers where traditional methods may fail.

This method of using the LLJ nose to define the PBLH is particularly useful in regions like the Southern Great Plains, where LLJs are common (Berg et al. 2015; Ferguson 2022; Song et al. 2005). Studies like Klein et al. (2014); Moreira et al. (2015); North et al. (2014); Zhang et al. (2014) have demonstrated the importance of the LLJ in promoting vertical mixing and redistributing atmospheric constituents, such as ozone and CH_4, from the LLJ nose to the surface.

Because balloon-borne soundings are not available at the three other sites (LEF, SCT, INFLUX), we used model simulations from the Weather Research and Forecasting (WRF) model to estimate PBL stability at each location using the same configuration as in Hu et al. (2020). We extracted the U and V components of wind speed and potential temperature at different levels within the lowest 300 meters above ground at the grid cell corresponding to each site. Using these variables, we calculated the Richardson number (Ri) to evaluate the atmospheric stability. This analysis concentrated on the winter months (DJF) and nighttime to early morning hours (9 PM to 6 AM) from 2017 to 2020. By focusing on these time periods, we aimed to capture the influence of stable boundary layer conditions, which typically dominate during winter nights and can significantly impact CH_4 concentrations near the surface.

By combining the use of Ri for assessing turbulence and the LLJ nose for defining PBLH, we are able to gain a comprehensive understanding of boundary layer stability at SGP. This integrated approach is crucial for accurately interpreting the surface CH_4 anomalies and their potential link to PBL dynamics and meteorological conditions.

4.3.3 Field Measurement Campaign and Top-Down CH_4 Emission Estimation Using the Mass Balance Method

To detect and quantify the potential CH_4 emissions near the ARM site, we conducted a field measurement campaign using LI-7810 (as introduced in 4.2.2.1) from June 23 – 26, 2024. The LI-7810 was mounted at the driver's window of a pickup truck, which allowed us to measure CH_4 concentrations along the red route shown in Fig 4.3. These measurements were conducted in the early mornings (4:30 AM to 9 AM local time) at a rate of one sample per second (1 Hz). To minimize noise or bias from pressure changes, we maintained a driving speed of less than 5 mph.

The primary goal was to capture CH_4 enhancements surrounding the SGP central facility, identify potential CH_4 emission sources, and estimate their emission rates using a top-down mass balance method.

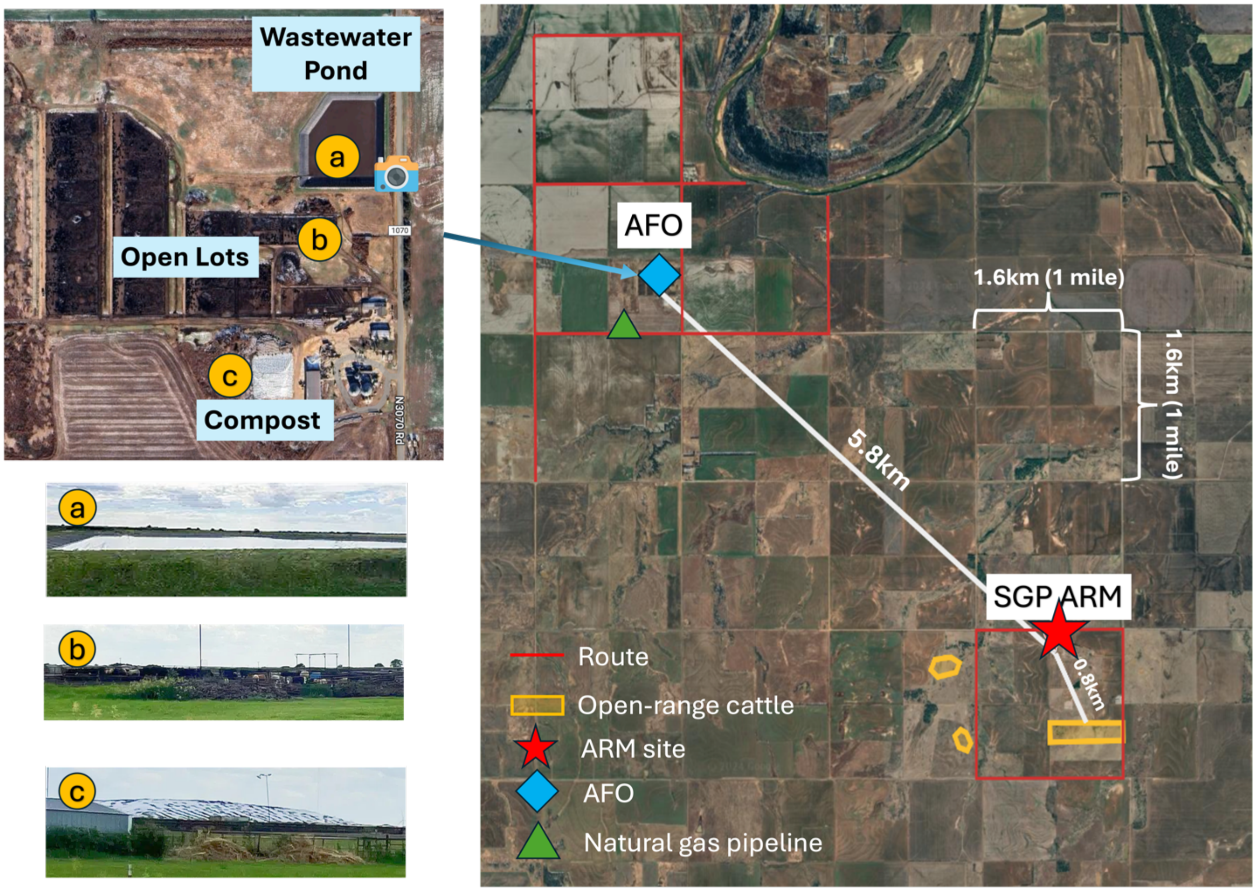

Figure 4.3 Map showing the field measurement campaign routes marked with red lines. Yellow-shaded areas indicate potential locations of open-range cattle, as observed from satellite imagery retrieved from Google Maps satellite layer. The SGP ARM site is marked by a red star and the animal feeding operation (AFO) facilities are marked by blue diamonds. The green triangles represent the locations of underground natural gas pipelines. The AFO facility includes (a) a wastewater pond, (b) open cattle lots, and (c) a compost area. The three photos at the bottom left depict the (a) wastewater pond, (b) cattle lots, and (c) compost, all taken from the location indicated by the camera icon in the top-left image.

We applied the mass balance method to estimate CH_4 emissions from the field campaign data. This approach calculates emission rates by integrating the difference between CH_4 concentrations measured upwind (background) and downwind (enhanced) across the width of the plume (2b) and from the ground (z_{ground}) up to the top of the PBL (PBLH) (Karion et al. 2015; Lavoie et al. 2015; Pandey et al. 2019; Peischl et al. 2015). The emission flux (F_{CH_4}) is determined using the formula (Equation 4.2):

$$F_{CH_4} = v \int_{-b}^{b} \Delta[CH_4] \left(\int_{z_{ground}}^{\mathrm{PBLH}} n_{air}\, dz\right) \cos\alpha\, dx, \quad (4.2)$$

where n_{air} is the molar dry air density, estimated using the ideal gas law with near-surface pressure and temperature from balloon-borne soundings. $\Delta[CH_4]$ is the CH_4 enhancement (downwind CH_4 minus upwind CH_4). v is the wind speed. $V\cos\alpha$ is the wind speed component normal to the driving direction. The 2b value is defined as the length of the measurement path where CH_4 concentrations remain continuously elevated, with a peak directly downwind of the source, resembling a normal distribution. We assume that wind direction and speed remain constant throughout the measurement period.

In this top-down approach, we focused on inferring emission rates based on observed downwind and upwind CH_4 concentrations in the atmosphere, rather than applying emission factors on total emission volume like bottom-up methods (e.g. EPA CH_4 inventory). This method is advantageous for identifying unreported or underestimated emissions in the region.

4.4 Results

4.4.1 CH_4 Concentration Trends at SGP Compared to Other Locations (2017-2020)

SGP is a focus of this study because CH_4 at this site is consistently higher compared to other sites in Table 4.1 across the United States over the 2017-2020 period. As shown in Figure 4.4, several key characteristics distinguish the CH_4 trends at SGP during this time period:

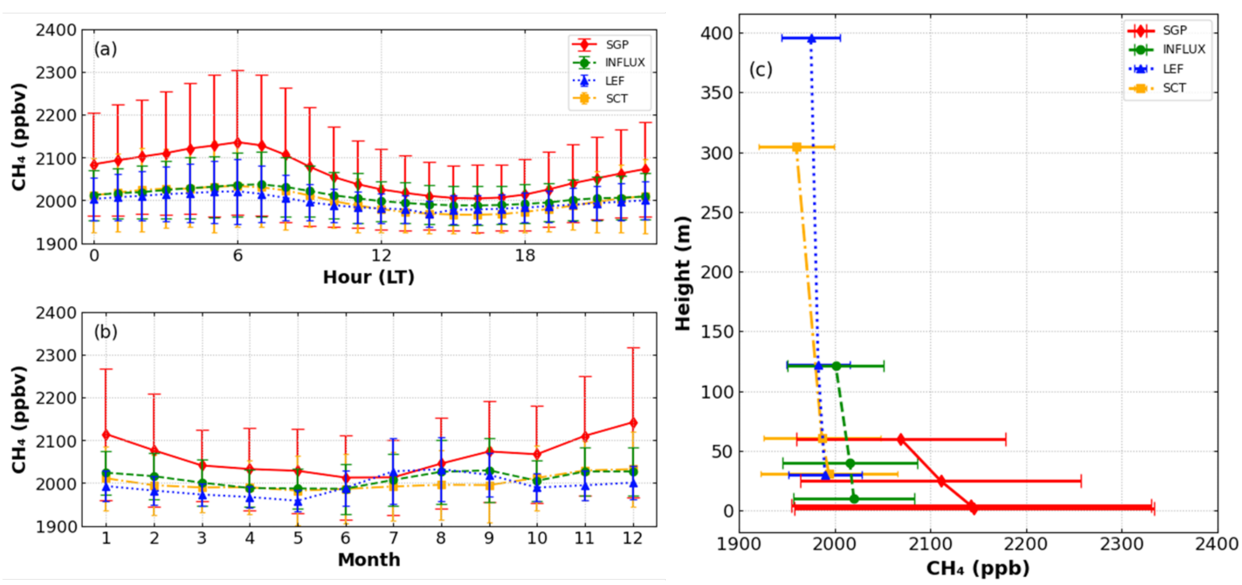

Figure 4.4 (a) Diurnal and (b) seasonal mean (lines) with standard deviation (error bars) of CH_4 at the heights marked with * in Table 1, and (c) vertical profiles of CH_4 at all heights listed in Table 1 for SGP (red), INFLUX (green), LEF (blue), and SCT (yellow). In panels (a) and (b), the mean and standard deviation are calculated from hourly averaged measurements taken from 2017 to 2020. Panel (c) shows vertical variations based on nighttime hourly measurements from 9 PM to 6 AM local time from 2017 to 2020. A 5-year trend was removed from the data on a daily basis to isolate short-term variations.

1) *Generally Higher CH_4 Concentration*: The CH_4 concentrations at SGP remain elevated across all seasons except July and times of day compared to other sites (Figures 4.4a and 4.4b). In July, however, CH_4 levels at the LEF site surpass those at SGP, likely due to strong emissions from nearby wetlands (Desai 2024; Yu et al. 2021). Nevertheless, SGP exhibits generally higher CH_4 concentrations year-round.

2) *Larger Diurnal Variations*: SGP displays pronounced diurnal fluctuations in CH_4 concentrations (Figure 4.4a). For example, at 6 AM, mean CH_4 concentrations at SGP reach 2135.6 ppb, compared to 2035.9 ppb at INFLUX, 2021.0 ppb at LEF, and 2033.3 ppb at SCT, indicating significantly higher at nighttime and early morning CH_4 levels at SGP.

3) *Larger Seasonal Variations*: CH_4 concentrations at SGP also show substantial seasonal variation, with winter months experiencing particularly high levels (Figure 4.4b). In December, for instance, mean CH_4 concentration at SGP reaches 2141.7 ppb, considerably higher than the CH_4 levels at other sites, which remain below 2040 ppb.

4) *Sharp Increases in Nocturnal Near-Surface CH_4:* CH_4 concentrations at SGP exhibit particularly high values near the surface at nighttime (Figure 4.4c): The average CH_4 concentration below 60 meters at SGP is 2116.98 ppb, and the vertical gradient in the lowest 60m is 1.27 $ppb \cdot m^{-1}$(more CH_4 near surface). In comparison, at INFLUX, the average CH_4 concentrations at 10m and 40m is 2018.10 ppb, and the vertical gradient between these two heights is only 0.37 $ppb \cdot m^{-1}$. Although LEF and SCT lack measurement heights below 30 meters, their respective measurements at 30-31 meters indicate significantly lower CH_4 concentrations, approximately 1990.0 ppb and 1994.1 ppb. This suggests that SGP may be strongly influenced by local sources and specific meteorological conditions that may not be fully accounted for in current emission inventories.

Existing inventories may underestimate local CH_4 emissions near SGP. As indicated by the EPA Greenhouse Gas Inventories (GHGI), emissions in Oklahoma predominantly originate from petroleum and natural gas systems, with significant contributions also from livestock-related activities such as enteric fermentation and manure management. However, detailed spatial analysis from Figure 4.1b and c reveals that the mean emission rate at SGP site grid cell is 2.61 $kg \cdot km^{-2} \cdot d^{-1}$ based on EPA monthly inventory in 2018, which indicates that the emission rate from the entire $0.25° \times 0.25°$ grid cell where SGP located in is about is 84 $kg \cdot hr^{-1}$. This emission rat-e is not particularly strong compared to other areas across the U.S. (Fig 4.1a). The major emission sources with rates exceeding 10 $kg \cdot km^2 \cdot d^{-1}$ are located more than 55 km (0.5°) away. Given that the flux footprint at a 25-meter measurement height at SGP is estimated to extend only up to 1 km (inferred from results in Chu et al. (2021)), and the concentration footprint up to 10 km (inferred from results in Schmid (1994)), it is unlikely that major emission sources located more than 55 km away would significantly influence CH_4 levels at SGP. Consequently, this spatial discrepancy suggests that local CH_4 emissions may be underreported in current inventories.

From a meteorological standpoint, CH_4 levels at SGP tend to peak during the night and early morning hours (Fig 4.4a), which are likely driven by specific climatic features at the site. such as the occurrence of LLJs and the persistence of a stable PBL, which inhibit vertical mixing and strengthen CH_4 accumulation near the surface.

In the next section, we will present a case study from October 30, 2020 to explore how meteorological conditions in the PBL influence surface CH_4 concentrations in detail.

4.4.2 A Case Study of Meteorological Influence on CH_4 Concentrations: October 30, 2020

This case study from October 30, 2020 provides a detailed analysis of how PBL conditions at SGP affect surface CH_4 concentrations. It reveals two distinct stages that highlight the interactions between CH_4 concentrations and PBL dynamics.

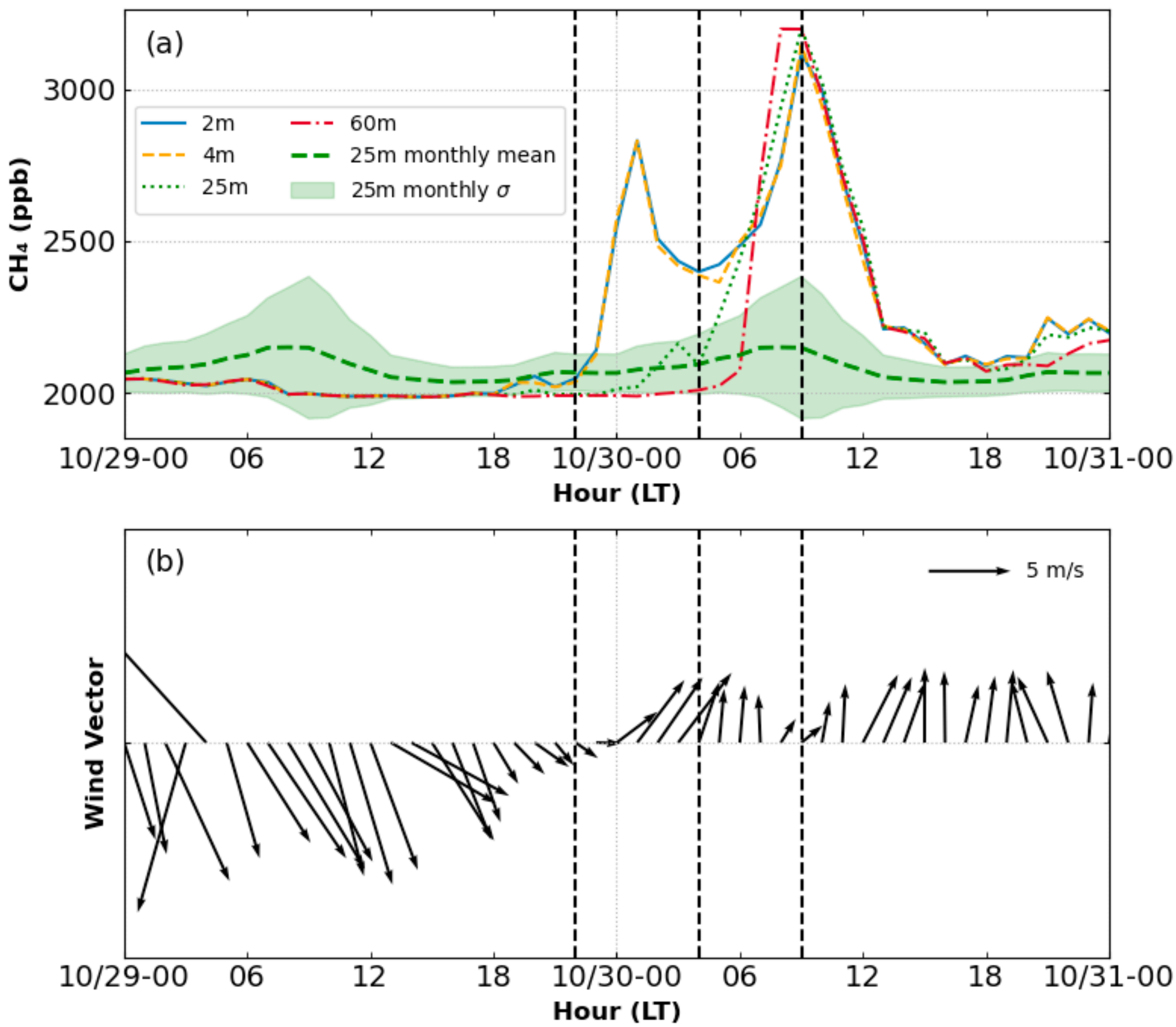

Figure 4.5 (a) Hourly averaged CH_4 concentration measured at 2m (blue solid), 4m (orange dashed), 25m (green dotted), and 60m (red dash dot), and monthly mean CH_4 concentration at 25m (green thick solid line) with standard deviations (green shade); (b) surface wind vector on Oct 29 and 30, 2020

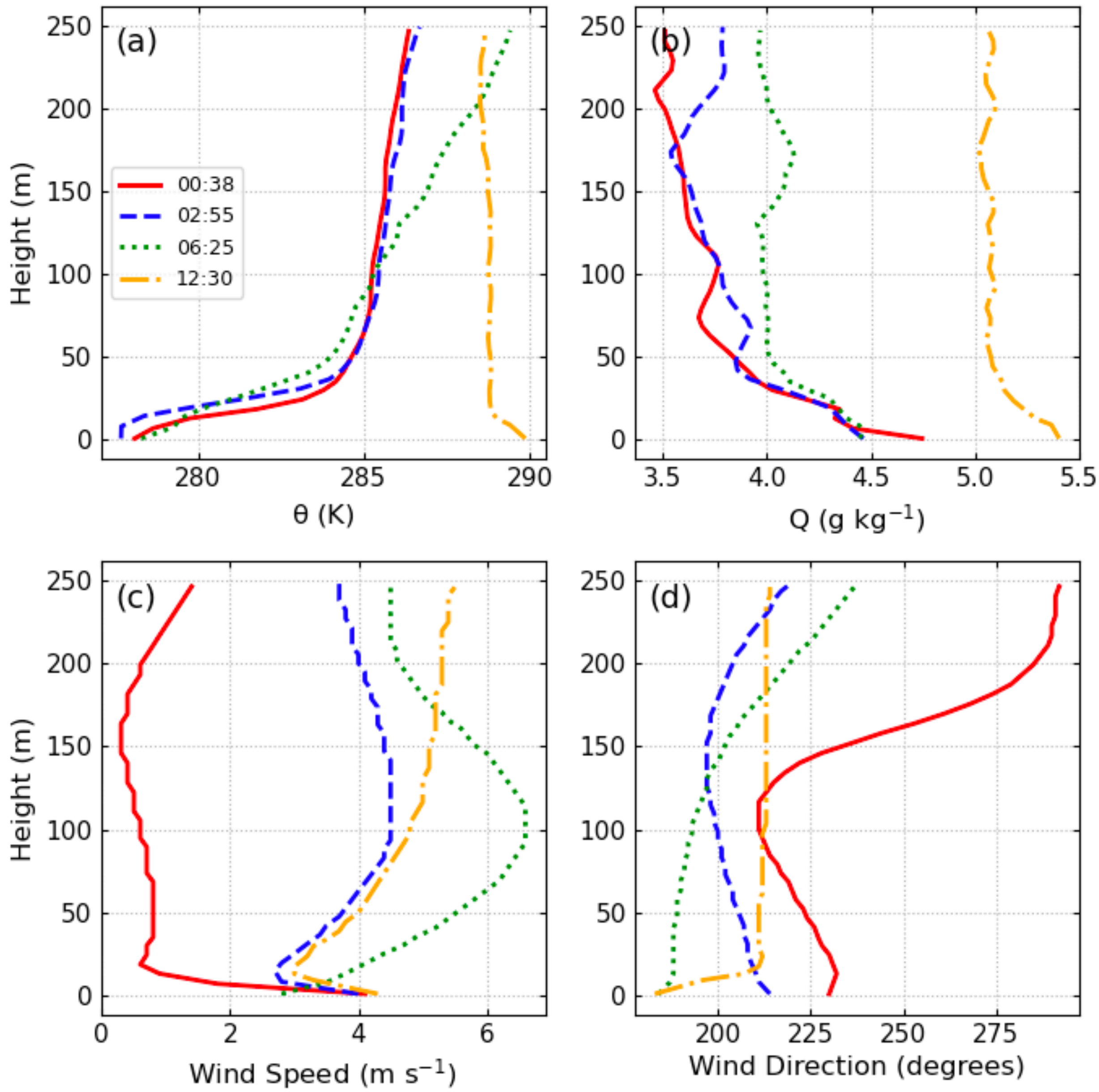

Figure 4.6 Balloon borne soundings for (a) potential temperature ($\boldsymbol{\theta}$), (b)specific humidity (Q), (c) Wind Speed, and (d) Wind Direction at 00:38 (red), 02:55 (blue), 06:25 (green), and 12:30 (yellow) on Oct 30, 2020

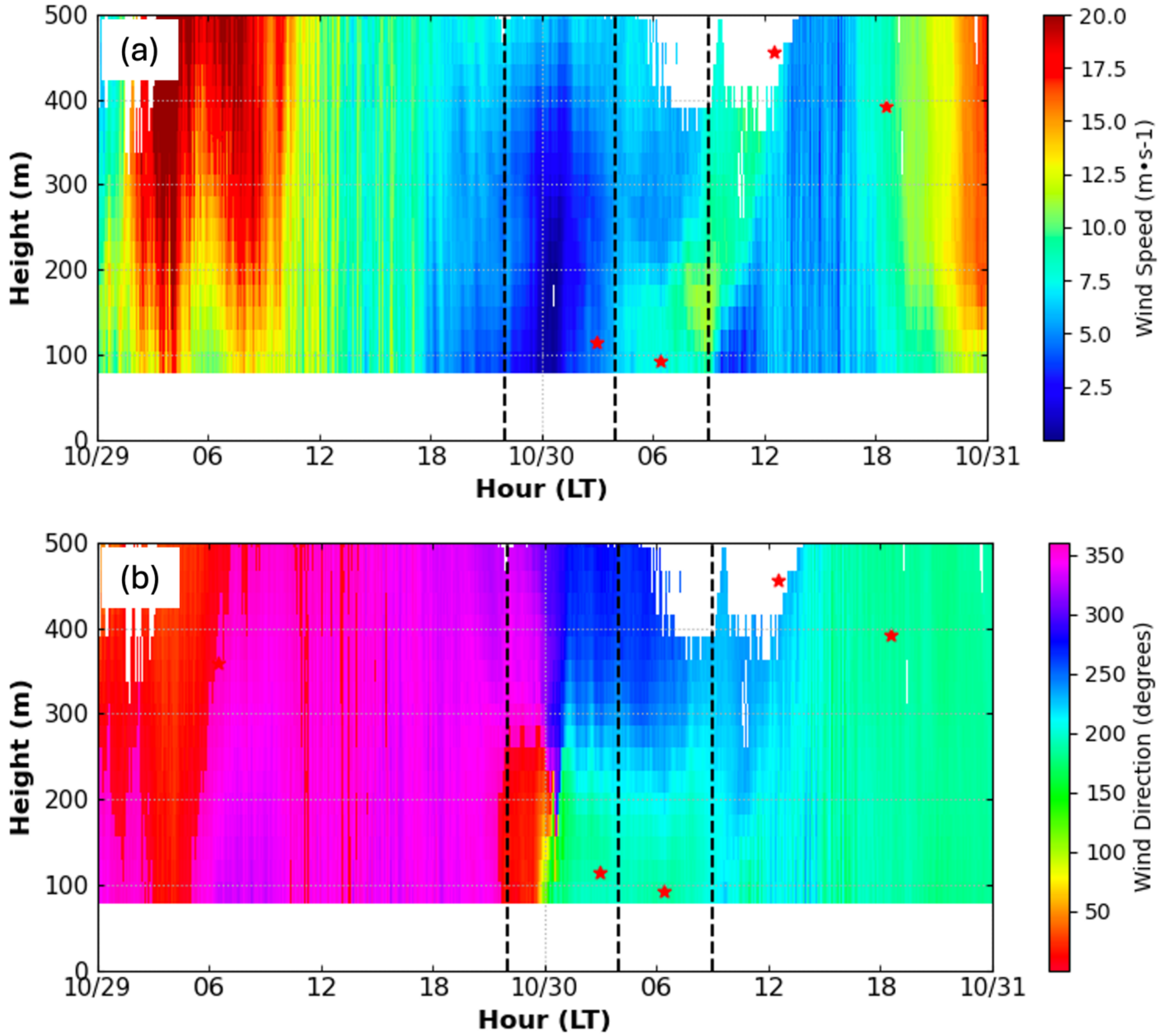

Figure 4.7 Doppler Lidar wind speed (a) and wind direction (b) on Oct 29 and 30, 2020. Red stars are PBLH inferred from balloon borne soundings with LLJ nose method introduced in 4.2.3.4.

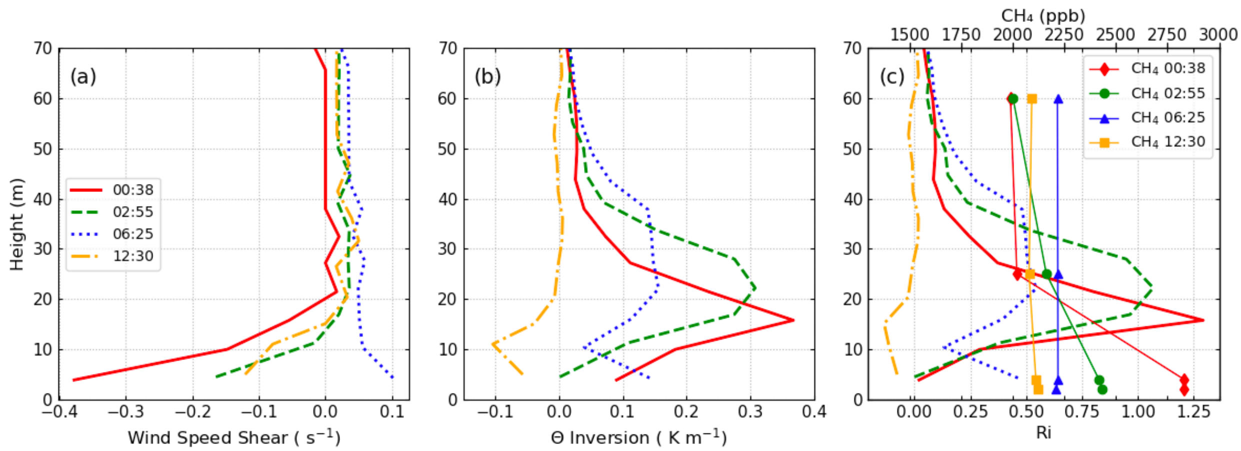

Figure 4.8 Balloon-borne sounding profiles on Oct 30, 2020 at SGP. Lines with no markers: (a) Wind speed shear, (b) θ inversion, and (c) Ri calculated with balloon borne soundings at 00:38 (red solid), 2:55(green dashed), 5:25 (blue dotted), and 12:30 (orange dashdot) on Oct 30, 2020; Thin line with markers in (c): Hourly-averaged $\boldsymbol{CH_4}$ concentration at 2m, 4m, 25m, and 60m, with the same color scheme as the solid lines to denote corresponding times of soundings – 00:38 (red diamond), 2:55(green circle), 5:25 (blue triangle), and 12:30 (orange square) on Oct 30, 2020.

<u>Stage I: 22:00 Oct 29 to 04:00 Oct 30</u>

The first stage, from 22:00 on Oct 29 to 04:00 on Oct 30, is characterized by a pronounced decoupling of CH_4 concentrations between the lower (2m and 4m) and upper (25m and 60m) measurement heights (Figure 4.5a). Despite mild surface wind shear, indicated by wind speeds of 4.1 m/s at the surface and 1.8 m/s at 6.8 meters (Figure 4.6), a strong potential temperature (θ) inversion at 00:38 and 02:55 suggests a highly stable boundary layer below 25 meters. Doppler lidar data (Figure 4.7a) corroborates this, showing a calm PBL under 400m during this period. The stability in the boundary layer limits vertical mixing, effectively trapping CH_4 near the surface.

The high Ri values, particularly below 25 meters (Figure 4.8c), indicate that turbulence is suppressed, as the stabilizing effect of the θ inversion outweighs the destabilizing wind shear. This results in a stratified air layer with limited vertical transport, allowing CH_4 to accumulate near the surface. The sharp increase in specific humidity (Q) at 15 meters, as shown in Figure 4.6(b), further supports this interpretation, suggesting a pronounced stratification that confines CH_4 to lower altitudes.

Additionally, the sharp rise in CH_4 concentrations at 2m and 4m around 11 PM (Figure 4.5a) corresponds to a shift in wind direction (Figures 4.5b and 4.7b), possibly indicating the activation or influence of a CH_4 source near SGP.

Stage II: 04:00 to Sunrise

By 06:25 AM, the PBL begins to mix more effectively due to the development of a low-level jet (LLJ) at 103 meters, with a peak wind speed of 6.6 m/s (Figure 4.5). The wind shear above 10 meters becomes more pronounced, generating mechanical turbulence that facilitates vertical mixing (Figure 4.7a). The θ inversion weakens (Figure 4.7b), and the Ri values drop closer to or below the critical threshold of 0.25 (Figure 4.7c), indicating a shift toward less stable atmospheric conditions. These changes result in more uniform CH_4 concentrations across the measured heights, marking a transition from the decoupling observed earlier.

Doppler lidar data shows that wind speeds begin to increase at approximately 100 meters around 04:00 (Fig 4.6a), and the LLJ strengthens as the morning progresses, lifting the PBLH and promoting further vertical mixing. By 12:30, the PBL has developed to 456 meters, and surface warming post-sunrise (sunrise time 07:52 at Lamont, OK on Oct 30,2020) intensifies vertical convection, redistributing CH_4 and smoothing out the surface anomalies observed earlier.

This case study demonstrates that elevated surface CH_4 concentrations are closely linked to stable PBL conditions, particularly when wind shear, θ inversion, and Ri values indicate limited vertical mixing. Conversely, when LLJ strength increases, especially after sunrise, enhanced wind shear promotes more efficient mixing, leading to a more uniform vertical profile of CH_4. The influence of solar heating further amplifies this effect, establishing a diurnal pattern in CH_4 dispersion.

This case suggests how a stable PBL is related to accumulated surface CH_4. In the next section, we will expand on this by statistically analyzing how meteorological factors contribute to CH_4 variability, providing a broader and more comprehensive understanding of their impact.

4.4.3 Statistical Impact of Meteorological Conditions on CH_4 Accumulation

High CH_4 anomalies at SGP are strongly associated with stable nocturnal PBL conditions, characterized by both mechanical and thermal stability. Mechanically, weak wind shear and low surface winds suppress turbulence, allowing CH_4 to accumulate near the surface. CH_4 anomalies above 200 ppb are primarily associated with low wind shear (below 0.1 s^{-1}) and weak surface wind speeds (less than 4 $m \cdot s^{-1}$) (Figure 4.9a). As wind shear increases, the CH_4 anomalies tend to decrease, suggesting that stronger mechanical mixing associated with higher wind shear disperses CH_4 more efficiently, thereby reducing the CH_4 concentration near the surface. Thermal stability, characterized by the strength of the potential temperature inversion, is a key factor in CH_4 accumulation. A positive correlation between CH_4 anomalies and inversion strength shows that stronger inversions consistently coincide with higher CH_4 concentrations ($y = 2648x - 117.6$, $r = 0.57$) (Figure 4.9b).

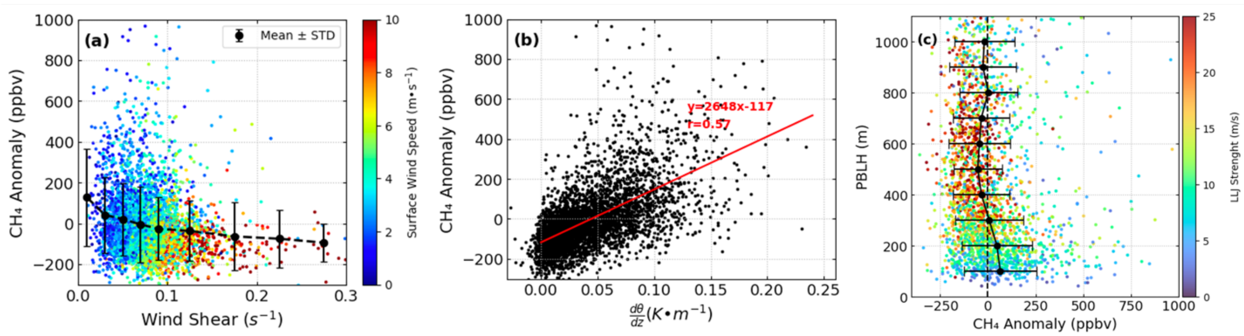

Figure 4.9 (a) Scatter of wind shear versus CH_4 anomaly, colored by the surface wind speed. Black error bars represent means with SDs of CH_4 anomalies in wind shear bins (with bins size 0.02 s^{-1} when wind shear is less than 0.1s^{-1}, and 0.05 s^{-1} when wind shear larger than 0.1s^{-1}) (b) scatter of CH_4 anomaly versus $\frac{d\theta}{dz}$ with red linear regression line and correlation coefficient r; (c) scatter of CH_4 anomalies versus PBLH. Black error bars represent means of CH_4 anomalies with SDs in PBLH bins (bins size 100m).

The combined effect of both mechanical and thermal stability is captured by PBLH, with the highest CH_4 anomalies occurring when the PBL is shallow (Figure 4.9c) – High CH_4 anomalies are generally observed when the PBL is shallow: enhancements of +65.1 ppb are noted at PBLHs of 50 to 150 meters, +47.2 ppb from 150 to 250 meters, and +6.8 ppb from 250 to 350 meters. Conversely, PBLHs above 350 meters are related to reduced surface CH_4 concentrations (CH_4 anomalies ranging from -2.8 to -40.1 ppb), suggesting less CH_4 accumulation under less stable atmospheric conditions.

As seen from the vertical CH_4 distributions across all PGS measurement heights at SGP, stable stratification strongly affects near-surface CH_4 accumulation and may cause decoupling in near-surface CH_4. Over the decade from 2012 to 2022, stable conditions with Ri values exceeding 0.4 were observed on 312 nights (271 nights in months from October to May), particularly below 30 meters. As illustrated in Fig 4.10: when the Ri exceeds 0.4 below 30m, the corresponding mean CH_4 concentrations at 2m and 4m are both above 2400 ppb, which is over 300 ppb higher than the CH_4 concentrations at 25m and 60m. This suggests that strong stratification at some height between 10m and 25m suppresses turbulence, effectively trapping CH_4 in the lowest 25 meters (or lower) of the atmosphere. While under weakly stable or neutral conditions (Ri<0.25 under 70m), turbulence enhances vertical mixing, leading to a more uniform vertical distribution of CH_4 below 70m compared to the stratified case in Figure 4.10b. This comparison highlights the significant influence of PBL stability on the vertical mixing of CH_4.

The higher CH_4 concentrations near the surface in winter nights and early mornings at SGP compared to other sites can be explained by less buoyant production of turbulence. Wind shear at during winter nights and mornings is similar to that at other sites, indicating comparable levels of mechanical mixing (Figure 4.11a). However, the θ inversion at SGP is much stronger (~0.027 K/m at 24 meters), compared to values ranging from 0.01 to 0.017 K/m at INFLUX, LEF, and SCT (Figure 4.11b). This stronger inversion results in higher Ri values at SGP, around 0.1, whereas Ri values at the other sites are much lower (Figure 4.11c). The elevated Ri at SGP suppresses turbulence, limiting CH_4 dispersion and leading to higher CH_4 concentrations near the surface, especially during stable, cold winter mornings.

However, meteorological factors like stable PBL conditions alone may not fully explain all surface CH_4 enhancement. For instance, we also observed cases of negative CH_4 anomalies under similar stable PBL conditions, where CH_4 anomalies were below zero even when the θ inversion exceeded 0.1 K/m (Figure 4.10). This suggests that stable PBL conditions are not always associated with elevated surface CH_4 concentrations. Therefore, additional factors, particularly underreported or unaccounted local emissions, may contribute to the observed CH_4 levels at SGP. This necessitates further exploration of potential sources underestimated in existing inventories to fully account for the variability in surface CH_4 concentrations.

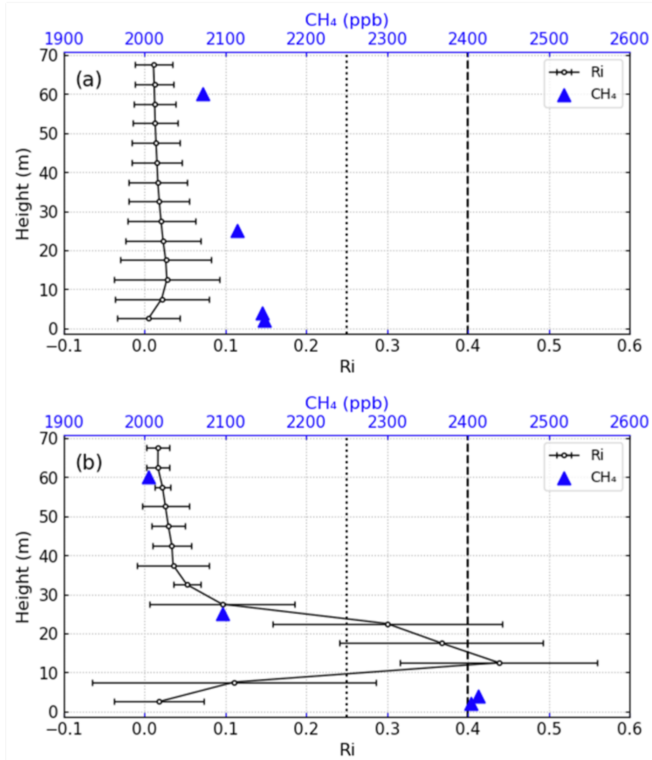

Figure 4.10 Mean Ri profiles with SD from nocturnal balloon-borne soundings (black errorbar) and corresponding CH_4 concentrations at 2m, 4m, 25m, and 60m (blue triangle) during the same time period, using data from 2012 to 2023. (a) Displays conditions where Ri under 70m is less than 0.25; (b) Shows conditions where the maximum Ri below 30m is greater than 0.4. vertical dashed (dotted) line in (a) and (b) indicate where Ri is 0.4 (0.25).

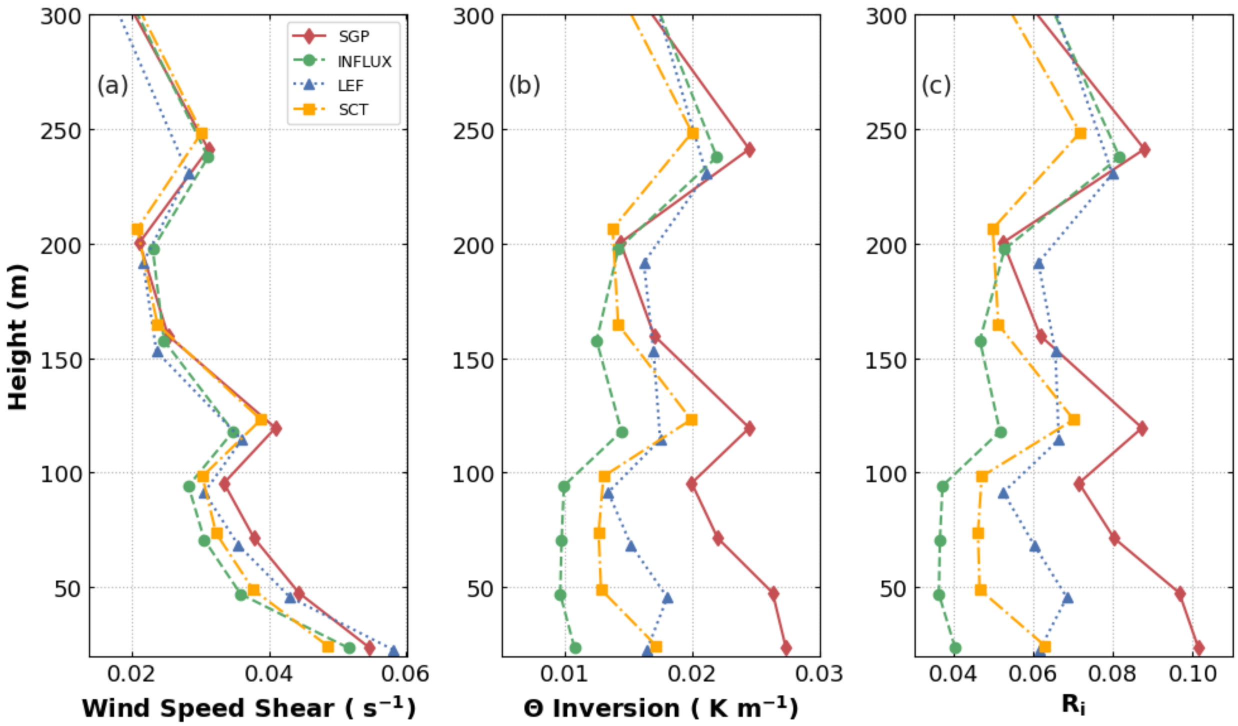

Figure 4.11 Mean winter (DJF) nocturnal (9 PM to 6 AM Local Time) (a) wind speed shear, (b) θ inversion, and (c) Ri under 300 meters for 2017-2020 from WRF simulations at SGP (red), INFLUX (blue), LEF (green), and SCT (orange). WRF configurations are after Hu et al. (2020).

4.4.4 Field Campaign to Identify and Quantify Potential CH_4 Sources Near SGP

Given that meteorological factors alone cannot fully account for the observed CH_4 variations, it's essential to investigate potential local sources contributing to these anomalies. Local CH_4 anomalies at SGP are closely tied to specific wind directions, suggesting unaccounted emission sources. Wind direction analysis (Fig 4.12) suggested that high surface CH_4 anomalies predominantly occurred when winds were blowing from two main sectors: 140° – 240° and 300°. These directions correspond to potential emission sources, including nearby agricultural and industrial activities, indicating that local CH_4 emissions may play a more significant role than previously captured by existing inventories, such as the GHGI and the FOG inventories.

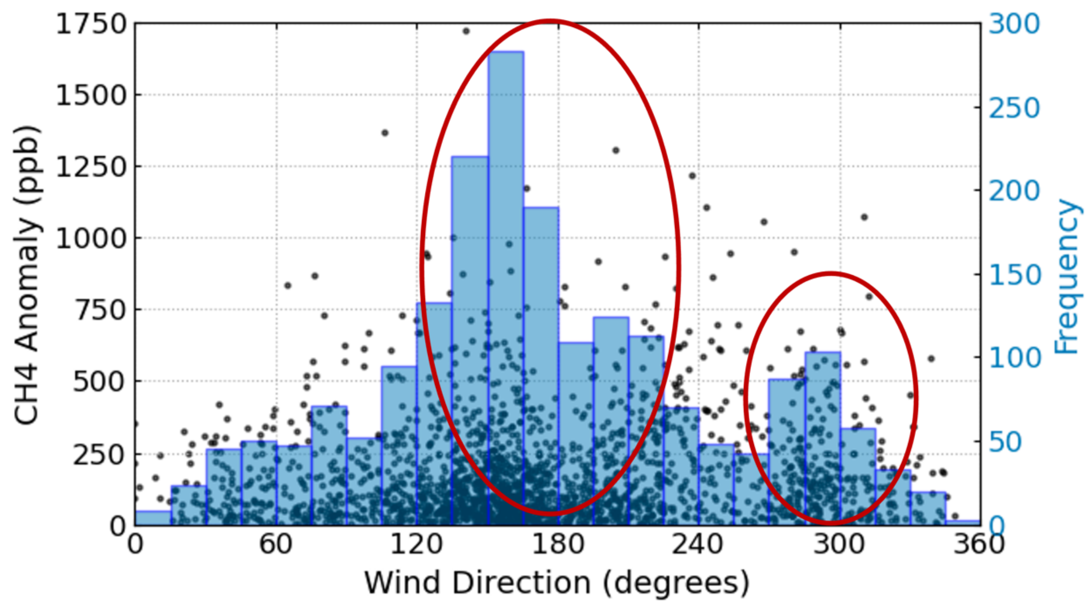

Figure 4.12 Distribution of Wind Directions Associated with CH_4 Anomalies from 2012 to 2023. This figure presents the frequency of wind directions corresponding to positive CH_4 anomalies (depicted as a blue histogram) alongside a scatter plot (black points) showing the relationship between CH_4 anomalies and wind directions, based on hourly averaged data.

Table 4.2 Potential CH_4 sources near the SGP site inferring from both satellite image and wind direction analysis in Figure 4.12

Potential Source	Lat, Lon	Degree to the SGP site	Distance to the SGP site	Potential methane emitter
Concentrated AFO	36.6413, -97.5374	310°	5800m	cattle, wastewater pond, compost, natural gas leak
Open-range Cattle	36.5983, -97.4836	140° – 240°	850m	cattle, cattle excrement

Our field observations identified an AFO located approximately 5.8 km from SGP at 310 degrees. The AFO houses around 15,000 cattle according to records from the Oklahoma Department of Agriculture and Forestry's Concentrated Animal Feeding Operation (CAFO) permit database. The potential CH_4 emissions at the AFO likely arise from open lots, wastewater ponds, and compost areas. Based on previous studies on the emission rate from per cow (0.22 to 1.39 kg per cow per day) (Arndt et al. 2018; Bjorneberg et al. 2009; Hamilton et al. 2010; Leytem et al.

2011; Sun et al. 2008; Todd et al. 2011; VanderZaag et al. 2014; Vechi and Scheutz 2023), the estimated CH_4 emission rate from this facility could exceed 130 $kg \cdot hr^{-1}$. However, the actual emission rate may vary significantly due to factors such as cattle diet (Chang et al. 2021), diurnal activity patterns (Leytem et al. 2011), and wastewater pond characteristics (Leytem et al. 2017; VanderZaag et al. 2014). The actual counts of cattle during our field campaign period also remain uncertain even with the records from the permit database.

To refine the emission rate estimates, we conducted a targeted field campaign from June 23 to 26, 2024, focusing on early morning measurements between approximately 4:30 and 9:00 AM local time. The most significant observation occurred at around 6:30 AM on June 26, while driving downwind of the AFO along the road on its east side. We observed an exceptionally high CH_4 concentration exceeding 6000 ppb downwind of the wastewater pond, which is located approximately 20 meters from the road (Figure 4.13). At the time of this sharp enhancement, the wind direction was 304 degrees, directly aligning the pond with our measurement path. Further downwind of the open lots, we observed CH_4 concentrations exceeding 4000 ppb. The covered compost area, located downwind of the open lots, showed CH_4 concentrations exceeding 3000 ppb, although it was difficult to distinguish its contribution from that of the open lots. These strong CH_4 enhancements suggest a substantial emission hotspot associated with the open lots, wastewater pond, and compost areas in the AFO.

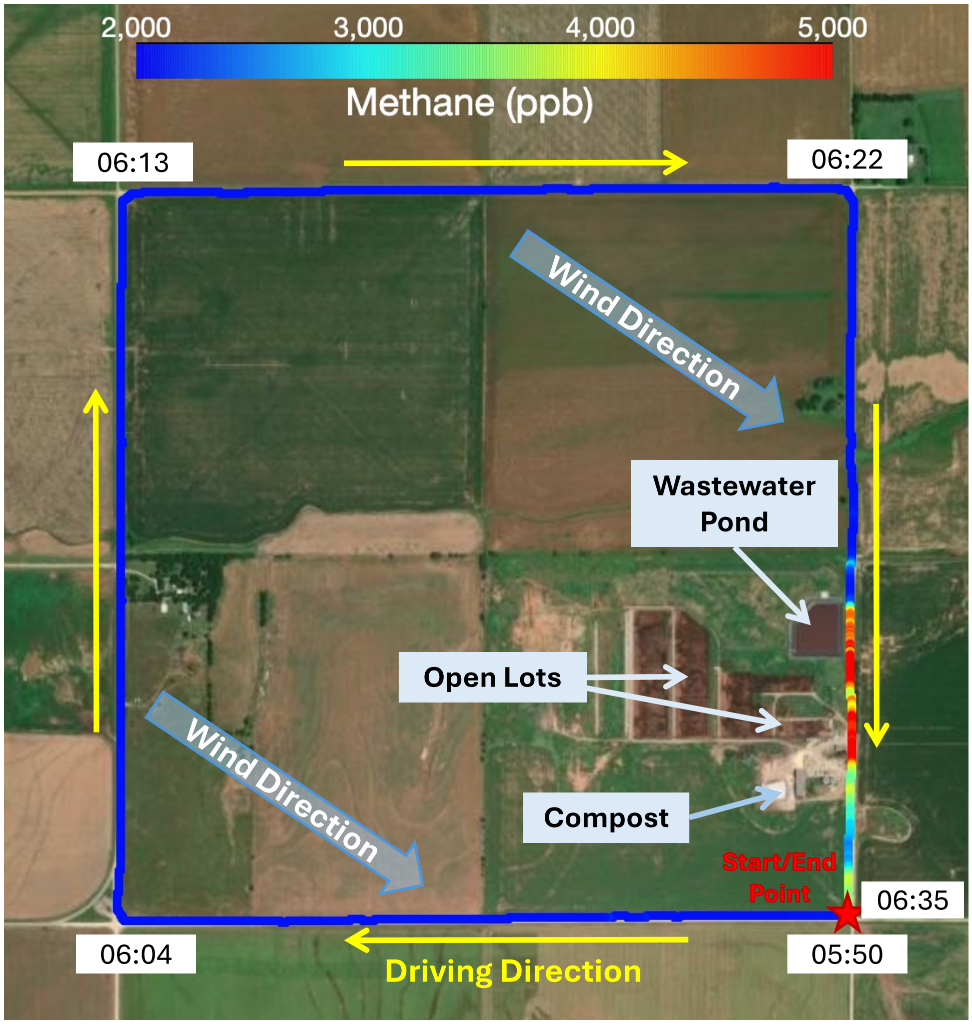

Figure 4.13 CH_4 measured using LI-7810 between 6:00-6:50 local time near the AFO during the field measurement campaign on June 26, 2024. The color stands for CH_4 concentration.

Using the mass balance method (as introduced in Section 4.2.3.3), the estimated CH_4 emission rate is at least 92 $kg{\cdot}hr^{-1}$, assuming the PBLH in Eqn.1 is 15 meters. Notably, this minimum estimate already exceeds the emission rate of 84 $kg{\cdot}hr^{-1}$ for the entire grid cell as reported in the EPA GHGI (detailed in Section 4.3.1). The PBLH inferred from Doppler lidar vertical velocity variance sharply decreases from 2.3 $m^2\ s^{-2}$ at 15 meters to a smaller value at 45 meters, although vertical velocity variance data at 6:30 AM is unavailable. For reference, the variance was 0.68 at 5:50 AM and 0.2 at 7:30 AM. If we assume that the surface CH_4 enhancement is uniform up to 45 meters, the emission rate increases to 275 kg hr^{-1}. The accuracy of emission calculations would greatly benefit from precise vertical CH_4 profiles, as the current estimates are highly sensitive to assumptions about PBLH.

During the campaign, we also detected a significant CH_4 leak from an underground natural gas pipeline about 500 meters from the AFO, where concentrations spiked to 40,000 ppb. This, combined with AFO emissions, points to a substantial local CH_4 source likely underreported in current inventories.

The AFO and the natural gas leak could be the potential sources leading to the CH_4 enhancement at 300 degrees in the wind direction analysis, and we also identified potential CH_4 emissions in the 140° – 240° wind sector—45 open-range cattle located about 850 meters southeast of SGP, within the 140° – 180° during our field campaign. At 7:30 AM, we detected a significant CH_4 enhancement exceeding 500 ppb downwind of this small group of cows. According to ARM facility staff, during the winter months, cows are corralled and fed hay instead of grazing on open pasture due to the lack of grass. While this smaller group of cattle may not contribute as much CH_4 as larger AFOs, their close proximity to SGP can still cause notable local CH_4 enhancements, especially under stable PBL conditions. This finding highlights the role of smaller livestock operations in influencing local CH_4 levels under specific meteorological conditions.

Our field campaign results suggest that agricultural activities, particularly from cattle, are the dominant contributors to elevated CH_4 levels at SGP. Additionally, leaks from natural gas systems, such as the detected pipeline, further contribute to CH_4 enhancements. This dual source of emissions, particularly during stable PBL conditions, underscores the complex relationship between agriculture, industry, and local CH_4 dynamics.

4.5 Conclusions

This study highlights the complex interplay between meteorological conditions and local emissions in driving surface CH_4 anomalies at SGP. Long-term analysis of CH_4 concentration trends from 2017 to 2020 revealed that SGP consistently exhibits higher surface CH_4 concentrations compared to other sites across the United States, particularly during winter and early morning hours. Our analysis showed that while meteorological factors such as stable PBL conditions with a PBLH lower than 350m, weak wind shear (less than 0.1 s^{-1}), and strong θ inversions (greater than 0.5 $K \cdot m^{-1}$) contribute significantly to CH_4 accumulation near the surface. As seen from Ri, very shallow laminar flow under 25m often occur at SGP at night, which largely reduce the vertical upward dispersion from surface emission to heights above 25m, and is related to vertical decoupling from the vertical CH_4 concentration distribution – leading to about 300 enhancement under 10m on average at these nights.

However, such stable PBL and reduction is turbulence are insufficient to explain the surface enhancement of CH_4 concentrations at SGP. Wind direction analysis suggests there can be nearby CH_4 sourced from two sectors: 140° – 240° and 300°. To address the potential underestimation of local emissions, we conducted a field campaign to identify specific CH_4 sources near SGP. Our results identified an AFO housing 15,000 cattle approximately 5.8 km from SGP as a major contributor to CH_4 enhancements, with emission rates estimated to be at least 92 $kg \cdot hr^{-1}$, exceeding the emission rate from EPA inventories for the entire grid cell. Further analysis revealed additional potential sources, including a smaller group of 45 open-range cattle southeast of SGP, which caused localized CH_4 enhancements. Additionally, our campaign detected a significant CH_4

leak from an underground natural gas pipeline near the AFO, further emphasizing the importance of underreported emissions from industrial sources.

Our results highlight the need for more detailed emission inventories and precise vertical CH_4 profiles to improve the accuracy of CH_4 source quantification. This integrated approach is essential for advancing CH_4 monitoring and better understanding greenhouse gas dynamics in agricultural and industrial regions like SGP.

Chapter 5 Underestimated Methane Emissions at SGP ARM Site: Field Campaign Insights and WRF-Chem Simulations

5.1 Introduction

Methane (CH_4) is the second most prevalent greenhouse gas, which significantly influences atmospheric chemistry and climate dynamics (Myhre et al. 2014; Stocker et al. 2013). Despite the progress in understanding the sources and sinks of CH_4, quantifying emissions—especially from localized sources such as wetlands, agriculture, and fossil fuel activities—continues to be a critical challenge in atmospheric sciences (Bamberger et al. 2014; Bridgham et al. 2013; Kuze et al. 2020; Lamb et al. 2015; Riddick et al. 2017). Discrepancies between observed CH_4 concentrations and emission estimates derived from inventories highlight persistent uncertainties and potential underestimations (Alvarez et al. 2018; Chan et al. 2020; Chen et al. 2022; Hmiel et al. 2020; Hristov et al. 2018; Shen et al. 2022; Tyner and Johnson 2021; Zhang et al. 2020).

Accurate CH_4 emission inventories are crucial for atmospheric models like the Weather Research and Forecasting model with Chemistry (WRF-Chem), which rely on emissions inventories to simulate the transport, mixing, and chemical reactions of atmospheric gases, like studies in Beck et al. (2013); Zhao et al. (2019). However, underestimations in these inventories can propagate through the modeling process, leading to inaccurate predictions about air quality and climate, ultimately hindering the development of effective mitigation strategies (Tibrewal et al. 2024; Wang et al. 2024)

The Southern Great Plains (SGP) site, part of the Atmospheric Radiation Measurement (ARM) network, presents an intriguing case for CH_4 research due to consistently higher recorded CH_4 concentrations compared to other U.S. observational sites (Miller et al. 2013; Saito et al. 2013;

Turner et al. 2016), as discussed in Chapter 4. This anomaly provides a valuable opportunity to reassess the assumptions that current CH_4 inventories, like the U.S. EPA's Greenhouse Gas Inventory (GHGI), often fail to capture small-scale emissions, which are significant contributors to regional CH_4 budgets. This limitation makes it likely that localized sources, such as concentrated animal feeding operations (AFOs) and natural gas leaks, are underrepresented in the inventories, thus requiring a more thorough investigation into these overlooked contributions. Hereafter, we refer to the SGP site simply as SGP.

To address these challenges of underestimating CH_4 emissions in regional inventories, we conducted a targeted field campaign in June 2024 at the SGP site. This campaign primarily aimed to investigate CH_4 emissions from a concentrated AFO located 5.8 km northwest of the SGP. By measuring CH_4 concentrations around the AFO and applying a top-down mass balance method, we quantified CH_4 emission rates based on observed atmospheric CH_4 concentrations. These refined emission estimates offer insights into how local sources, such as AFOs, contribute to higher-than-expected CH_4 concentrations at SGP, thus enhancing the accuracy of CH_4 inventories and supporting more precise climate modeling efforts.

By integrating the field measurements with advanced atmospheric chemistry transport models like Weather Research and Forecasting model with Greenhouse Gas (WRF-GHG), this study seeks to improve the understanding of CH_4 dynamics on a regional scale and their broader impact on global CH_4 inventories. The findings contribute to enhancing the accuracy of atmospheric models, offering critical insights that support the development of more effective climate policies and strategies aimed at mitigating CH_4 emissions.

5.2 Materials and Methods

5.2.1 Study Farm

The concentrated AFO investigated in this study is located in Grant County, northern Oklahoma, and is surrounded by crop fields, as shown in Figure 5.1. This facility houses approximately 15,000 beef cattle, according to records from the Oklahoma Department of Agriculture and Forestry's Concentrated Animal Feeding Operation (CAFO) permit database. From satellite imagery, the total area of the AFO is estimated to cover around 200,000 square meters. The facility includes open lots of around 75,000 m^2, a wastewater pond occupying about 14,000 m^2, and a composting area of roughly 3,600 m^2, both of which are potential sources of CH_4 emissions due to the decomposition of organic material and waste from cattle operations. The presence of these sources, combined with the dense livestock population, underscores the significance of this AFO in contributing to local CH_4 emissions.

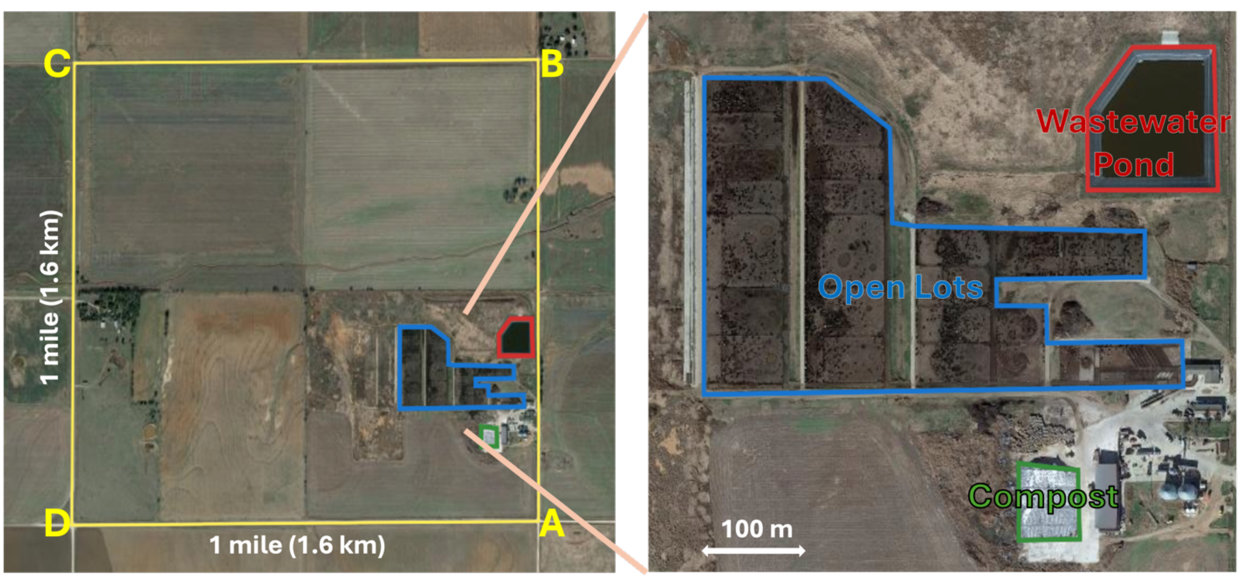

Figure 5.1 The layout of the concentrated AFO in Grant County, Oklahoma, and the surrounding area. The left panel shows the location of AFO within a 1-mile by 1-mile grid, with roads marked in yellow where driving and methane measurements were conducted during the field campaign. The right panel provides a close-up satellite image of the AFO including a wastewater pond (outlined in red), open lots (outlined in blue), and a covered compost area (outlined in green).

These components are potential sources of CH_4 emissions, contributing to localized atmospheric CH_4 concentrations. Satellite image was accessed on Oct 15, 2024.

5.2.2 Field Measurements

Our primary objective was to estimate the emissions of CH_4 from the three main sources located on the farm, which included the open lots, wastewater pond, and composting areas (Fig 5.1). The concentrations of CH_4 were continuously measured using a LI-COR LI-7810 $CH_4/CO_2/H_2O$ Trace Gas Analyzer (https://www.licor.com/env/products/trace-gas/LI-7810, LI-COR Biosciences, Lincoln, Nebraska, USA), which provides high-precision readings at a rate of one sample per second (1 Hz). Prior to the study, the analyzer was recalibrated in June 2024 to ensure measurement accuracy.

The analyzer was mounted on the driver's window of a pickup truck, which allowed us to take real-time measurements of CH_4 concentrations while driving along the roads surrounding the AFO (Fig 5.1). The vehicle was driven at a steady speed of approximately 3 mph to ensure consistent sampling. The field measurements were carried out during the early morning hours from 4:30 to 8:00 AM **local time**, over the period of June 23-26, 2024.

5.2.3 WRF-GHG simulations

In this study, we used an enhanced version of the WRF-VPRM model, referred to as WRF-GHG, to simulate CH_4 emissions and transport. WRF-GHG builds on the Weather Research and Forecasting model coupled with the Vegetation Photosynthesis and Respiration Model (VPRM) for biogenic CO_2 fluxes (Ahmadov et al. 2007; Mahadevan et al. 2008; Xiao et al. 2004), which has previously been applied to investigate CO_2 fluxes and concentrations at regional scales (Dong et al. 2021; Hu et al. 2020; Li et al. 2023; Li et al. 2020)

For this work, WRF-GHG was further developed to include CH_4 by coupling with the Copernicus Atmosphere Monitoring Service (CAMS) CH_4 global simulation for initial and boundary conditions. The model also integrates CH_4 emissions from wetlands using the WetCHARTs dataset (Bloom et al. 2017) and anthropogenic emissions. This enhanced version of WRF-GHG has demonstrated its capability in capturing both monthly variations and episodic events of CO_2 and CH_4 concentrations associated with frontal passages across the United States.

The simulation results were validated against multiple datasets, including satellite observations from the Total Carbon Column Observing Network (TCCON), OCO-2, and TROPOMI, as well as in-situ measurements from the GLOBALVIEW obspack data (Hu et al. 2021).

The spatial resolution of the model was set at 32 meters by 32 meters with a temporal resolution of 5 minutes to capture fine-scale variability in emissions and concentrations.

5.2.4 Emission Rate Estimation

5.2.4.1 Construction of Pseudo Vertical CH_4 Concentration Profile

Since our field measurements were limited to surface-level CH_4 concentrations and lacked information on the vertical distribution, we constructed a pseudo vertical profile to approximate CH_4 distribution throughout the PBL. To achieve this, we used the WRF-GHG simulated CH_4 profiles as a reference as in Figure 5.2.

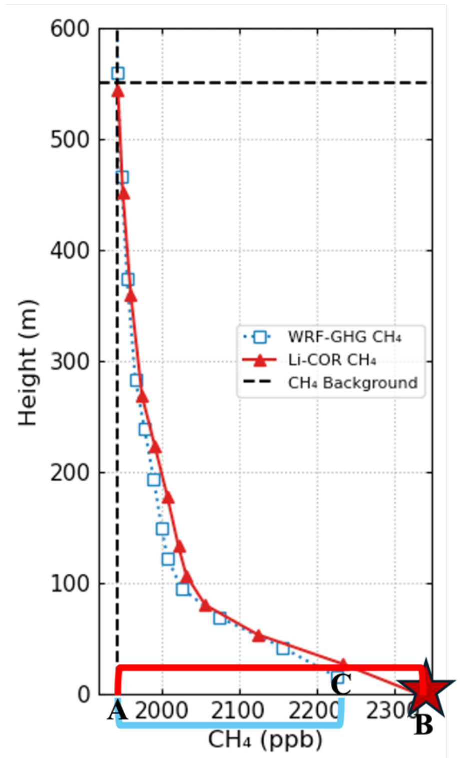

Figure 5.2 Example of methods to generate pseudo CH_4 profile from WRF-GHG CH_4 and radiosonde-determined PBLH

The WRF-GHG model provides CH_4 concentration profiles at a spatial resolution of 32m×32m with temporal updates every 5 minutes, while the LI-7810 instrument measured surface-level CH_4 concentrations at a frequency of one sample per second. For each second of LI-7810 data, we identified the closest WRF-GHG CH_4 profile based on both time and location to construct a corresponding pseudo vertical profile. We introduce the method use the profile in Figure 5.2 as an example:

1) **Identify PBLH from Radiosonde Profiles**: For each surface LI-7810 CH_4 measurement, determine the planetary boundary layer height from the nearest-in-time radiosonde profile, using the height of the low-level jet (LLJ) nose as the PBLH indicator.

2) **Retrieve WRF-GHG CH_4 Profiles**: Find the closest WRF-GHG CH_4 profile in both time and location corresponding to the LI-7810 measurement.

3) **Determine Background CH_4 Concentration**: Define the background CH_4 concentration as the mean CH_4 concentration in the WRF-GHG profile levels above the identified PBLH.

4) **Calculate Surface CH_4 Enhancements and Ratios**: Compute the CH_4 observation enhancement by subtracting the background CH_4 concentration from the LI-7810 measured CH_4 (enhancement from A and B in Figure 5.2). Similarly, calculate the bottom-level CH_4 enhancement by subtracting the background CH_4 concentration from the bottom-level CH_4 concentration in the WRF-GHG profile. Determine the ratio between these two enhancements.

5) **Generate Pseudo CH_4 Profiles**: Apply the calculated ratio to scale the WRF-GHG CH_4 profile, adjusting the profile to match the observed enhancements. The adjusted profile, referred to as the Pseudo CH_4 profile, represents the scaled CH_4 distribution.

This ensured that every LI-7810 surface measurement was paired with an appropriate WRF-GHG vertical profile. This method is relatively insensitive to the PBLH, as CH_4 concentrations in the troposphere above the PBLH exhibit minimal vertical variation. For the four analyzed days, even if the PBLH were to double, the estimated emission rate would change by less than 25%.

5.2.4.2 Application of the Mass Balance Method on Pseudo Vertical CH_4 Profiles

To estimate CH_4 emissions from our field campaign data, we employed the mass balance method. This approach calculates emission rates by integrating the difference between CH_4 concentrations measured upwind (background) and downwind (enhanced) across the width of the plume (2b) and from the ground (z_{ground}) up to the top of the PBL (PBLH) (Karion et al. 2015; Lavoie et al. 2015; Pandey et al. 2019; Peischl et al. 2015). The emission flux (F_{CH_4}) is determined using the formula:

$$F_{CH_4} = \int_{x_0}^{x_1} v\cos\alpha\left(\int_{z_{ground}}^{\mathrm{PBLH}} n_{air} \cdot [CH_4]dz\right) dx, \quad (5.1)$$

where n_{air} is the molar dry air density, calculated using the ideal gas law based on near-surface pressure and temperature from balloon-borne soundings. $[CH_4]$ the pseudo vertical CH_4 profile, constructed as described earlier in 3.3.1. v is the wind speed measured at the ARM surface meteorological station. $v\cos\alpha$ is wind speed component normal to the driving track. dx is the distance between consecutive LI-7810 samples, with x_0 marking the start and x_1 the end of the measurement path along the route. This method assumes that wind direction and speed remain constant throughout the measurement period.

The method has known uncertainties, including: 1. It is based on the assumption that all measurements are measured at a simultaneous time, neglecting the meteorological condition and emission change over time during the measurement; 2. The uncertainty from the pseudo CH_4 profile: we are lack of vertical profile info of the CH_4, even though inferring from WRF simulation has been the best way now we can estimate the true CH_4 profile, uncertainties still exist from both the uncertainty of WRF simulation itself and how likely the true profile is from the WRF CH_4 profile, 3. The uncertainty from meteorological conditions: we use the meteorological states from the surface meteorology station at the SGP ARM site, which is about 5.8km to the southeast of the AFO.

5.3 Results

5.3.1 Initial Exploration on AFO CH_4 influences on SGP site using WRF-GHG

In Chapter 4, we identified several key characteristics of the SGP ARM site related to CH_4 dynamics: 1) consistently high surface CH_4 concentrations compared to other sites across the U.S.; 2) pronounced diurnal variations; 3) marked seasonal variations; and 4) sharp nocturnal increases in near-surface CH_4. These phenomena are difficult to fully explain using current CH_4 inventories, such as the EPA Greenhouse Gas Inventories (GHGI). This raises questions about whether these inventories are underestimating CH_4 emissions in the region.

We hypothesize that the AFO located 5.8 km northwest of the SGP ARM site could be a significant local CH_4 source contributing to these anomalies. To test this, we plan to use the WRF-GHG model to simulate CH_4 dispersion from the AFO and evaluate whether it can explain the observed CH_4 concentration enhancements at SGP. This modeling approach will help determine if emissions from the AFO are substantial enough to account for the CH_4 trends identified in Chapter 4, offering insights into potential gaps in current emission inventories.

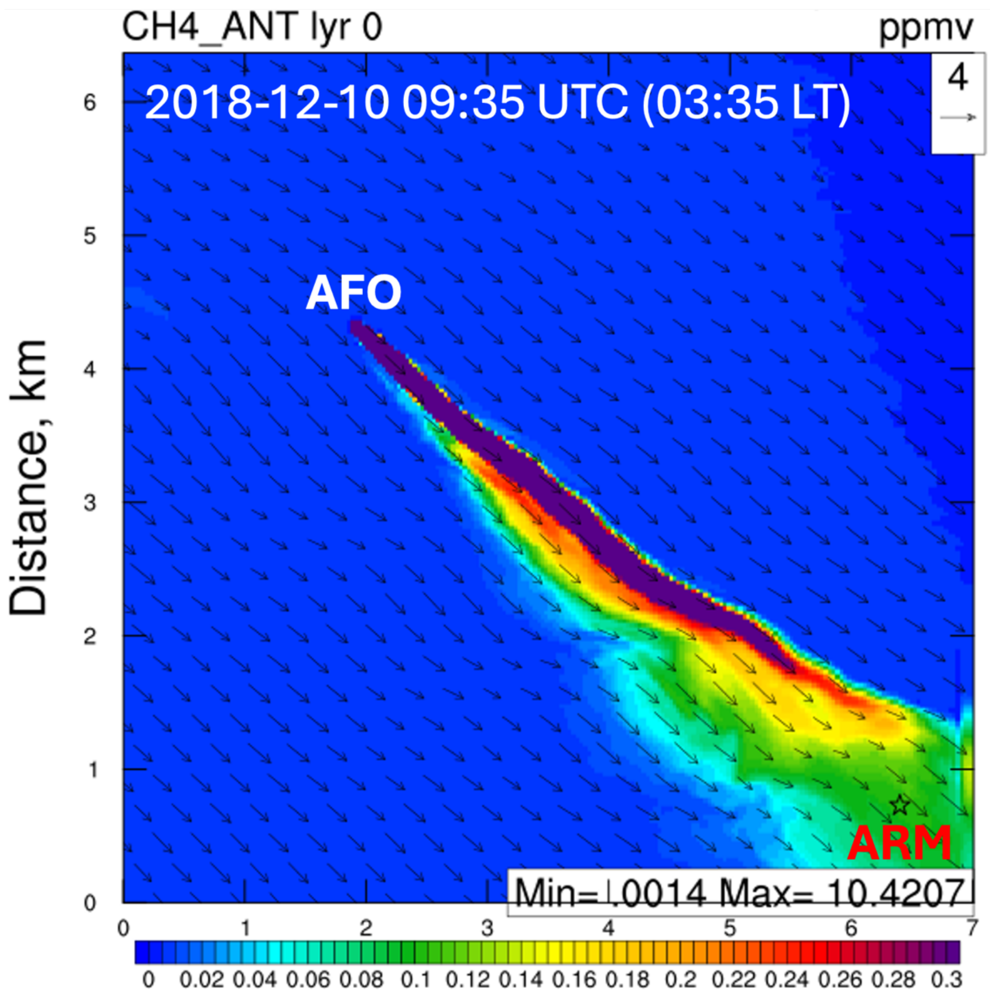

Figure 5.3 WRF-GHG simulation showing the dispersion of CH_4 from a 100 kg·hr^{-1} point source located at the AFO on December 10, 2018, at 09:35 UTC (03:35 local time). The wind arrows indicate the wind direction, with the SGP ARM site marked by a star, approximately 5.8 km southeast of the AFO. Simulated and plotted by Xiao-Ming Hu.

We simulated CH_4 dispersion under the meteorological conditions observed on December 10, 2018, when the surface wind speed was 5.1 m·s^{-1} at 305 degrees, consistent with the WRF-GHG model. The simulation (Fig 5.3) indicates that the AFO emissions increase CH_4 concentrations near the SGP site by about 100 ppb at the surface. However, tower measurements at 3:30 AM local time show a CH_4 concentration of 2619 ppb—587 ppb higher than the day before, when the wind direction was from the north. This significant discrepancy between observed and modeled CH_4 levels suggests that the actual emission rate from the AFO might be higher than the 100 kg·hr^{-1} assumed in the simulation.

Interestingly, the WRF-GHG simulation underestimates the observed CH_4 enhancement, predicting only a 100 ppb increase. This discrepancy suggests that the actual emission rate from the AFO may be larger than the 100 kg·hr^{-1} used in the simulation. Therefore, further refinement of emission estimates is required to match the observed data, indicating the potential for larger emissions from the AFO than currently modeled.

5.3.2 Estimated CH_4 Emission Rate from the AFO

With the CH_4 concentration measured in the field campaign, we estimated CH_4 emission rates from the AFO using the mass balance method with meteorological conditions such as surface air temperature, pressure, wind speed, and wind direction recorded at each sampling time. The CH_4 emissions varied significantly over the four days of observations, as illustrated in Figure 5.4 and summarized in Table 5.1.

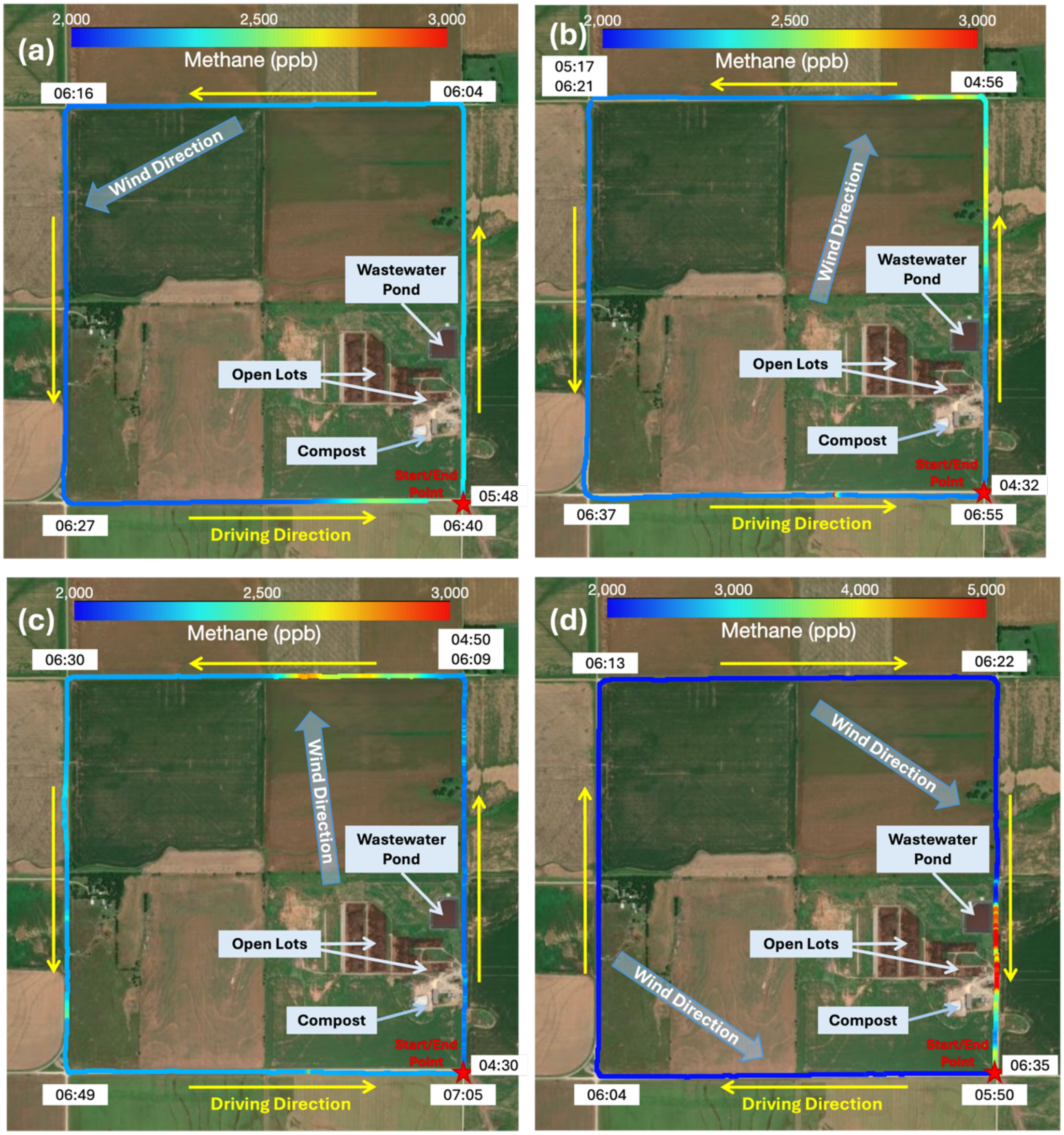

Figure 5.4 CH_4 concentrations measured during the field campaign at the AFO on four different mornings: (a) June 23 05:48 – 06:40, (b) June 24 04:32 – 06:55, (c) June 25 04:30 – 07:05, and (d) June 26, 2024 05:50 – 06:35. The satellite image shows the AFO layout, including open lots, a wastewater pond, and a compost area. The color scale represents CH_4 concentrations. Blue arrows show the mean wind direction during the measurement. The yellow arrows denote the driving direction, which was counterclockwise on June 23, 24, and 25, and clockwise on June 26. The marked local times indicate the time we arrived at the corner. The red star marks the start and end point of the driving route, located at the bottom right corner of each panel.

The CH_4 emission rate estimates ranged from 227 $kg{\cdot}hr^{-1}$ on June 24 to 1,147 $kg{\cdot}hr^{-1}$ on June 26. The first three days of measurements showed more moderate emission rates between 200 and 400 kg·hr^{-1}. However, on June 26, a strong CH_4 enhancement exceeding 6,000 ppb was recorded downwind of the AFO between 06:29 and 06:35, resulting in an estimated emission rate of 1,147 kg·hr^{-1}. This substantial increase is likely linked to the rainfall event on the evening of June 25, where rain rates reached 8.1 mm·hr^{-1} between 20:29 and 21:02.

Table 5.1 Summary of CH_4 emission rates estimated using the mass balance method (as described in Section 5.2.4.2) and the corresponding weather conditions observed during the field campaigns from June 23 to 26, 2024. Weather conditions, including wind speed, wind direction, temperature, surface pressure, and rainfall are from SGP surface meteorological station with mean and standard deviation in brackets during the measurement time. PBLH is estimated from the balloon-borne soundings at the nose of LLJ.

Measurement Date and Time	CH_4 Emission Rate	Weather Conditions					
		Wind Speed	Wind Direction	Temperature	Surface Pressure	PBLH	Rainfall
	kg·hr^{-1}	m·s^{-1}	degrees	°C	hPa	m	None
June 23 05:48 – 06:40	227	2.3 (0.56)	61.9 (104.2)	24.4 (0.23)	975.9 (0.086)	189	None
June 24 04:35 – 06:55	202	4.2 (0.44)	196.1 (2.7)	26.9 (0.22)	974.4 (0.170)	185	None
June 25 04:30 – 07:05	354	3.6 (1.21)	173.3 (17.9)	24.7 (0.21)	973.8 (0.346)	558	Evening heavy rain (4.45 mm from 20:29 to 21:02, 8.1 mm·hr^{-1} on average)
June 26 05:50 – 06:34	1147	2.4 (0.24)	289.5 (24.2)	25.5 (0.34)	972.5 (0.167)	334	None

Previous studies suggest that rainfall can significantly increase CH_4 emissions from manure ponds and feedlots. VanderZaag et al. (2010b) noted that CH_4 flux trends from liquid manure in tanks can rise due to two main components: baseline fluxes due to diffusion and intermittent bursts due to bubble flux (ebullition). Baseline fluxes are strongly correlated to, as microbial fermentation and methanogenesis are temperature-dependent (Cárdenas et al. 2021; Dalby et al. 2021; Mazzetto et al. 2014; Rennie et al. 2018; VanderZaag et al. 2010b). Given the temperature on June 26 is not the highest in these four days, we infer temperature is not the reason to explain the high CH_4 emission rate on June 26. Rainfall-induced ebullition and surface disturbance can generate spikes in CH_4 emissions (Baldé et al. 2016; Minato et al. 2013; VanderZaag et al. 2010a). Kaharabata and Schuepp (1998) reported that rainy days frequently resulted in CH_4 concentration increases by factors of 1.2 to 4. Similarly, Minato et al. (2013) found that CH_4 emissions from stored cattle manure ponds surged to over four times the baseline during heavy rain and remained elevated for up to eight hours post-rainfall. Even the CH_4 emission rapidly decrease when the heavy rain stopped, the CH_4 emission is still 2 to 3 times of the rate before the rainfall in the following 8 hours. Rainfalls are also related to CH_4 emission increase probably from the manure on corral surfaces by creating anaerobic conditions that enhanced microbial fermentation of manure organic matter(Todd et al. 2014) under more humid condition because of rainfall (Miller and Berry 2005).

Based on the CH_4 enhancements downwind of the AFO, we estimate that the wastewater pond emitted approximately 421 $kg{\cdot}hr^{-1}$ and the feedlot emitted around 406 $kg{\cdot}hr^{-1}$. This estimate assumes that the two observed CH_4 peaks between 06:22 and 06:35 (figure 5.4d) correspond to these two sources respectively – the north peak is related to the wastewater pond and the south is related to the feed lots. Given the proximity of the driving route to the AFO (110 meters from the center of the wastewater pond and 240 meters from the feedlot boundary), it's possible that CH_4 did not disperse uniformly throughout the PBL, based on a PBLH of 334 meters. If the CH_4 emissions from these sources only reached up to 100 meters, the total emission rate from the AFO would still be around 751 $kg{\cdot}hr^{-1}$.

In summary, CH_4 emissions from the entire AFO were likely greater than 300 kg·hr^{-1} during the early morning field campaign conducted in June 2024. Rainfall events can significantly increase CH_4 emission rates, potentially elevating them to 2-3 times the levels observed on dry days. In the next section, we will validate the WRF-GHG model simulations with our field campaign data to further assess CH_4 dispersion and its impact on regional air quality.

5.3.3 WRF-GHG Validation with Field Measurement

WRF-GHG simulations confirm the wastewater pond as a significant CH_4 source. We used the WRF-GHG model to simulate CH_4 dispersion from the AFO's wastewater pond, assuming an emission rate of 100 kg·hr^{-1}. The model simulated wind patterns from June 24, 2024, between 04:55 and 05:30 closely matched the wind speed (4.2 m/s) and direction (196 degrees) observed at the SGP surface meteorological station. The simulation predicted a northeastward plume dispersion, consistent with our field measurements, where we found high CH_4 concentrations exceeding 2400 ppb at the northeast corner of the AFO. This strong agreement between the WRF-GHG model and field measurements confirms the wastewater pond as a significant CH_4 source.

Field measurements captured CH_4 concentration peaks beyond the simulated plume, likely from the open lots. The WRF-GHG simulation of the CH_4 plume dispersing from the wastewater pond shows that the modeled plume primarily follows the wind direction toward the south-north drive route on the east side of the AFO (Figure 5.5). This aligns with field measurements that captured elevated CH_4 concentrations along this route. However, an additional CH_4 peak was observed during the field campaign when driving along the west-east route north of the AFO—something the WRF simulation does not fully capture if considering only the wastewater pond plume. Based on the simulated wind direction from WRF-GHG and corroborated by data from the SGP meteorological station, this additional peak is likely caused by CH_4 emissions from the open lots, rather than the wastewater pond. The position of the open lots upwind of the route supports this interpretation, emphasizing the importance of considering multiple emission sources within the AFO when analyzing CH_4 dispersion and concentration patterns in the region.

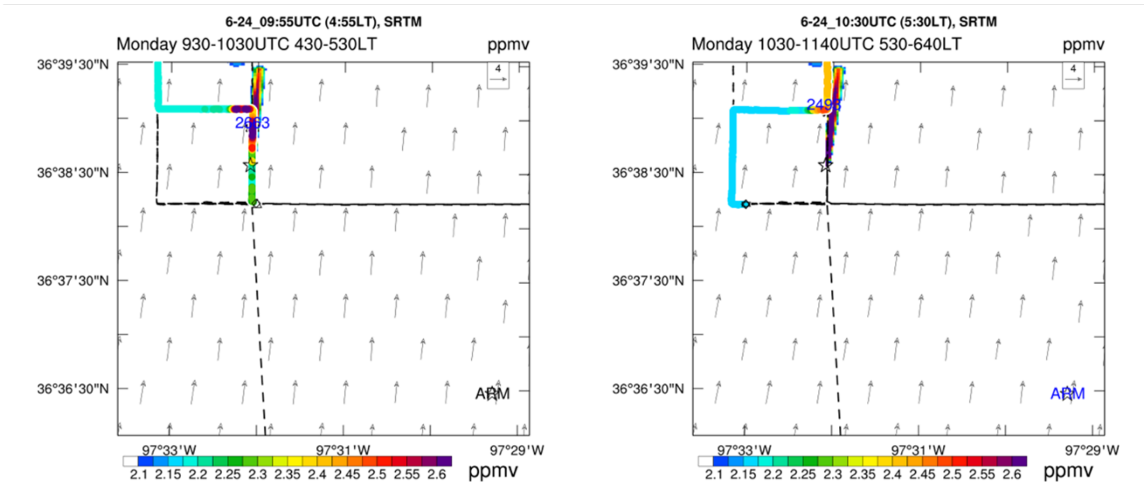

Figure 5.5 WRF-GHG simulations showing wind speed, direction, and CH_4 dispersion from the point source located at the wastewater pond (indicated by the plume) at two time intervals: 09:55 to 10:30 UTC (4:55 to 5:30 AM local time) on the left and 10:30 to 11:00 UTC (5:30 to 6:00 AM local time) on the right. The wind field is represented by arrows, and the CH_4 concentrations are indicated by the color scale. Overlaid on the simulation are the field measurement data from the early morning campaign on June 24. The location of the ARM site is also marked on the map with "ARM". Simulated and plotted by Xiao-Ming Hu.

This case demonstrates that WRF-GHG simulations reliably represent CH_4 dispersion from the AFO. The model effectively captured the CH_4 dispersion from the wastewater pond, closely aligning with the measured CH_4 concentrations during our field campaign. This supports the reliability of WRF-GHG in simulating CH_4 emissions from agricultural sources like AFOs.

In the next section, we will explore how CH_4 disperses under stable PBL conditions and evaluate how the AFO emissions impact CH_4 concentrations at SGP, located 5.8 km southeast of the AFO. This analysis will help us understand how local emissions contribute to observed CH_4

enhancements at the SGP site, especially during stable atmospheric conditions when vertical mixing is limited.

5.4 Conclusion

Our study at the Southern Great Plains (SGP) ARM site has uncovered important insights into the relationship between local CH_4 emissions and their impact on regional CH_4 concentrations. Throughout our previous investigation, we found that the SGP site consistently exhibited higher surface CH_4 levels compared to other sites across the U.S., with sharp nocturnal increases and substantial diurnal and seasonal variations. These patterns could not be fully explained by current CH_4 inventories, such as the EPA Greenhouse Gas Inventory (GHGI), highlighting the limitations of existing models to capture localized emissions.

Through the WRF-GHG simulations, we validated that the AFO is a significant local CH_4 source. Our mass balance estimates showed that the emission rate from the AFO ranged between 227 $kg \cdot hr^{-1}$ and 1147 $kg \cdot hr^{-1}$ during the four-day field campaign, with a substantial spike following a rainfall event on June 25, 2024. This surge in emissions, likely driven by increased microbial fermentation in the manure, underscores the complex interplay between local emissions and meteorological conditions. The comparison between modeled and observed CH_4 concentrations highlighted the possibility of larger emissions than what was initially assumed in the simulation (100 $kg \cdot hr^{-1}$), suggesting that current inventories may underestimate emissions from such sources.

Furthermore, the spatial distribution of CH_4 concentrations captured during the field campaign pointed to multiple emission sources within the AFO, with both the wastewater pond and open lots contributing substantially to CH_4 levels. WRF-GHG simulations indicated that while the modeled dispersion from the wastewater pond closely matched the field observations on the east-side drive route, additional CH_4 peaks observed on the west-east drive route were likely attributable to emissions from the open lots.

This study illustrates the importance of integrating field measurements with high-resolution modeling to improve emission inventories and refine CH_4 emission estimates. Our findings highlight the need for more accurate characterization of local emission sources, especially under various meteorological conditions, to better inform atmospheric models and climate policies. Future work should focus on refining the emission rates from such facilities and exploring the implications for regional and global CH_4 budgets, as well as improving the accuracy of predictive climate models.

Chapter 6 Summary

This dissertation investigates methane (CH_4) dynamics at the Southern Great Plains (SGP) Atmospheric Radiation Measurement (ARM) site through an integrated approach combining analysis of multi-year meteorological observations and CH_4 concentration profiles, targeted field campaigns, and atmospheric modeling that resulted in improved CH_4 emission source quantification. As a potent greenhouse gas, CH_4 plays a critical role in atmospheric chemistry and climate change. However, accurately quantifying its emissions remains a challenge due to the complex interplay between localized emissions and meteorological conditions. This dissertation provided new insights about strength and variability of emissions from agricultural operations and how land-atmosphere processes impact CH_4 concentrations which is important for improving CH_4 source quantifications.

To explore how land-atmosphere processes impact CH_4 at the SGP site, the first part of this research focuses on enhancing the understanding of land-atmosphere interactions by optimizing key parameters in the Noah-Multiparameterization Land Surface (Noah-MP) model. Using Bayesian optimization, the most sensitive land surface parameters were adjusted to improve the simulation of surface energy fluxes and atmospheric state variables. The optimized parameters led to improved accuracy in simulating energy fluxes (sensible and latent heat) and better representations of surface variables, such as soil moisture and temperature, particularly in the shallow topsoil layer. The results show that improving land-surface model performance has important implications for understanding land-atmosphere exchanges, especially in agriculturally dominated regions like the Southern Great Plains.

CH_4 dynamics at the SGP site were then analyzed, with long-term observations from 2017 to 2020 revealing consistently higher surface CH_4 concentrations compared to other U.S.

observational sites. These elevated levels of CH_4 showed pronounced diurnal and seasonal variations, with particularly sharp increases near the surface at nighttime. The study highlights the role of stable planetary boundary layer (PBL) conditions, with strong temperature inversions and shallow PBLs, in trapping CH_4 close to the surface. Localized emissions from concentrated animal feeding operations (AFOs), natural gas leaks, and open-range cattle were identified as key contributors to the CH_4 enhancements. A field campaign conducted in June 2024 provided further insights into the emissions from a large AFO located 5.8 km northwest of the SGP site. CH_4 emissions from the AFO, estimated using the mass balance method, ranged from 227 $kg \cdot hr^{-1}$ to 1147 $kg \cdot hr^{-1}$, with peak emissions following a rainfall event. The increase in emissions suggests that wet conditions significantly enhance microbial activity in manure ponds and open lots, leading to higher CH_4 releases.

To validate these findings, WRF-GHG s were employed to simulate CH_4 dispersion from the AFO, allowing for a direct comparison between the field measurements and the simulated results. The simulations captured the dispersion of CH_4 from the AFO, showing good agreement with field measurements. However, the simulated CH_4 enhancements at the SGP site were lower than observed with emission from the wastewater pond only. This discrepancy points to a potential underestimation of actual AFO emissions in the model. As a result, it highlights the importance of refining CH_4 emission inventories to account for localized sources and meteorological conditions, which are crucial for improving the accuracy of climate models and formulating effective mitigation strategies.

In summary, this research emphasizes the significance of accurately quantifying CH_4 emissions from agricultural and industrial sources, especially in regions with complex meteorological conditions. By integrating field measurements and atmospheric modeling, this study provides valuable insights into the regional and global implications of CH_4 emissions, contributing to more reliable predictions of the role of CH_4 in climate change.

Chapter 7 Future Works

Building on the insights and experience gained from our field campaign at the Southern Great Plains (SGP) site, we can envision several promising directions for future research. Our investigation of CH_4 emissions from agricultural sources, particularly the concentrated animal feeding operations (AFOs), has provided valuable data for improving CH_4 emission inventories. However, this work can be extended to explore CH_4 emissions from a broader array of urban and industrial sources.

Urban-Scale CH_4 Emission Quantification

One extension of our research would involve expanding our CH_4 measurement efforts to urban areas. CH_4 emissions in urban environments are quite difficult to quantify due to the complexity of potential sources, which range from small natural gas pipeline leaks and oil wells to large landfills and wastewater treatment plants. Based on our prior field campaign experience and the measurements we conducted at the City of Norman Wastewater Reclamation Facility, we have built the foundation for developing an approach that could address these challenges.

During our visit to the wastewater facility on August 1, 2024, we recorded significant CH_4 emissions from the sedimentation pond, where wastewater solids had accumulated for over 20 years. Measurements revealed CH_4 concentrations exceeding 10,000 ppb downwind of the pond (Figure 7.1). With southeast winds, the elevated CH_4 levels extended to the nearby road, including areas near the National Weather Center across Highway 9. These findings underscore the critical role of wastewater facilities in urban CH_4 inventories. Additionally, Norman City has numerous oil wells (Figure 7.2), which present another potential source of CH_4 leaks that should be included in future urban CH_4 inventories.

By integrating measurements from diverse CH_4 sources within urban settings, such as those found in Norman, we can enhance our ability to build a more accurate urban CH_4 inventory, which would be crucial for improving climate models and developing effective mitigation strategies.

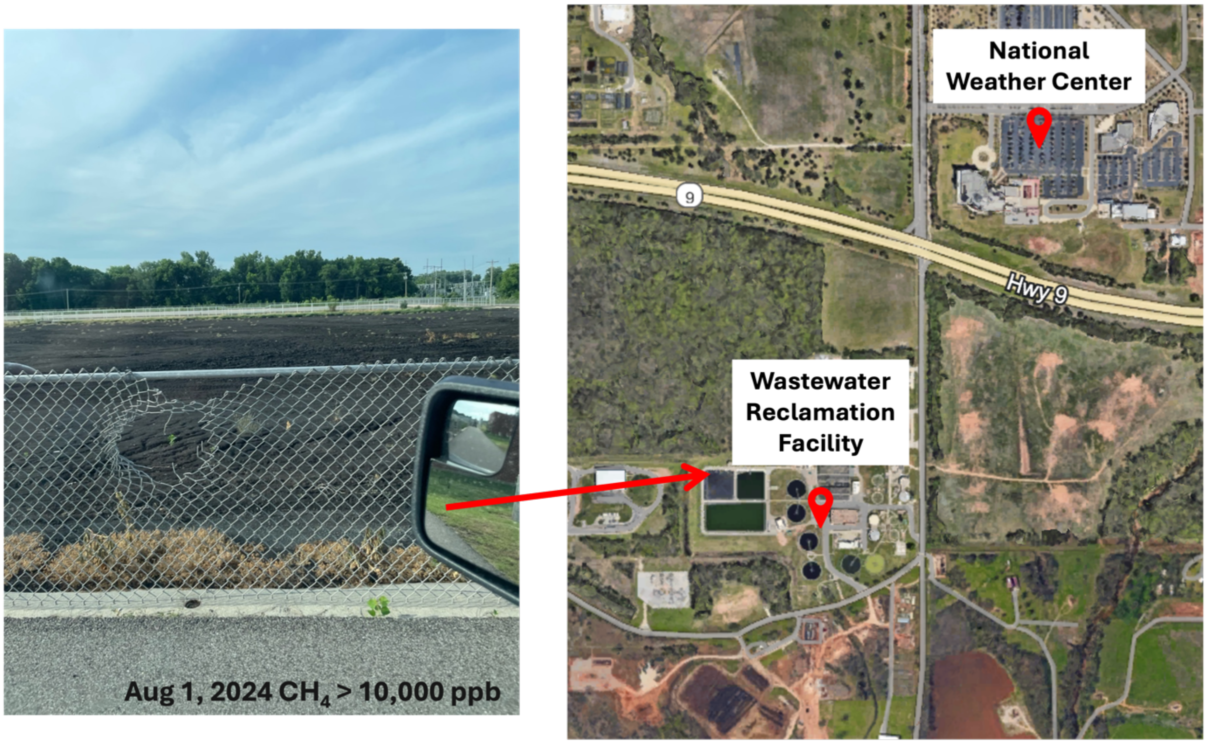

Figure 7.1 CH_4 Concentration measurement at the City of Norman Wastewater Reclamation Facility. The right panel shows the City of Norman Wastewater Reclamation Facility as seen from Google Earth, with the National Weather Center located just across Highway 9. The left panel captures the solid sedimentation pond at the facility, where methane concentrations exceeding 10,000 ppb were measured downwind of the pond on August 1, 2024.

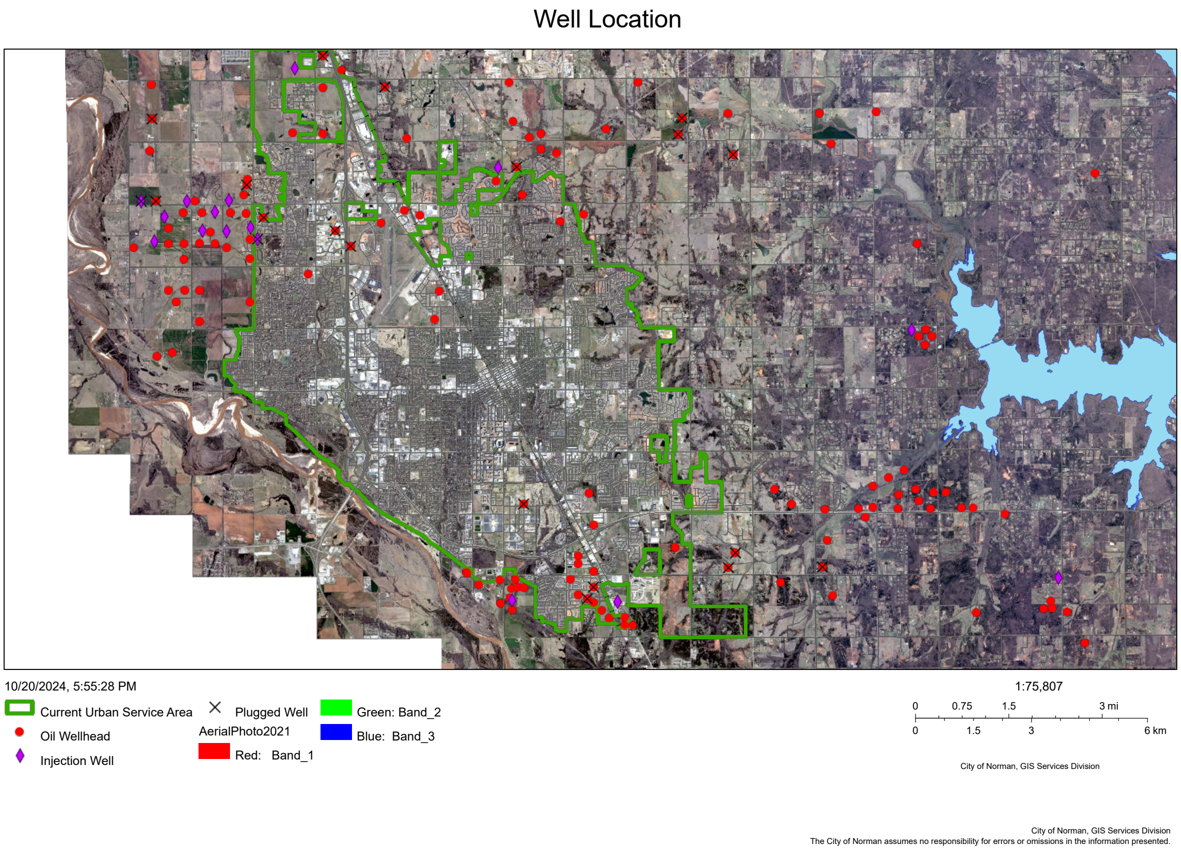

Figure 7.2: Oil well locations in the city of Norman, Oklahoma, highlighting different types of wells, including plugged wells (red X), oil wellheads (red dots), and injection wells (purple dots). The green outline indicates the current urban service area. Data source: City of Norman GIS Services Division, from https://www.normanok.gov/your-government/departments/planning-and-community-development/planning-and-zoning/oil-gas

Tools and Techniques for Urban CH_4 Inventories

The methodology we employed during the field campaign at SGP is adaptable for urban-scale studies, including the use of the LI-COR LI-7810 CH_4/CO_2/H_2O Trace Gas Analyzer, meteorological anemometers, and GPS. When coupled with the WRF-GHG, we can simulate CH_4 dispersion and better understand how emissions from local sources contribute to overall CH_4 concentrations in the atmosphere.

The equipment needed for urban-scale CH_4 quantification is relatively straightforward. With a portable trace gas analyzer like the LI-7810, a meteorological anemometer to record wind speed and direction, and GPS to track location, we can map CH_4 sources with precision. The addition of WRF-GHG simulations would allow us to model the transport and dispersion of CH_4 across the city, helping us identify hotspots and quantify the contribution of various CH_4 sources.

Building a Comprehensive Urban CH_4 Inventory

By collecting data from both small and large CH_4 sources—ranging from leaks in natural gas pipelines and emissions from oil wells to large emitters like landfills and wastewater treatment plants—we can build a more accurate and localized top-down urban CH_4 inventory. This would provide a more accurate CH_4 Inventory compared to traditional bottom-up CH_4 inventories like EPA GHGI.

In conclusion, our ability to extend the methodologies developed in this dissertation to an urban scale offers exciting opportunities for improving CH_4 emission inventories and enhancing our understanding of urban CH_4 dynamics. By leveraging portable instrumentation and advanced atmospheric models like WRF-GHG, we can develop more accurate and detailed CH_4 inventories that account for the complex landscape of urban emissions, paving the way for more effective mitigation strategies at both local and global scales.

References

Afchar, D., V. Nozick, J. Yamagishi, and I. Echizen, 2018: Mesonet: a compact facial video forgery detection network. *2018 IEEE international workshop on information forensics and security (WIFS)*, IEEE, 1-7.

Ahmadov, R., C. Gerbig, R. Kretschmer, S. Koerner, B. Neininger, A. Dolman, and C. Sarrat, 2007: Mesoscale covariance of transport and CO2 fluxes: Evidence from observations and simulations using the WRF‐VPRM coupled atmosphere‐biosphere model. *Journal of Geophysical Research: Atmospheres*, **112**.

Alvarez, R. A., and Coauthors, 2018: Assessment of methane emissions from the US oil and gas supply chain. *Science*, **361,** 186-188.

Andrews, T., 2009: Forcing and response in simulated 20th and 21st century surface energy and precipitation trends. *Journal of Geophysical Research: Atmospheres*, **114**.

Anenberg, S. C., and Coauthors, 2012: Global air quality and health co-benefits of mitigating near-term climate change through methane and black carbon emission controls. *Environmental health perspectives*, **120,** 831-839.

Arndt, C., and Coauthors, 2018: Short-term methane emissions from 2 dairy farms in California estimated by different measurement techniques and US Environmental Protection Agency inventory methodology: A case study. *Journal of dairy science*, **101,** 11461-11479.

Arsenault, K. R., G. S. Nearing, S. Wang, S. Yatheendradas, and C. D. Peters-Lidard, 2018: Parameter sensitivity of the Noah-MP land surface model with dynamic vegetation. *Journal of Hydrometeorology*, **19,** 815-830.

Balashov, N. V., K. J. Davis, N. L. Miles, T. Lauvaux, S. J. Richardson, Z. R. Barkley, and T. A. Bonin, 2020: Background heterogeneity and other uncertainties in estimating urban methane flux:

results from the Indianapolis Flux Experiment (INFLUX). *Atmospheric Chemistry and Physics*, **20,** 4545-4559.

Balcombe, P., K. Anderson, J. Speirs, N. Brandon, and A. Hawkes, 2017: The natural gas supply chain: the importance of methane and carbon dioxide emissions. *ACS Sustainable Chemistry & Engineering*, **5,** 3-20.

Baldé, H., A. C. VanderZaag, S. Burtt, L. Evans, C. Wagner-Riddle, R. L. Desjardins, and J. D. MacDonald, 2016: Measured versus modeled methane emissions from separated liquid dairy manure show large model underestimates. *Agriculture, ecosystems & environment*, **230,** 261-270.

Baldocchi, D., and Coauthors, 2001: FLUXNET: A new tool to study the temporal and spatial variability of ecosystem-scale carbon dioxide, water vapor, and energy flux densities. *Bulletin of the American Meteorological Society*, **82,** 2415-2434.

Ball, J. T., I. E. Woodrow, and J. A. Berry, 1987: A model predicting stomatal conductance and its contribution to the control of photosynthesis under different environmental conditions. *Progress in photosynthesis research*, Springer, 221-224.

Bamberger, I., J. Stieger, N. Buchmann, and W. Eugster, 2014: Spatial variability of methane: Attributing atmospheric concentrations to emissions. *Environmental Pollution*, **190,** 65-74.

Bannister, R. N., and C. Wilson, 2024: Inverse modelling for surface methane flux estimation with 4DVar: impact of a computationally efficient representation of a non-diagonal B-matrix in INVICAT v4. *EGUsphere*, **2024,** 1-34.

Banta, R. M., L. Mahrt, D. Vickers, J. Sun, B. B. Balsley, Y. L. Pichugina, and E. J. Williams, 2007: The very stable boundary layer on nights with weak low-level jets. *Journal of the Atmospheric Sciences*, **64,** 3068-3090.

Barros, A. P., and W. Hwu, 2002: A study of land‐atmosphere interactions during summertime rainfall using a mesoscale model. *Journal of Geophysical Research: Atmospheres*, **107,** ACL 17-11-ACL 17-18.

Basu, S., and Coauthors, 2022: Estimating emissions of methane consistent with atmospheric measurements of methane and δ 13 C of methane. *Atmospheric Chemistry and Physics*, **22,** 15351-15377.

Batchvarova, E., and S.-E. Gryning, 1991: Applied model for the growth of the daytime mixed layer. *Boundary-Layer Meteorology*, **56,** 261-274.

Bateni, S., and D. Entekhabi, 2012: Relative efficiency of land surface energy balance components. *Water Resources Research*, **48**.

Beck, V., and Coauthors, 2013: WRF-Chem simulations in the Amazon region during wet and dry season transitions: evaluation of methane models and wetland inundation maps. *Atmospheric Chemistry and Physics*, **13,** 7961-7982.

Berg, L. K., L. D. Riihimaki, Y. Qian, H. Yan, and M. Huang, 2015: The low-level jet over the southern Great Plains determined from observations and reanalyses and its impact on moisture transport. *Journal of Climate*, **28,** 6682-6706.

Beringer, J., and N. Tapper, 2002: Surface energy exchanges and interactions with thunderstorms during the Maritime Continent Thunderstorm Experiment (MCTEX). *Journal of Geophysical Research: Atmospheres*, **107,** AAC 3-1-AAC 3-13.

Betts, A. K., 2009: Land‐surface‐atmosphere coupling in observations and models. *Journal of Advances in Modeling Earth Systems*, **1**.

Betts, A. K., J. H. Ball, A. C. Beljaars, M. J. Miller, and P. A. Viterbo, 1996: The land surface‐atmosphere interaction: A review based on observational and global modeling perspectives. *Journal of Geophysical Research: Atmospheres*, **101,** 7209-7225.

Betts, R., 2007: Implications of land ecosystem-atmosphere interactions for strategies for climate change adaptation and mitigation. *Tellus B: Chemical and Physical Meteorology*, **59,** 602-615.

Bhardwaj, P., R. Kumar, D. A. Mitchell, C. A. Randles, N. Downey, D. Blewitt, and B. Kosovic, 2022: Evaluating the detectability of methane point sources from satellite observing systems using microscale modeling. *Scientific Reports*, **12,** 17425.

Biraud, S., M. Fischer, S. Chan, and M. Torn, 2023: AmeriFlux AmeriFlux US-ARM ARM Southern Great Plains site-Lamont. Lawrence Berkeley National Lab.(LBNL), Berkeley, CA (United States). AmeriFlux.

Bjorneberg, D. L., A. B. Leytem, D. Westermann, P. Griffiths, L. Shao, and M. Pollard, 2009: Measurement of atmospheric ammonia, methane, and nitrous oxide at a concentrated dairy production facility in southern Idaho using open-path FTIR spectrometry. *Transactions of the ASABE*, **52,** 1749-1756.

Blackadar, A. K., 1957: Boundary layer wind maxima and their significance for the growth of nocturnal inversions. *Bulletin of the American Meteorological Society*, **38,** 283-290.

Bleeker, W., and M. Andre, 1951: On the diurnal variation of precipitation, particularly over central USA, and its relation to large‐scale orographic circulation systems. *Quarterly Journal of the Royal Meteorological Society*, **77,** 260-271.

Bloom, A. A., and Coauthors, 2017: A global wetland methane emissions and uncertainty dataset for atmospheric chemical transport models (WetCHARTs version 1.0). *Geoscientific Model Development*, **10,** 2141-2156.

Blyth, E. M., and Coauthors, 2021: Advances in land surface modelling. *Current Climate Change Reports*, **7,** 45-71.

Boeckx, P., O. Van Cleemput, and I. Villaralvo, 1996: Methane emission from a landfill and the methane oxidising capacity of its covering soil. *Soil Biology and Biochemistry*, **28,** 1397-1405.

Boer, G., 1993: Climate change and the regulation of the surface moisture and energy budgets. *Climate Dynamics*, **8,** 225-239.

Bogner, J., and K. Spokas, 1993: Landfill CH4: rates, fates, and role in global carbon cycle. *Chemosphere*, **26,** 369-386.

Bonan, G. B., 2008: Forests and climate change: forcings, feedbacks, and the climate benefits of forests. *science*, **320,** 1444-1449.

Bonner, W. D., and J. Paegle, 1970: Diurnal variations in boundary layer winds over the south-central United States in summer. *Monthly Weather Review*, **98,** 735-744.

Boryan, C., Z. Yang, R. Mueller, and M. Craig, 2011: Monitoring US agriculture: the US department of agriculture, national agricultural statistics service, cropland data layer program. *Geocarto International*, **26,** 341-358.

Boucher, O., P. Friedlingstein, B. Collins, and K. P. Shine, 2009: The indirect global warming potential and global temperature change potential due to methane oxidation. *Environmental Research Letters*, **4,** 044007.

Bousquet, P., and Coauthors, 2011: Source attribution of the changes in atmospheric methane for 2006–2008. *Atmospheric Chemistry and Physics*, **11,** 3689-3700.

Bridgham, S. D., H. Cadillo‐Quiroz, J. K. Keller, and Q. Zhuang, 2013: Methane emissions from wetlands: biogeochemical, microbial, and modeling perspectives from local to global scales. *Global change biology*, **19,** 1325-1346.

Brubaker, K. L., and D. Entekhabi, 1996: Analysis of feedback mechanisms in land - atmosphere interaction. *Water Resources Research*, **32,** 1343-1357.

Brutsaert, W., 1982: *Evaporation into the atmosphere: theory, history and applications.* Vol. 1, Springer Science & Business Media.

Cai, Z., Y. Shan, and H. Xu, 2007: Effects of nitrogen fertilization on CH4 emissions from rice fields. *Soil Science and Plant Nutrition*, **53,** 353-361.

Callewaert, S., and Coauthors, 2022: Analysis of CO 2, CH 4, and CO surface and column concentrations observed at Réunion Island by assessing WRF-Chem simulations. *Atmospheric Chemistry and Physics*, **22,** 7763-7792.

Campioli, M., and Coauthors, 2015: Biomass production efficiency controlled by management in temperate and boreal ecosystems. *Nature Geoscience*, **8,** 843-846.

Cárdenas, A., and Coauthors, 2021: Methane emissions from the storage of liquid dairy manure: Influences of season, temperature and storage duration. *Waste Management*, **121,** 393-402.

Caulton, D. R., and Coauthors, 2014: Toward a better understanding and quantification of methane emissions from shale gas development. *Proceedings of the National Academy of Sciences*, **111,** 6237-6242.

Chan, A., and T. Parkin, 2001: Effect of land use on methane flux from soil. *Journal of Environmental Quality*, **30,** 786-797.

Chan, E., D. E. Worthy, D. Chan, M. Ishizawa, M. D. Moran, A. Delcloo, and F. Vogel, 2020: Eight-year estimates of methane emissions from oil and gas operations in Western Canada are nearly twice those reported in inventories. *Environmental Science & Technology*, **54,** 14899-14909.

Chandra, N., and Coauthors, 2021: Emissions from the oil and gas sectors, coal mining and ruminant farming drive methane growth over the past three decades. *Journal of the Meteorological Society of Japan. Ser. II*, **99,** 309-337.

Chang, J., S. Peng, Y. Yin, P. Ciais, P. Havlik, and M. Herrero, 2021: The key role of production efficiency changes in livestock methane emission mitigation, AGU Advances, 2, e2021AV000391.

Chehbouni, A., and Coauthors, 2000: Estimation of heat and momentum fluxes over complex terrain using a large aperture scintillometer. *Agricultural and forest meteorology*, **105,** 215-226.

Chelton, D. B., and S.-P. Xie, 2010: Coupled ocean-atmosphere interaction at oceanic mesoscales. *Oceanography*, **23,** 52-69.

Chen, F., and Coauthors, 1996: Modeling of land surface evaporation by four schemes and comparison with FIFE observations. *Journal of Geophysical Research: Atmospheres*, **101,** 7251-7268.

Chen, Y., and Coauthors, 2022: Quantifying regional methane emissions in the New Mexico Permian Basin with a comprehensive aerial survey. *Environmental science & technology*, **56,** 4317-4323.

Christensen, T. R., and Coauthors, 2003: Factors controlling large scale variations in methane emissions from wetlands. *Geophysical Research Letters*, **30**.

Chu, H., and Coauthors, 2021: Representativeness of Eddy-Covariance flux footprints for areas surrounding AmeriFlux sites. *Agricultural and Forest Meteorology*, **301,** 108350.

Clark, M. P., D. Kavetski, and F. Fenicia, 2011: Pursuing the method of multiple working hypotheses for hydrological modeling. *Water Resources Research*, **47**.

Clark, M. P., and Coauthors, 2015: Improving the representation of hydrologic processes in Earth System Models. *Water Resources Research*, **51,** 5929-5956.

Collatz, G. J., J. T. Ball, C. Grivet, and J. A. Berry, 1991: Physiological and environmental regulation of stomatal conductance, photosynthesis and transpiration: a model that includes a laminar boundary layer. *Agricultural and Forest meteorology*, **54,** 107-136.

Collins, W., and Coauthors, 2006: Radiative forcing by well‐mixed greenhouse gases: Estimates from climate models in the Intergovernmental Panel on Climate Change (IPCC) Fourth Assessment Report (AR4). *Journal of Geophysical Research: Atmospheres*, **111**.

Conley, S., and Coauthors, 2017: Application of Gauss's theorem to quantify localized surface emissions from airborne measurements of wind and trace gases. *Atmospheric Measurement Techniques*, **10,** 3345-3358.

Cuntz, M., and Coauthors, 2016: The impact of standard and hard‐coded parameters on the hydrologic fluxes in the Noah‐MP land surface model. *Journal of Geophysical Research: Atmospheres*, **121,** 10,676-610,700.

Cusworth, D. H., and Coauthors, 2021a: Intermittency of large methane emitters in the Permian Basin. *Environmental Science & Technology Letters*, **8,** 567-573.

Cusworth, D. H., and Coauthors, 2021b: A Bayesian framework for deriving sector-based methane emissions from top-down fluxes. *Communications Earth & Environment*, **2,** 242.

Dalby, F. R., and Coauthors, 2021: Understanding methane emission from stored animal manure: A review to guide model development. *Journal of Environmental Quality*, **50,** 817-835.

Dangal, S. R., H. Tian, B. Zhang, S. Pan, C. Lu, and J. Yang, 2017: Methane emission from global livestock sector during 1890–2014: Magnitude, trends and spatiotemporal patterns. *Global Change Biology*, **23,** 4147-4161.

Deardorff, J. W., 1978: Efficient prediction of ground surface temperature and moisture, with inclusion of a layer of vegetation. *Journal of Geophysical Research: Oceans*, **83,** 1889-1903.

Dee, D. P., and Coauthors, 2011: The ERA‐Interim reanalysis: Configuration and performance of the data assimilation system. *Quarterly Journal of the royal meteorological society*, **137,** 553-597.

Delwiche, K. B., and Coauthors, 2021: FLUXNET-CH4: A global, multi-ecosystem dataset and analysis of methane seasonality from freshwater wetlands. *Earth System Science Data Discussions*, **2021,** 1-111.

Dentener, F., and Coauthors, 2005: The impact of air pollutant and methane emission controls on tropospheric ozone and radiative forcing: CTM calculations for the period 1990-2030. *Atmospheric Chemistry and Physics*, **5,** 1731-1755.

Desai, A., 2024: AmeriFlux BASE US‐PFa Park falls/WLEF. *AmeriFlux AMP*, 28-5 ed.

Dickinson, R. E., 1983: Land surface processes and climate—Surface albedos and energy balance. *Advances in geophysics*, Elsevier, 305-353.

——, 1984: Modeling evapotranspiration for three‐dimensional global climate models. *Climate processes and climate sensitivity*, **29,** 58-72.

——, 1995: Land‐atmosphere interaction. *Reviews of geophysics*, **33,** 917-922.

Dickinson, R. E., M. Shaikh, R. Bryant, and L. Graumlich, 1998: Interactive canopies for a climate model. *Journal of Climate*, **11,** 2823-2836.

Diessner, M., J. O'Connor, A. Wynn, S. Laizet, Y. Guan, K. Wilson, and R. D. Whalley, 2022: Investigating Bayesian optimization for expensive-to-evaluate black box functions: Application in fluid dynamics. *Frontiers in Applied Mathematics and Statistics*, **8,** 1076296.

Diwekar, U. M., and J. R. Kalagnanam, 1997: Efficient sampling technique for optimization under uncertainty. *AIChE Journal*, **43,** 440-447.

Dlugokencky, E. J., and Coauthors, 2009: Observational constraints on recent increases in the atmospheric CH4 burden. *Geophysical Research Letters*, **36**.

Dong, X., M. Yue, Y. Jiang, X.-M. Hu, Q. Ma, J. Pu, and G. Zhou, 2021: Analysis of CO 2 spatio-temporal variations in China using a weather–biosphere online coupled model. *Atmospheric Chemistry and Physics*, **21,** 7217-7233.

Driedonks, A., and H. Tennekes, 1984: Entrainment effects in the well-mixed atmospheric boundary layer. *Boundary-Layer Meteorology*, **30,** 75-105.

Duan, Q., and Coauthors, 2006: Model Parameter Estimation Experiment (MOPEX): An overview of science strategy and major results from the second and third workshops. *Journal of Hydrology*, **320,** 3-17.

Dudhia, J., 1989: Numerical study of convection observed during the winter monsoon experiment using a mesoscale two-dimensional model. *Journal of Atmospheric Sciences*, **46,** 3077-3107.

Duren, R. M., and Coauthors, 2019: California's methane super-emitters. *Nature*, **575,** 180-184.

Erland, B. M., A. K. Thorpe, and J. A. Gamon, 2022: Recent advances toward transparent methane emissions monitoring: a review. *Environmental Science & Technology*, **56,** 16567-16581.

Esau, I., and S. Zilitinkevich, 2010: On the role of the planetary boundary layer depth in the climate system. *Advances in Science and Research*, **4,** 63-69.

Etminan, M., G. Myhre, E. J. Highwood, and K. P. Shine, 2016: Radiative forcing of carbon dioxide, methane, and nitrous oxide: A significant revision of the methane radiative forcing. *Geophysical Research Letters*, **43,** 12,614-612,623.

facility, A. R. M. A. u., 2010a: Doppler Lidar Horizontal Wind Profiles (DLPROFWIND4NEWS). 2010-11-02 to 2024-04-25, Southern Great Plains (SGP) Central Facility, Lamont, OK (C1). Compiled by T. Shippert, R. Newsom, L. Riihimaki and D. Zhang.

——, 2010b: Doppler Lidar Wind Statistics Profiles (DLPROFWSTATS4NEWS). 2010-10-22 to 2023-10-23, Southern Great Plains (SGP) Central Facility, Lamont, OK (C1). Compiled by T. Shippert, R. Newsom, L. Riihimaki and D. Zhang.

Fang, Z., H. Bogena, S. Kollet, and H. Vereecken, 2016: Scale dependent parameterization of soil hydraulic conductivity in 3D simulation of hydrological processes in a forested headwater catchment. *Journal of hydrology*, **536,** 365-375.

Ferguson, C. R., 2022: Changes in Great Plains Low‐Level Jet Structure and Associated Precipitation Over the 20th Century. *Journal of Geophysical Research: Atmospheres*, **127,** e2021JD035859.

Findell, K., P. Gentine, B. R. Lintner, and C. Kerr, 2011: Probability of afternoon precipitation in eastern United States and Mexico enhanced by high evaporation. *Nat. Geosci.*, **4,** 434-439.

Fiore, A. M., D. J. Jacob, B. D. Field, D. G. Streets, S. D. Fernandes, and C. Jang, 2002: Linking ozone pollution and climate change: The case for controlling methane. *Geophysical Research Letters*, **29,** 25-21-25-24.

Fisher, J. B., K. P. Tu, and D. D. Baldocchi, 2008: Global estimates of the land–atmosphere water flux based on monthly AVHRR and ISLSCP-II data, validated at 16 FLUXNET sites. *Remote Sensing of Environment*, **112,** 901-919.

Fisher, R. A., and C. D. Koven, 2020: Perspectives on the future of land surface models and the challenges of representing complex terrestrial systems. *Journal of Advances in Modeling Earth Systems*, **12,** e2018MS001453.

Foken, T., 2008: The energy balance closure problem: An overview. *Ecological Applications*, **18,** 1351-1367.

Fooladmand, H., 2007: Measurement of soil specific surface area and its relation to some soil physico-chemical properties, Ph. D. Thesis. Department of Irrigation. Science and Research Unit of ….

Forster, P., and Coauthors, 2007: Changes in atmospheric constituents and in radiative forcing. Chapter 2.

Frankenberg, C., J. Meirink, M. van Weele, U. Platt, and T. Wagner, 2005: Assessing methane emissions from global space-borne observations. *Science*, **308,** 1010-1014.

Frazier, P. I., 2018: A tutorial on Bayesian optimization. *arXiv preprint arXiv:1807.02811*.

Fritschen, L. J., and J. R. Simpson, 1989: Surface energy and radiation balance systems: General description and improvements. *Journal of Applied Meteorology and Climatology*, **28,** 680-689.

Galle, B., J. Samuelsson, B. H. Svensson, and G. Börjesson, 2001: Measurements of methane emissions from landfills using a time correlation tracer method based on FTIR absorption spectroscopy. *Environmental Science & Technology*, **35,** 21-25.

Galperin, B., S. Sukoriansky, and P. S. Anderson, 2007: On the critical Richardson number in stably stratified turbulence. *Atmospheric Science Letters*, **8,** 65-69.

Gao, J., C. Guan, and B. Zhang, 2022: Why are methane emissions from China's oil & natural gas systems still unclear? A review of current bottom-up inventories. *Science of The Total Environment*, **807,** 151076.

Garratt, J. R., 1994: The atmospheric boundary layer. *Earth-Science Reviews*, **37,** 89-134.

Garrigues, S., and Coauthors, 2018: Impacts of the soil water transfer parameterization on the simulation of evapotranspiration over a 14-year Mediterranean crop succession. *Journal of Hydrometeorology*, **19,** 3-25.

GaŽovic, M., L. Kutzbach, P. Schreiber, C. Wille, and M. Wilmking, 2010: Diurnal dynamics of CH4 from a boreal peatland during snowmelt. *Tellus B: Chemical and Physical Meteorology*, **62,** 133-139.

Gebler, S., H.-J. Hendricks Franssen, T. Pütz, H. Post, M. Schmidt, and H. Vereecken, 2015: Actual evapotranspiration and precipitation measured by lysimeters: a comparison with eddy covariance and tipping bucket. *Hydrology and earth system sciences*, **19,** 2145-2161.

Gelaro, R., and Coauthors, 2017: The modern-era retrospective analysis for research and applications, version 2 (MERRA-2). *Journal of Climate*, **30,** 5419-5454.

Gerber, P., and Coauthors, 2013: Technical options for the mitigation of direct methane and nitrous oxide emissions from livestock: a review. *animal*, **7,** 220-234.

Ghanbarian-Alavijeh, B., and H. Millán, 2009: The relationship between surface fractal dimension and soil water content at permanent wilting point. *Geoderma*, **151,** 224-232.

Global, 2015: MERRA‐2 inst3_3d_asm_Np: 3d, 3‐hourly, instantaneous, pressure‐level, assimilation, assimilated meteorological fields V5.12.4.

Goss, M. J., and W. Ehlers, 2009: The role of lysimeters in the development of our understanding of soil water and nutrient dynamics in ecosystems. *Soil Use and Management*, **25,** 213-223.

Grachev, A. A., E. L. Andreas, C. W. Fairall, P. S. Guest, and P. O. G. Persson, 2013: The critical Richardson number and limits of applicability of local similarity theory in the stable boundary layer. *Boundary-layer meteorology*, **147,** 51-82.

Haines, A., and Coauthors, 2009: Public health benefits of strategies to reduce greenhouse-gas emissions: overview and implications for policy makers. *The lancet*, **374,** 2104-2114.

Hamilton, S. W., E. J. DePeters, J. A. McGarvey, J. Lathrop, and F. M. Mitloehner, 2010: Greenhouse gas, animal performance, and bacterial population structure responses to dietary monensin fed to dairy cows. *Journal of environmental quality*, **39,** 106-114.

Hassan, A. E., H. M. Bekhit, and J. B. Chapman, 2009: Using Markov Chain Monte Carlo to quantify parameter uncertainty and its effect on predictions of a groundwater flow model. *Environmental Modelling & Software*, **24,** 749-763.

He, C., and Coauthors, 2021: Interactions between air pollution and terrestrial ecosystems: Perspectives on challenges and future directions. *Bulletin of the American Meteorological Society*, **102,** E525-E538.

He, J., K. Yang, W. Tang, H. Lu, J. Qin, Y. Chen, and X. Li, 2020: The first high-resolution meteorological forcing dataset for land process studies over China. *Scientific Data*, **7,** 1-11.

He, Q., H. Lu, and K. Yang, 2023: Soil moisture memory of land surface models utilized in major reanalyses differ significantly from SMAP observation. *Earth's Future*, **11,** e2022EF003215.

Head, T., M. Kumar, H. Nahrstaedt, G. Louppe, and I. Shcherbatyi, 2021: scikit-optimize.

Heilig, G. K., 1994: The greenhouse gas methane (CH4): Sources and sinks, the impact of population growth, possible interventions. *Population and environment*, **16,** 109-137.

Helbig, M., and Coauthors, 2021: Integrating continuous atmospheric boundary layer and tower-based flux measurements to advance understanding of land-atmosphere interactions. *Agricultural and Forest Meteorology*, **307,** 108509.

Hemakumara, H., L. Chandrapala, and A. F. Moene, 2003: Evapotranspiration fluxes over mixed vegetation areas measured from large aperture scintillometer. *Agricultural water management*, **58,** 109-122.

Hersbach, H., and Coauthors, 2018: ERA5 hourly data on pressure levels from 1979 to present. *Copernicus climate change service (c3s) climate data store (cds)*, **10**.

Hillel, D., 2013: *Introduction to soil physics.* Academic press.

Hmiel, B., and Coauthors, 2020: Preindustrial 14CH4 indicates greater anthropogenic fossil CH4 emissions. *Nature*, **578,** 409-412.

Hoesly, R. M., and Coauthors, 2018: Historical (1750–2014) anthropogenic emissions of reactive gases and aerosols from the Community Emissions Data System (CEDS). *Geoscientific Model Development*, **11,** 369-408.

Hogan, K. B., and J. S. Hoffman, 1991: Methane on the greenhouse agenda. *Nature*, **354**.

Holtslag, A., and Coauthors, 2013: Stable atmospheric boundary layers and diurnal cycles: challenges for weather and climate models. *Bulletin of the American Meteorological Society*, **94,** 1691-1706.

Hong, S.-Y., Y. Noh, and J. Dudhia, 2006: A new vertical diffusion package with an explicit treatment of entrainment processes. *Monthly weather review*, **134,** 2318-2341.

Hristov, A. N., and Coauthors, 2017: Discrepancies and uncertainties in bottom-up gridded inventories of livestock methane emissions for the contiguous United States. *Environmental science & technology*, **51,** 13668-13677.

Hristov, A. N., and Coauthors, 2018: Symposium review: Uncertainties in enteric methane inventories, measurement techniques, and prediction models. *Journal of dairy science*, **101,** 6655-6674.

Hu, X.-M., J. W. Nielsen-Gammon, and F. Zhang, 2010: Evaluation of three planetary boundary layer schemes in the WRF model. *Journal of Applied Meteorology and Climatology*, **49,** 1831-1844.

Hu, X.-M., and Coauthors, 2013: Impact of the vertical mixing induced by low-level jets on boundary layer ozone concentration. *Atmospheric Environment*, **70,** 123-130.

Hu, X.-M., and Coauthors, 2021: Implementation of improved parameterization of terrestrial flux in WRF‐VPRM improves the simulation of nighttime CO_2 peaks and a daytime CO_2 band ahead of a cold front. *Journal of Geophysical Research: Atmospheres*, **126,** e2020JD034362.

Hu, X.-M., and Coauthors, 2020: Dynamical Downscaling of CO2 in 2016 over the contiguous United States using WRF‐VPRM, a weather‐biosphere‐online‐coupled model. *Journal of Advances in Modeling Earth Systems*, **12,** e2019MS001875.

Hunt, E. D., K. G. Hubbard, D. A. Wilhite, T. J. Arkebauer, and A. L. Dutcher, 2009: The development and evaluation of a soil moisture index. *International Journal of Climatology: A Journal of the Royal Meteorological Society*, **29,** 747-759.

Iacono, M. J., J. S. Delamere, E. J. Mlawer, M. W. Shephard, S. A. Clough, and W. D. Collins, 2008: Radiative forcing by long‐lived greenhouse gases: Calculations with the AER radiative transfer models. *Journal of Geophysical Research: Atmospheres*, **113**.

Irvin, J., and Coauthors, 2021: Gap-filling eddy covariance methane fluxes: Comparison of machine learning model predictions and uncertainties at FLUXNET-CH4 wetlands. *Agricultural and Forest Meteorology*, **308,** 108528.

Ishizuka, S., H. Tsuruta, and D. Murdiyarso, 2002: An intensive field study on CO2, CH4, and N2O emissions from soils at four land‐use types in Sumatra, Indonesia. *Global Biogeochemical Cycles*, **16,** 22-21-22-11.

Jacob, D. J., and Coauthors, 2016: Satellite observations of atmospheric methane and their value for quantifying methane emissions. *Atmospheric Chemistry and Physics*, **16,** 14371-14396.

Jaeger, E. B., R. Stöckli, and S. I. Seneviratne, 2009: Analysis of planetary boundary layer fluxes and land - atmosphere coupling in the regional climate model CLM. *Journal of Geophysical Research: Atmospheres*, **114**.

Jahan, I., M. Mehana, G. Matheou, and H. Viswanathan, 2024: Deep Learning-Based quantifications of methane emissions with field applications. *International Journal of Applied Earth Observation and Geoinformation*, **132,** 104018.

Jarvis, P., 1976: The interpretation of the variations in leaf water potential and stomatal conductance found in canopies in the field. *Philosophical Transactions of the Royal Society of London. B, Biological Sciences*, **273,** 593-610.

Jin, J., N. L. Miller, and N. Schlegel, 2010: Sensitivity study of four land surface schemes in the WRF model. *Advances in Meteorology*, **2010,** 167436.

Jongaramrungruang, S., C. Frankenberg, G. Matheou, A. K. Thorpe, D. R. Thompson, L. Kuai, and R. M. Duren, 2019: Towards accurate methane point-source quantification from high-resolution 2-D plume imagery. *Atmospheric Measurement Techniques*, **12,** 6667-6681.

Jordan, R. E., 1991: A one-dimensional temperature model for a snow cover: Technical documentation for SNTHERM. 89.

Ju, C., and Coauthors, 2022: Comparison of the forecast performance of WRF using Noah and Noah-MP land surface schemes in Central Asia arid region. *Atmosphere*, **13,** 927.

Karion, A., and Coauthors, 2015: Aircraft-based estimate of total methane emissions from the Barnett Shale region. *Environmental science & technology*, **49,** 8124-8131.

Kasting, J. F., 2004: When methane made climate. *Scientific American*, **291,** 78-85.

Katzenstein, A. S., L. A. Doezema, I. J. Simpson, D. R. Blake, and F. S. Rowland, 2003: Extensive regional atmospheric hydrocarbon pollution in the southwestern United States. *Proceedings of the National Academy of Sciences*, **100,** 11975-11979.

Keeler, E., R. Coulter, J. Kyrouac, and D. Holdridge, 2019: Balloon-Borne Sounding System (SONDEWNPN). *Atmospheric Radiation Measurement (ARM) user facility, accessed*, **30**.

Keller, M., and R. F. Stallard, 1994: Methane emission by bubbling from Gatun Lake, Panama. *Journal of Geophysical Research: Atmospheres*, **99,** 8307-8319.

Kenneth N. Schuldt, T. A., Arlyn Andrews, Francesco Apadula, Jgor Arduini, Sabrina Arnold, Bianca Baier, Jakub Bartyzel, Peter Bergamaschi, Tobias Biermann, Sebastien C. Biraud, Pierre-Eric Blanc, Harald Boenisch, Gordon Brailsford, Willi A. Brand, Dominik Brunner, Thao P. Bui, Lukas Bäni, Francescopiero Calzolari, Cecilia S. Chang, Huilin Chen, Lukasz Chmura, Sites Climadat, Aurelie Colomb, Lino Condori, Franz Conen, Sébastien Conil, Cédric Couret, Paolo Cristofanelli, Emilio Cuevas, Roger Curcoll, Bruce Daube, Kenneth J. Davis, Martine De Mazière, Jonathan M. Dean-Day, Julian Della Coletta, Marc Delmotte, Ankur Desai, Tatiana Di Iorio, Joshua P. DiGangi, Elizabeth DiGangi, James W. Elkins, Michael Elsasser, Lukas Emmenegger, Marc L. Fischer, Grant Forster, Arnoud Frumau, Marta Fuente-Lastra, Michal Galkowski, Luciana V. Gatti, Torsten Gehrlein, Christoph Gerbig, Francois Gheusi, Emanuel Gloor, Daisuke Goto, Samuel Hammer, Thomas F. Hanisco, László Haszpra, Juha Hatakka, Martin Heimann, Michal Heliasz, Daniela Heltai, Stephan Henne, Arjan Hensen, Christian Hermans, Ove Hermansen, Eric Hintsa, Antje Hoheisel, Jutta Holst, Laura T. Iraci, Viktor Ivakhov, Daniel A. Jaffe, Armin Jordan, Warren Joubert, Hui-Yun Kang, Anna Karion, Victor Kazan, Ralph F. Keeling, Petri Keronen, Bert Kers, Jooil Kim, Jörg Klausen, Tobias Kneuer, Mi-Young Ko, Pasi Kolari, Katerina Kominkova, Eric Kort, Elena Kozlova, Paul B. Krummel, Dagmar Kubistin, Susan S. Kulawik, Nicolas Kumps,

Casper Labuschagne, Xin Lan, Ray L. Langenfelds, Andrea Lanza, Olivier Laurent, Tuomas Laurila, Thomas Lauvaux, Jost Lavric, Haeyoung Lee, John Lee, Choong-Hoon Lee, Irene Lehner, Kari Lehtinen, Reimo Leppert, Ari Leskinen, Markus Leuenberger, Ingeborg Levin, Janne Levula, Matthias Lindauer, Anders Lindroth, Zoe M. Loh, Morgan Lopez, David Lowry, Chris R. Lunder, Mikaell O. Löfvenius, Toshinobu Machida, Ivan Mammarella, Giovanni Manca, Alistair Manning, Michal V. Marek, Per Marklund, Josette E. Marrero, Damien Martin, Melissa Y. Martin, Giordane A. Martins, Hidekazu Matsueda, Kathryn McKain, Frank Meinhardt, Malika Menoud, Jean-Marc Metzger, Natasha L. Miles, John B. Miller, Charles E. Miller, Vanessa Monteiro, Stephen Montzka, Fred Moore, Heiko Moossen, Eric Morgan, Josep-Anton Morgui, Shinji Morimoto, David Munro, Mathew Mutuku, Cathrine L. Myhre, Meelis Mölder, Jennifer Müller-Williams, Jaroslaw Necki, Sylvia Nichol, Euan Nisbet, Yosuke Niwa, David M. Njiru, Steffen M. Noe, Simon O\'Doherty, Florian Obersteiner, Caroline L. Parworth, Olli Peltola, Wouter Peters, Carole Philippon, Salvatore Piacentino, Jean M. Pichon, Penelope Pickers, Joseph Pitt, Jasna Pittman, Christian Plass-Dülmer, Stephen M. Platt, Maria E. Popa, Steve Prinzivalli, Michel Ramonet, Scott J. Richardson, Louis-Jeremy Rigouleau, Pedro P. Rivas, Michael Rothe, Yves-Alain Roulet, Ju-Mee Ryoo, Thomas Röckmann, Greg Santoni, Motoki Sasakawa, Bert Scheeren, Martina Schmidt, Tanja Schuck, Marcus Schumacher, Thomas Seifert, Mahesh K. Sha, Paul Shepson, Christopher D. Sloop, Paul D. Smith, Gerard Spain, Jason M. St. Clair, David Steger, Martin Steinbacher, Britton Stephens, Colm Sweeney, Lise L. Sørensen, Risto Taipale, Shinya Takatsuji, Kirk Thoning, Helder Timas, Margaret Torn, Pamela Trisolino, Jocelyn Turnbull, Alex Vermeulen, Isaac Vimont, Brian Viner, Gabriela Vitkova, Andrew Watson, Ray Weiss, Dietmar Weyrauch, Steven C. Wofsy, Justin Worsey, Doug Worthy, Irène Xueref-Remy, Emma L. Yates, Dickon Young, Camille Yver-Kwok, Sönke Zaehle, Andreas Zahn, Giulia Zazzeri, Christoph Zellweger, Miroslaw Zimnoch, Rodrigo A. de

Souza, Marcel de Vries, Alcide G. di Sarra, Danielle van Dinther, Pim van den Bulk, Carina van der Veen, 2023: Multi-laboratory compilation of atmospheric methane data for the period 1983-2022; obspack_ch4_1_GLOBALVIEWplus_v6.0_2023-12-01. G. M. L. NOAA Earth System Research Laboratory, Ed.

Kirchgessner, D. A., S. D. Piccot, and J. D. Winkler, 1993: Estimate of global methane emissions from coal mines. *Chemosphere*, **26,** 453-472.

Klein, P. M., X.-M. Hu, and M. Xue, 2014: Impacts of mixing processes in nocturnal atmospheric boundary layer on urban ozone concentrations. *Boundary-layer meteorology*, **150,** 107-130.

Kobayashi, S., and Coauthors, 2015: The JRA-55 reanalysis: General specifications and basic characteristics. *Journal of the Meteorological Society of Japan. Ser. II*, **93,** 5-48.

Kollet, S. J., and R. M. Maxwell, 2008: Capturing the influence of groundwater dynamics on land surface processes using an integrated, distributed watershed model. *Water Resources Research*, **44**.

Koren, V., J. Schaake, K. Mitchell, Q. Y. Duan, F. Chen, and J. Baker, 1999: A parameterization of snowpack and frozen ground intended for NCEP weather and climate models. *Journal of Geophysical Research: Atmospheres*, **104,** 19569-19585.

Kort, E. A., C. Frankenberg, K. R. Costigan, R. Lindenmaier, M. K. Dubey, and D. Wunch, 2014: Four corners: The largest US methane anomaly viewed from space. *Geophysical Research Letters*, **41,** 6898-6903.

Koyama, A., N. G. Johnson, P. Brewer, C. T. Webb, and J. C. von Fischer, 2024: Biological and physical controls of methane uptake in grassland soils across the US Great Plains. *Ecosphere*, **15,** e4955.

Krings, T., and Coauthors, 2013: Quantification of methane emission rates from coal mine ventilation shafts using airborne remote sensing data. *Atmospheric Measurement Techniques*, **6,** 151-166.

Kuze, A., N. Kikuchi, F. Kataoka, H. Suto, K. Shiomi, and Y. Kondo, 2020: Detection of methane emission from a local source using GOSAT target observations. *Remote Sensing*, **12,** 267.

Kyrouac, J., and M. Tuftedal, 2024: Surface Meteorological System (MET) Instrument Handbook, Medium: ED pp.

Laguë, M. M., G. B. Bonan, and A. L. Swann, 2019: Separating the impact of individual land surface properties on the terrestrial surface energy budget in both the coupled and uncoupled land–atmosphere system. *Journal of Climate*, **32,** 5725-5744.

Lamb, B. K., and Coauthors, 2015: Direct measurements show decreasing methane emissions from natural gas local distribution systems in the United States. *Environmental Science & Technology*, **49,** 5161-5169.

Lavoie, T. N., and Coauthors, 2015: Aircraft-based measurements of point source methane emissions in the Barnett Shale basin. *Environmental science & technology*, **49,** 7904-7913.

Law, R., and Coauthors, 2008: TransCom model simulations of hourly atmospheric CO2: Experimental overview and diurnal cycle results for 2002. *Global Biogeochemical Cycles*, **22**.

Lee, C. B., J.-C. Kim, M. Belorid, and P. Zhao, 2016: Performance evaluation of four different land surface models in WRF. *Asian Journal of Atmospheric Environment*, **10,** 42-50.

Lenhart, T., K. Eckhardt, N. Fohrer, and H.-G. Frede, 2002: Comparison of two different approaches of sensitivity analysis. *Physics and Chemistry of the Earth, Parts A/B/C*, **27,** 645-654.

Leytem, A. B., R. S. Dungan, D. L. Bjorneberg, and A. C. Koehn, 2011: Emissions of ammonia, methane, carbon dioxide, and nitrous oxide from dairy cattle housing and manure management systems. *Journal of environmental quality*, **40,** 1383-1394.

Leytem, A. B., D. L. Bjorneberg, A. Koehn, L. Moraes, E. Kebreab, and R. Dungan, 2017: Methane emissions from dairy lagoons in the western United States. *Journal of dairy science*, **100,** 6785-6803.

Li, J., C. Miao, G. Zhang, Y. H. Fang, W. Shangguan, and G. Y. Niu, 2022: Global evaluation of the Noah‐MP land surface model and suggestions for selecting parameterization schemes. *Journal of Geophysical Research: Atmospheres*, **127,** e2021JD035753.

Li, X., and Coauthors, 2023: On the Large Variation in Atmospheric CO2 Concentration at Shangdianzi GAW Station during Two Dust Storm Events in March 2021. *Atmosphere*, **14,** 1348.

Li, X., and Coauthors, 2020: Terrestrial CO2 fluxes, concentrations, sources and budget in Northeast China: Observational and modeling studies. *Journal of Geophysical Research: Atmospheres*, **125,** e2019JD031686.

Lipiec, J., J. Kuś, A. Słowińska-Jurkiewicz, and A. Nosalewicz, 2006: Soil porosity and water infiltration as influenced by tillage methods. *Soil and Tillage research*, **89,** 210-220.

López-Urrea, R., F. M. de Santa Olalla, C. Fabeiro, and A. Moratalla, 2006: Testing evapotranspiration equations using lysimeter observations in a semiarid climate. *Agricultural water management*, **85,** 15-26.

Lu, D., D. Ricciuto, A. Walker, C. Safta, and W. Munger, 2017: Bayesian calibration of terrestrial ecosystem models: a study of advanced Markov chain Monte Carlo methods. *Biogeosciences*, **14,** 4295-4314.

Lu, X., Y.-P. Wang, T. Ziehn, and Y. Dai, 2013: An efficient method for global parameter sensitivity analysis and its applications to the Australian community land surface model (CABLE). *Agricultural and forest meteorology*, **182,** 292-303.

Luiz, E. W., and S. Fiedler, 2024: Global climatology of low‐level‐jets: Occurrence, characteristics, and meteorological drivers. *Journal of Geophysical Research: Atmospheres*, **129,** e2023JD040262.

Lyon, D. R., and Coauthors, 2015: Constructing a spatially resolved methane emission inventory for the Barnett Shale region. *Environmental science & technology*, **49,** 8147-8157.

Ma, J., Y. Ding, J. C. Cheng, F. Jiang, V. J. Gan, and Z. Xu, 2020: A Lag-FLSTM deep learning network based on Bayesian Optimization for multi-sequential-variant PM2. 5 prediction. *Sustainable Cities and Society*, **60,** 102237.

Ma, S., and Coauthors, 2022: Evaluating alternative ebullition models for predicting peatland methane emission and its pathways via data–model fusion. *Biogeosciences*, **19,** 2245-2262.

Mahadevan, P., and Coauthors, 2008: A satellite‐based biosphere parameterization for net ecosystem CO2 exchange: Vegetation Photosynthesis and Respiration Model (VPRM). *Global Biogeochemical Cycles*, **22**.

Mahmood, R., R. Leeper, and A. I. Quintanar, 2011: Sensitivity of planetary boundary layer atmosphere to historical and future changes of land use/land cover, vegetation fraction, and soil moisture in Western Kentucky, USA. *Global and Planetary Change*, **78,** 36-53.

Manabe, S., 1969: Climate and the ocean circulation: I. The atmospheric circulation and the hydrology of the earth's surface. *Monthly weather review*, **97,** 739-774.

Masarie, K., W. Peters, A. Jacobson, and P. Tans, 2014: ObsPack: a framework for the preparation, delivery, and attribution of atmospheric greenhouse gas measurements. *Earth System Science Data*, **6,** 375-384.

Mather, J. H., and J. W. Voyles, 2013: The ARM Climate Research Facility: A review of structure and capabilities. *Bulletin of the American Meteorological Society*, **94,** 377-392.

Mauder, M., and Coauthors, 2013: A strategy for quality and uncertainty assessment of long-term eddy-covariance measurements. *Agricultural and Forest Meteorology*, **169,** 122-135.

Mauritsen, T., and G. Svensson, 2007: Observations of stably stratified shear-driven atmospheric turbulence at low and high Richardson numbers. *J. Atmos. Sci.*, **64,** 645-655.

Mazzetto, A., A. S. Barneze, B. J. Feigl, J. Van Groenigen, O. Oenema, and C. C. Cerri, 2014: Temperature and moisture affect methane and nitrous oxide emission from bovine manure patches in tropical conditions. *Soil Biology and Biochemistry*, **76,** 242-248.

McCord, R., and J. Voyles, 2016: The ARM data system and archive. *Meteorological Monographs*, **57,** 11.11-11.15.

McDaniel, M. D., D. Saha, M. G. Dumont, M. Hernández, and M. A. Adams, 2019: The effect of land-use change on soil CH4 and N2O fluxes: A global meta-analysis. *Ecosystems*, **22,** 1424-1443.

McDermitt, D., and Coauthors, 2011: A new low-power, open-path instrument for measuring methane flux by eddy covariance. *Applied Physics B*, **102,** 391-405.

McNicol, G., and Coauthors, 2023: Upscaling wetland methane emissions from the FLUXNET‐CH4 Eddy covariance network (UpCH4 v1. 0): Model development, network assessment, and budget comparison. *AGU Advances*, **4,** e2023AV000956.

McNorton, J., and Coauthors, 2016: Role of OH variability in the stalling of the global atmospheric CH 4 growth rate from 1999 to 2006. *Atmospheric Chemistry and Physics*, **16,** 7943-7956.

Meijninger, W., O. Hartogensis, W. Kohsiek, J. Hoedjes, R. Zuurbier, and H. De Bruin, 2002: Determination of area-averaged sensible heat fluxes with a large aperture scintillometer over a heterogeneous surface–Flevoland field experiment. *Boundary-Layer Meteorology*, **105,** 37-62.

Metya, A., A. Datye, S. Chakraborty, Y. K. Tiwari, D. Sarma, A. Bora, and N. Gogoi, 2021: Diurnal and seasonal variability of CO2 and CH4 concentration in a semi-urban environment of western India. *Scientific reports*, **11,** 2931.

Milich, L., 1999: The role of methane in global warming: where might mitigation strategies be focused? *Global Environmental Change*, **9,** 179-201.

Miller, D. N., and E. D. Berry, 2005: Cattle feedlot soil moisture and manure content: I. Impacts on greenhouse gases, odor compounds, nitrogen losses, and dust. *Journal of environmental quality*, **34,** 644-655.

Miller, S. M., and Coauthors, 2013: Anthropogenic emissions of methane in the United States. *Proceedings of the National Academy of Sciences*, **110,** 20018-20022.

Milly, P., and A. Shmakin, 2002a: Global modeling of land water and energy balances. Part I: The land dynamics (LaD) model. *Journal of Hydrometeorology*, **3,** 283-299.

——, 2002b: Global modeling of land water and energy balances. Part II: Land-characteristic contributions to spatial variability. *Journal of Hydrometeorology*, **3,** 301-310.

Minato, K., Y. Kouda, M. Yamakawa, S. Hara, T. Tamura, and T. Osada, 2013: Determination of GHG and ammonia emissions from stored dairy cattle slurry by using a floating dynamic chamber. *Animal Science Journal*, **84,** 165-177.

Misra, V., 2020: *Regionalizing global climate variations: a study of the Southeastern US regional climate.* Elsevier.

Mlawer, E. J., S. J. Taubman, P. D. Brown, M. J. Iacono, and S. A. Clough, 1997: Radiative transfer for inhomogeneous atmospheres: RRTM, a validated correlated‐k model for the longwave. *Journal of Geophysical Research: Atmospheres*, **102,** 16663-16682.

Montaldo, N., V. Toninelli, J. D. Albertson, M. Mancini, and P. A. Troch, 2003: The effect of background hydrometeorological conditions on the sensitivity of evapotranspiration to model parameters: analysis with measurements from an Italian alpine catchment. *Hydrology and Earth System Sciences*, **7,** 848-861.

Montgomery, R., 1948: Vertical eddy flux of heat in the atmosphere. *Journal of the Atmospheric Sciences*, **5,** 265-274.

Morán, A., R. Ferreyra, G. Sellés, E. Salgado, A. Cáceres-Mella, and C. Poblete-Echeverría, 2020: Calibration of the Surface Renewal Method (SR) under Different Meteorological Conditions in an Avocado Orchard. *Agronomy*, **10,** 730.

Moreira, G. d. A., M. Marques, W. Nakaema, A. de CA Moreira, and E. Landulfo, 2015: Detecting the planetary boundary layer height from low-level jet with Doppler lidar measurements. *Lidar Technologies, Techniques, and Measurements for Atmospheric Remote Sensing XI*, SPIE, 80-89.

Morin, T. H., 2019: Advances in the eddy covariance approach to CH4 monitoring over two and a half decades. *Journal of Geophysical Research: Biogeosciences*, **124,** 453-460.

Muñoz Sabater, J., 2019: ERA5-Land hourly data from 1981 to present. *Copernicus Climate Change Service (C3S) Climate Data Store (CDS)*, **10**.

Munoz-González, L., 2017: Bayesian Optimization for Black-Box Evasion of Machine Learning Systems, PhD thesis, Imperial College London.

Myhre, G., E. J. Highwood, K. P. Shine, and F. Stordal, 1998: New estimates of radiative forcing due to well mixed greenhouse gases. *Geophysical research letters*, **25,** 2715-2718.

Myhre, G., and Coauthors, 2011: Radiative forcing due to changes in ozone and methane caused by the transport sector. *Atmospheric Environment*, **45,** 387-394.

Myhre, G., and Coauthors, 2014: Anthropogenic and natural radiative forcing. *Climate Change 2013-The Physical Science Basis***,** 659-740.

Nesser, H., and Coauthors, 2024: High-resolution US methane emissions inferred from an inversion of 2019 TROPOMI satellite data: contributions from individual states, urban areas, and landfills. *Atmospheric Chemistry and Physics*, **24,** 5069-5091.

Newsom, R. K., and R. Krishnamurthy, 2022: Doppler Lidar (DL) instrument handbook.

Newsom, R. K., C. Sivaraman, T. Shippert, and L. Riihimaki, 2015: Doppler lidar wind value-added product.

Newsom, R. K., C. Sivaraman, T. Shippert, and L. Riihimaki, 2019: Doppler lidar vertical velocity statistics value-added product.

Nishanth, T., K. Praseed, M. S. Kumar, and K. Valsaraj, 2014: Observational study of surface O3, NOx, CH4 and total NMHCs at Kannur, India. *Aerosol and Air Quality Research*, **14,** 1074-1088.

Niu, G. Y., 2011: The community Noah land-surface model (LSM) with multi-physics options. *User Guide, Heritage***,** 1-21.

Niu, G. Y., and Z. L. Yang, 2004: Effects of vegetation canopy processes on snow surface energy and mass balances. *Journal of Geophysical Research: Atmospheres*, **109**.

——, 2006: Effects of frozen soil on snowmelt runoff and soil water storage at a continental scale. *Journal of Hydrometeorology*, **7,** 937-952.

Niu, G. Y., Z. L. Yang, R. E. Dickinson, and L. E. Gulden, 2005: A simple TOPMODEL ‐ based runoff parameterization (SIMTOP) for use in global climate models. *Journal of Geophysical Research: Atmospheres*, **110**.

Niu, G. Y., Z. L. Yang, R. E. Dickinson, L. E. Gulden, and H. Su, 2007: Development of a simple groundwater model for use in climate models and evaluation with Gravity Recovery and Climate Experiment data. *Journal of Geophysical Research: Atmospheres*, **112**.

Niu, G. Y., and Coauthors, 2011: The community Noah land surface model with multiparameterization options (Noah‐MP): 1. Model description and evaluation with local‐scale measurements. *Journal of Geophysical Research: Atmospheres*, **116**.

North, G. R., J. A. Pyle, and F. Zhang, 2014: *Encyclopedia of atmospheric sciences.* Vol. 1, Elsevier.

Novick, K. A., J. Biederman, A. Desai, M. Litvak, D. J. Moore, R. Scott, and M. Torn, 2018: The AmeriFlux network: A coalition of the willing. *Agricultural and Forest Meteorology*, **249,** 444-456.

Obukhov, A., 1951: Charakteristiki mikrostruktury vetra v prizemnom sloje atmosfery (Characteristics of the micro-structure of the wind in the surface layer of the atmosphere). *Izv AN SSSR, Ser Geofiz*, **3,** 49-68.

Oleson, K. W., and Coauthors, 2010: Technical description of version 4.0 of the Community Land Model (CLM).

Omara, M., and Coauthors, 2018: Methane emissions from natural gas production sites in the United States: Data synthesis and national estimate. *Environmental science & technology*, **52,** 12915-12925.

Pal, S., and M. Haeffelin, 2015: Forcing mechanisms governing diurnal, seasonal, and interannual variability in the boundary layer depths: Five years of continuous lidar observations over a suburban site near Paris. *Journal of Geophysical Research: Atmospheres*, **120,** 11,936-911,956.

Pan, Z., M. Segal, and R. W. Arritt, 2004: Role of topography in forcing low-level jets in the central United States during the 1993 flood-altered terrain simulations. *Monthly weather review*, **132,** 396-403.

Pandey, S., and Coauthors, 2019: Satellite observations reveal extreme methane leakage from a natural gas well blowout. *Proceedings of the National Academy of Sciences*, **116,** 26376-26381.

Parker, R., and Coauthors, 2011: Methane observations from the Greenhouse Gases Observing SATellite: Comparison to ground‐based TCCON data and model calculations. *Geophysical Research Letters*, **38**.

Patra, P. K., and Coauthors, 2009: Growth rate, seasonal, synoptic, diurnal variations and budget of methane in the lower atmosphere. *Journal of the Meteorological Society of Japan. Ser. II*, **87,** 635-663.

Peischl, J., and Coauthors, 2015: Quantifying atmospheric methane emissions from the Haynesville, Fayetteville, and northeastern Marcellus shale gas production regions. *Journal of Geophysical Research: Atmospheres*, **120,** 2119-2139.

Pison, I., B. Ringeval, P. Bousquet, C. Prigent, and F. Papa, 2013: Stable atmospheric methane in the 2000s: key-role of emissions from natural wetlands. *Atmospheric Chemistry and Physics*, **13,** 11609-11623.

Pitman, A. J., 2003: The evolution of, and revolution in, land surface schemes designed for climate models. *International Journal of Climatology: A Journal of the Royal Meteorological Society*, **23,** 479-510.

Prihodko, L., A. Denning, N. Hanan, I. Baker, and K. Davis, 2008: Sensitivity, uncertainty and time dependence of parameters in a complex land surface model. *agricultural and forest meteorology*, **148,** 268-287.

Prueger, J. H., J. L. Hatfield, J. K. Aase, and J. L. Pikul Jr, 1997: Bowen‐ratio comparisons with lysimeter evapotranspiration. *Agronomy Journal*, **89,** 730-736.

Puckett, W., J. Dane, and B. Hajek, 1985: Physical and mineralogical data to determine soil hydraulic properties. *Soil Science Society of America Journal*, **49,** 831-836.

Qiu, J., H.-B. Su, T. Watanabe, and Y. Brunet, 1995: Surface renewal analysis: a new method to obtain scalar fluxes. *Agricultural and Forest Meteorology*, **74,** 119-137.

Räsänen, A., T. Manninen, M. Korkiakoski, A. Lohila, and T. Virtanen, 2021: Predicting catchment-scale methane fluxes with multi-source remote sensing. *Landscape Ecology*, **36,** 1177-1195.

Raupach, M., 1995: Vegetation-atmosphere interaction and surface conductance at leaf, canopy and regional scales. *Agricultural and Forest Meteorology*, **73,** 151-179.

Reay, D. S., P. Smith, T. R. Christensen, R. H. James, and H. Clark, 2018: Methane and global environmental change. *Annual Review of Environment and Resources*, **43,** 165-192.

Rennie, T. J., R. J. Gordon, W. N. Smith, and A. C. VanderZaag, 2018: Liquid manure storage temperature is affected by storage design and management practices—A modelling assessment. *Agriculture, Ecosystems & Environment*, **260,** 47-57.

Riddick, S. N., and Coauthors, 2017: Estimating the size of a methane emission point source at different scales: from local to landscape. *Atmospheric Chemistry and Physics*, **17,** 7839-7851.

Rigby, M., and Coauthors, 2017: Role of atmospheric oxidation in recent methane growth. *Proceedings of the National Academy of Sciences*, **114,** 5373-5377.

Robertson, G. P., E. A. Paul, and R. R. Harwood, 2000: Greenhouse gases in intensive agriculture: contributions of individual gases to the radiative forcing of the atmosphere. *Science*, **289,** 1922-1925.

Röckmann, T., and Coauthors, 2016: In situ observations of the isotopic composition of methane at the Cabauw tall tower site. *Atmospheric Chemistry and Physics*, **16,** 10469-10487.

Rosolem, R., H. V. Gupta, W. J. Shuttleworth, X. Zeng, and L. G. G. De Gonçalves, 2012: A fully multiple‐criteria implementation of the Sobol′ method for parameter sensitivity analysis. *Journal of Geophysical Research: Atmospheres*, **117**.

Ryoo, J.-M., and Coauthors, 2019: Quantification of CO 2 and CH 4 emissions over Sacramento, California, based on divergence theorem using aircraft measurements. *Atmospheric Measurement Techniques*, **12,** 2949-2966.

Saito, R., and Coauthors, 2013: TransCom model simulations of methane: Comparison of vertical profiles with aircraft measurements. *Journal of Geophysical Research: Atmospheres*, **118,** 3891-3904.

Sakabe, A., K. Hamotani, Y. Kosugi, M. Ueyama, K. Takahashi, A. Kanazawa, and M. Itoh, 2012: Measurement of methane flux over an evergreen coniferous forest canopy using a relaxed eddy accumulation system with tuneable diode laser spectroscopy detection. *Theoretical and applied climatology*, **109,** 39-49.

Sakaguchi, K., and X. Zeng, 2009: Effects of soil wetness, plant litter, and under‐canopy atmospheric stability on ground evaporation in the Community Land Model (CLM3. 5). *Journal of Geophysical Research: Atmospheres*, **114**.

Santanello Jr, J. A., C. D. Peters-Lidard, and S. V. Kumar, 2011a: Diagnosing the sensitivity of local land–atmosphere coupling via the soil moisture–boundary layer interaction. *Journal of Hydrometeorology*, **12,** 766-786.

Santanello Jr, J. A., and Coauthors, 2011b: Local land-atmosphere coupling (LoCo) research: Status and results. *GEWEX news*, **21,** 7-9.

Sawyer, W. J., I. Genina, R. J. Brenneis, H. Feng, Y. Li, and S.-X. L. Luo, 2022: Methane emissions and global warming: Mitigation technologies, policy ambitions, and global efforts. *MIT Sci. Policy Rev*, **3,** 73-84.

Schaake, J. C., V. I. Koren, Q. Y. Duan, K. Mitchell, and F. Chen, 1996: Simple water balance model for estimating runoff at different spatial and temporal scales. *Journal of Geophysical Research: Atmospheres*, **101,** 7461-7475.

Schjønning, P., and K. J. Rasmussen, 2000: Soil strength and soil pore characteristics for direct drilled and ploughed soils. *Soil and Tillage Research*, **57,** 69-82.

Schmid, H., 1994: Source areas for scalars and scalar fluxes. *Boundary-Layer Meteorology*, **67,** 293-318.

Sellers, P. J., and Coauthors, 1997a: Modeling the exchanges of energy, water, and carbon between continents and the atmosphere. *Science*, **275,** 502-509.

Sellers, P. J., and Coauthors, 1997b: Modeling the exchanges of energy, water, and carbon between continents and the atmosphere. *Science*, **275,** 502-509.

Seneviratne, S. I., D. Lüthi, M. Litschi, and C. Schär, 2006: Land–atmosphere coupling and climate change in Europe. *Nature*, **443,** 205-209.

Seneviratne, S. I., and Coauthors, 2010: Investigating soil moisture–climate interactions in a changing climate: A review. *Earth-Science Reviews*, **99,** 125-161.

Shahriari, B., K. Swersky, Z. Wang, R. P. Adams, and N. De Freitas, 2015: Taking the human out of the loop: A review of Bayesian optimization. *Proceedings of the IEEE*, **104,** 148-175.

Shaw, J. T., A. Shah, H. Yong, and G. Allen, 2021: Methods for quantifying methane emissions using unmanned aerial vehicles: A review. *Philosophical Transactions of the Royal Society A*, **379,** 20200450.

Shen, L., and Coauthors, 2022: Satellite quantification of oil and natural gas methane emissions in the US and Canada including contributions from individual basins. *Atmospheric Chemistry and Physics*, **22,** 11203-11215.

Sicard, P., and Coauthors, 2021: High spatial resolution WRF-Chem model over Asia: Physics and chemistry evaluation. *Atmospheric Environment*, **244,** 118004.

Siler, N., G. H. Roe, K. C. Armour, and N. Feldl, 2019: Revisiting the surface-energy-flux perspective on the sensitivity of global precipitation to climate change. *Climate Dynamics*, **52,** 3983-3995.

Singh, S., K. Kulshreshtha, and S. Agnihotri, 2000: Seasonal dynamics of methane emission from wetlands. *Chemosphere-Global Change Science*, **2,** 39-46.

Sisterson, D., R. Peppler, T. Cress, P. Lamb, and D. Turner, 2016: The ARM southern great plains (SGP) site. *Meteorological Monographs*, **57,** 6.1-6.14.

Skamarock, W. C., and Coauthors, 2008: A description of the advanced research WRF version 3. *NCAR technical note*, **475,** 10.5065.

Skamarock, W. C., and Coauthors, 2019: A description of the advanced research WRF version 4. *NCAR tech. note ncar/tn-556+ str*, **145**.

Snyder, R., D. Spano, and K. Pawu, 1996: Surface renewal analysis for sensible and latent heat flux density. *Boundary-Layer Meteorology*, **77,** 249-266.

Solazzo, E., M. Crippa, D. Guizzardi, M. Muntean, M. Choulga, and G. Janssens-Maenhout, 2021: Uncertainties in the Emissions Database for Global Atmospheric Research (EDGAR) emission inventory of greenhouse gases. *Atmospheric Chemistry and Physics*, **21,** 5655-5683.

Song, J., K. Liao, R. L. Coulter, and B. M. Lesht, 2005: Climatology of the low-level jet at the southern Great Plains atmospheric boundary layer experiments site. *Journal of Applied Meteorology and Climatology*, **44,** 1593-1606.

Spano, D., R. L. Snyder, and P. Duce, 2000: Estimating sensible and latent heat flux densities from grapevine canopies using surface renewal. *Agricultural and Forest Meteorology*, **104,** 171-183.

Spittlehouse, D., and T. Black, 1980: Evaluation of the Bowen ratio/energy balance method for determining forest evapotranspiration. *Atmosphere-Ocean*, **18,** 98-116.

Stavert, A. R., and Coauthors, 2022: Regional trends and drivers of the global methane budget. *Global Change Biology*, **28,** 182-200.

Stocker, T. F., and Coauthors, 2013: *Climate change 2013: the physical science basis: Working Group I contribution to the Fifth assessment report of the Intergovernmental Panel on Climate Change.* Cambridge university press.

Stull, R. B., 1988: *An introduction to boundary layer meteorology.* Vol. 13, Springer Science & Business Media.

——, 2015: *Practical meteorology: an algebra-based survey of atmospheric science.* University of British Columbia.

Su, Z., 2006: Estimation of the surface energy balance. *Encyclopedia of hydrological sciences*.

Sun, H., and Coauthors, 2008: Alcohol, volatile fatty acid, phenol, and methane emissions from dairy cows and fresh manure. *Journal of environmental quality*, **37,** 615-622.

Swinbank, W., 1951: The measurement of vertical transfer of heat and water vapor by eddies in the lower atmosphere. *Journal of Atmospheric Sciences*, **8,** 135-145.

Tan, J.-w., Q.-y. Duan, W. Gong, and Z.-h. Di, 2022: Differences in parameter estimates derived from various methods for the ORYZA (v3) Model. *Journal of Integrative Agriculture*, **21,** 375-388.

Thompson, R. L., and Coauthors, 2017: Methane fluxes in the high northern latitudes for 2005–2013 estimated using a Bayesian atmospheric inversion. *Atmospheric Chemistry and Physics*, **17,** 3553-3572.

Tibrewal, K., and Coauthors, 2024: Assessment of methane emissions from oil, gas and coal sectors across inventories and atmospheric inversions. *Communications Earth & Environment*, **5,** 26.

Todd, R. W., S. R. Evett, and T. A. Howell, 2000: The Bowen ratio-energy balance method for estimating latent heat flux of irrigated alfalfa evaluated in a semi-arid, advective environment. *Agricultural and Forest Meteorology*, **103,** 335-348.

Todd, R. W., M. B. Altman, N. A. Cole, and H. M. Waldrip, 2014: Methane emissions from a beef cattle feedyard during winter and summer on the southern high plains of Texas. *Journal of environmental quality*, **43,** 1125-1130.

Todd, R. W., N. Cole, K. Casey, R. Hagevoort, and B. Auvermann, 2011: Methane emissions from southern High Plains dairy wastewater lagoons in the summer. *Animal feed science and technology*, **166,** 575-580.

Toon, G., and Coauthors, 2009: Total column carbon observing network (TCCON). *Hyperspectral Imaging and Sensing of the Environment*, Optica Publishing Group, JMA3.

Tsuboi, K., and Coauthors, 2013: Evaluation of a new JMA aircraft flask sampling system and laboratory trace gas analysis system. *Atmospheric Measurement Techniques*, **6,** 1257-1270.

Tubiello, F. N., M. Salvatore, S. Rossi, A. Ferrara, N. Fitton, and P. Smith, 2013: The FAOSTAT database of greenhouse gas emissions from agriculture. *Environmental Research Letters*, **8,** 015009.

Turner, A. J., C. Frankenberg, and E. A. Kort, 2019: Interpreting contemporary trends in atmospheric methane. *Proceedings of the National Academy of Sciences*, **116,** 2805-2813.

Turner, A. J., and Coauthors, 2016: A large increase in US methane emissions over the past decade inferred from satellite data and surface observations. *Geophysical research letters*, **43,** 2218-2224.

Turner, A. J., and Coauthors, 2015: Estimating global and North American methane emissions with high spatial resolution using GOSAT satellite data. *Atmospheric Chemistry and Physics*, **15,** 7049-7069.

Tyagi, B., and Coauthors, 2018: Performance analysis of planetary boundary layer parameterization schemes in WRF modeling set up over southern Italy. *Atmosphere*, **9,** 272.

Tyner, D. R., and M. R. Johnson, 2021: Where the methane is—Insights from novel airborne LiDAR measurements combined with ground survey data. *Environmental Science & Technology*, **55,** 9773-9783.

Uccellini, L. W., 1980: The role of upper tropospheric jet streaks and lee side cyclogenesis in the development of low level jets in the great plains.

Ueyama, M., and Coauthors, 2013: High-precision measurements of the methane flux over a larch forest based on a hyperbolic relaxed eddy accumulation method using a laser spectrometer. *Agricultural and forest meteorology*, **178,** 183-193.

Ueyama, M., and Coauthors, 2015: Methane uptake in a temperate forest soil using continuous closed-chamber measurements. *Agricultural and forest meteorology*, **213,** 1-9.

VanderZaag, A. C., R. J. Gordon, R. Jamieson, D. Burton, and G. Stratton, 2010a: Permeable synthetic covers for controlling emissions from liquid dairy manure. *Applied Engineering in Agriculture*, **26,** 287-297.

VanderZaag, A. C., R. J. Gordon, R. C. Jamieson, D. L. Burton, and G. W. Stratton, 2010b: Effects of winter storage conditions and subsequent agitation on gaseous emissions from liquid dairy manure. *Canadian Journal of Soil Science*, **90,** 229-239.

VanderZaag, A. C., T. Flesch, R. Desjardins, H. Baldé, and T. Wright, 2014: Measuring methane emissions from two dairy farms: Seasonal and manure-management effects. *Agricultural and Forest Meteorology*, **194,** 259-267.

Vaughn, T. L., and Coauthors, 2018: Temporal variability largely explains top-down/bottom-up difference in methane emission estimates from a natural gas production region. *Proceedings of the National Academy of Sciences*, **115,** 11712-11717.

Vechi, N. T., and C. Scheutz, 2023: Measurements of methane emissions from manure tanks, using a stationary tracer gas dispersion method. *Biosystems Engineering*, **233,** 21-34.

Verchot, L. V., E. A. Davidson, J. H. Cattânio, and I. L. Ackerman, 2000: Land-use change and biogeochemical controls of methane fluxes in soils of eastern Amazonia. *Ecosystems*, **3,** 41-56.

Verma, S. B., 1990: Micrometeorological methods for measuring surface fluxes of mass and energy. *Remote sensing reviews*, **5,** 99-115.

Vermote, E., 2019: NOAA Climate Data Record (CDR) of AVHRR Leaf Area Index (LAI) and Fraction of Absorbed Photosynthetically Active Radiation (FAPAR), Version 5. *NOAA National Centers for Environmental Information*.

Verseghy, D. L., 1991: CLASS—A Canadian land surface scheme for GCMs. I. Soil model. *International Journal of Climatology*, **11,** 111-133.

Wang, K., and R. E. Dickinson, 2012: A review of global terrestrial evapotranspiration: Observation, modeling, climatology, and climatic variability. *Reviews of Geophysics*, **50**.

Wang, X., M. Jia, X. Lin, Y. Xu, X. Ye, C. M. Kao, and S. Chen, 2017: A comparison of CH4, N2O and CO2 emissions from three different cover types in a municipal solid waste landfill. *Journal of the Air & Waste Management Association*, **67,** 507-515.

Wang, Y., and Coauthors, 2024: Methane emissions from landfills differentially underestimated worldwide. *Nature Sustainability*, **7,** 496-507.

Wang, Y. P., C. M. Trudinger, and I. G. Enting, 2009: A review of applications of model–data fusion to studies of terrestrial carbon fluxes at different scales. *Agricultural and forest meteorology*, **149,** 1829-1842.

Wassmann, R., H.-U. Neue, R. Lantin, L. Buendia, and H. Rennenberg, 2000: Characterization of methane emissions from rice fields in Asia. I. Comparison among field sites in five countries. *Nutrient Cycling in Agroecosystems*, **58,** 1-12.

West, J. J., A. M. Fiore, L. W. Horowitz, and D. L. Mauzerall, 2006: Global health benefits of mitigating ozone pollution with methane emission controls. *Proceedings of the National Academy of Sciences*, **103,** 3988-3993.

Western, L. M., and Coauthors, 2021: Estimates of North African methane emissions from 2010 to 2017 using GOSAT observations. *Environmental Science & Technology Letters*, **8,** 626-632.

Williams, G., E. Horn, and J. White, 1985: *Soil survey of Grant County, Oklahoma.* USDA Soil Conservation Service.

Wilson, C., M. Chipperfield, M. Gloor, and F. Chevallier, 2014: Development of a variational flux inversion system (INVICAT v1. 0) using the TOMCAT chemical transport model. *Geoscientific Model Development*, **7,** 2485-2500.

Wilson, D. M., D. L. Dalluge, M. Rover, E. A. Heaton, and R. C. Brown, 2013: Crop management impacts biofuel quality: influence of switchgrass harvest time on yield, nitrogen and ash of fast pyrolysis products. *Bioenergy Research*, **6,** 103-113.

Worden, J. R., and Coauthors, 2022: The 2019 methane budget and uncertainties at 1° resolution and each country through Bayesian integration Of GOSAT total column methane data and a priori inventory estimates. *Atmospheric Chemistry and Physics*, **22,** 6811-6841.

Wu, J., X.-Y. Chen, H. Zhang, L.-D. Xiong, H. Lei, and S.-H. Deng, 2019: Hyperparameter optimization for machine learning models based on Bayesian optimization. *Journal of Electronic Science and Technology*, **17,** 26-40.

Wyngaard, J. C., and R. A. Brost, 1984: Top-down and bottom-up diffusion of a scalar in the convective boundary layer. *Journal of the atmospheric sciences*, **41,** 102-112.

Xiao, X., D. Hollinger, J. Aber, M. Goltz, E. A. Davidson, Q. Zhang, and B. Moore III, 2004: Satellite-based modeling of gross primary production in an evergreen needleleaf forest. *Remote sensing of environment*, **89,** 519-534.

Xu, Z., H. Chen, J. Guo, and W. Zhang, 2021: Contrasting effect of soil moisture on the daytime boundary layer under different thermodynamic conditions in summer over China. *Geophysical Research Letters*, **48,** e2020GL090989.

Xue, Y., P. J. Sellers, J. Kinter, and J. Shukla, 1991: A simplified biosphere model for global climate studies. *Journal of Climate*, **4,** 345-364.

Yang, R., and M. A. Friedl, 2003: Modeling the effects of three - dimensional vegetation structure on surface radiation and energy balance in boreal forests. *Journal of Geophysical Research: Atmospheres*, **108**.

Yang, Z.-L., and R. E. Dickinson, 1996: Description of the Biosphere-Atmosphere Transfer Scheme (BATS) for the Soil Moisture Workshop and evaluation of its performance. *Global and Planetary Change*, **13,** 117-134.

Yang, Z.-L., R. E. Dickinson, A. Robock, and K. Y. Vinnikov, 1997: Validation of the snow submodel of the biosphere–atmosphere transfer scheme with Russian snow cover and meteorological observational data. *Journal of climate*, **10,** 353-373.

Yang, Z.-L., and Coauthors, 2011: The community Noah land surface model with multiparameterization options (Noah‐MP): 2. Evaluation over global river basins. *Journal of Geophysical Research: Atmospheres*, **116**.

Yavitt, J., 1992: Methane, biogeochemical cycle. *Encyclopedia of earth system science*, **3,** 197-207.

Yi, C., and Coauthors, 2004: Observed covariance between ecosystem carbon exchange and atmospheric boundary layer dynamics at a site in northern Wisconsin. *Journal of Geophysical Research: Atmospheres*, **109**.

Yu, X., and Coauthors, 2021: Aircraft-based inversions quantify the importance of wetlands and livestock for Upper Midwest methane emissions. *Atmospheric chemistry and physics*, **21,** 951-971.

Yuan, B., and Coauthors, 2015: Airborne flux measurements of methane and volatile organic compounds over the Haynesville and Marcellus shale gas production regions. *Journal of Geophysical Research: Atmospheres*, **120,** 6271-6289.

Zhang, B., and Coauthors, 2016: Methane emissions from global rice fields: Magnitude, spatiotemporal patterns, and environmental controls. *Global Biogeochemical Cycles*, **30,** 1246-1263.

Zhang, Y., Y. Chen, G. Sarwar, and K. Schere, 2012: Impact of gas‐phase mechanisms on Weather Research Forecasting Model with Chemistry (WRF/Chem) predictions: Mechanism implementation and comparative evaluation. *Journal of Geophysical Research: Atmospheres*, **117**.

Zhang, Y., Z. Gao, D. Li, Y. Li, N. Zhang, X. Zhao, and J. Chen, 2014: On the computation of planetary boundary-layer height using the bulk Richardson number method. *Geoscientific Model Development*, **7,** 2599-2611.

Zhang, Y., and Coauthors, 2020: Quantifying methane emissions from the largest oil-producing basin in the United States from space. *Science advances*, **6,** eaaz5120.

Zhang, Z., and Coauthors, 2017: Emerging role of wetland methane emissions in driving 21st century climate change. *Proceedings of the National Academy of Sciences*, **114,** 9647-9652.

Zhao, X., J. Marshall, S. Hachinger, C. Gerbig, M. Frey, F. Hase, and J. Chen, 2019: Analysis of total column CO 2 and CH 4 measurements in Berlin with WRF-GHG. *Atmospheric Chemistry and Physics*, **19,** 11279-11302.

Zhou, Y., and Coauthors, 2017: Examining the short-term impacts of diverse management practices on plant phenology and carbon fluxes of Old World bluestems pasture. *Agricultural and forest meteorology*, **237,** 60-70.